TWO-POINT STATISTICS FOR TESTING MODELS OF COSMIC STRUCTURE

Yuedong Fang

A DISSERTATION

in

Physics and Astronomy

Presented to the Faculties of the University of Pennsylvania

in

Partial Fulfillment of the Requirements for the

Degree of Doctor of Philosophy

2018

Supervisor of Dissertation

Bhuvnesh Jain, Professor, Physics and Astronomy

Graduate Group Chairperson

Joshua R. Klein, Professor, Physics and Astronomy

Dissertation Committee

Gary Bernstein, Professor, Physics and Astronomy

Masao Sako, Associate Professor, Physics and Astronomy

Bhuvnesh Jain, Professor, Physics and Astronomy

Adam Lidz, Associate Professor, Physics and Astronomy

Evelyn Thomson, Associate Professor, Physics and Astronomy

Dedicated to my parents for supporting me all the way.

ACKNOWLEDGEMENT

I have been very fortunate to have the opportunity to complete my graduate study at the Department of Physics and Astronomy at University of Pennsylvania. It is such a wonderful place with talented people.

Foremost, I would like to thank my advisor, Prof. Bhuvnesh Jain, for his continuous support of my research, for his guidance with patience and immense knowledge, and for the opportunity he offered to meet and collaborate with numerous people in the field.

I would like to thank the rest of my dissertation committee members: Prof. Gary Bernstein, Prof. Masao Sako, Prof. Adam Lidz, and Prof. Evelyn Thomson, for taking the time to review my thesis work.

I will always be grateful to Joseph Clampitt, for his patient mentoring in the early stage of my graduate school.

Special thanks go to Mike Jarvis, for all the guidance and assistance with software, programming, and statistic questions. I also want to express my gratitude to the postdocs and students in our group for many illuminative discussions: Eric Baxter, Carles Sanchez, Vinicius Miranda, Lucas Secco, Tae-Hyeon Shin, and Shivam Pandey.

Finally, I would like to thank my girlfriend Yue Zhang, for always being encouraging and supportive for my research, and for her companionship in the last few years.

ABSTRACT

TWO-POINT STATISTICS FOR TESTING MODELS OF COSMIC STRUCTURE

Yuedong Fang

Bhuvnesh Jain

Two-point statistics can be used to probe various types of cosmic structures. We perform a cross-correlation measurement using $\sim 160,000$ red satellite galaxies in SDSS redMaPPer clusters and find evidence that subhalo correlations do persist well beyond their tidal radius, suggesting that many of the observed satellites fell into their current host less than a dynamical time ago, $t_{\rm infall} < t_{\rm dyn}$. Combined with estimated dynamical times $t_{\rm dyn} \sim 3-5$ Gyr and SED fitting results for the time at which satellites stopped forming stars, $t_{\rm quench} \sim 6$ Gyr, we infer that for a significant fraction of the satellites, star formation quenched before those satellites entered their current hosts. In addition to cross-correlation measurement, galaxy-galaxy lensing is another powerful two-point statistic in cosmology analysis. We introduce and perform a number of tests of systematics on the DES Science Verification shear catalogs and photometric redshifts. We estimate the covariance matrices for the DES Year 1 galaxy-galaxy lensing measurement using the Jackknife approach. We validate the estimation using a suite of log-normal mock surveys. After testing the pipeline of our weak lensing measurement, we perform comprehensive measurements of weak lensing and galaxy clustering around voids in DES Year 1 data. We get heretofore the highest signal-to-noise void lensing measurements for voids identified by two different void finding algorithms. Using data from the MICE simulation, we study the impact of photo-z scatter on watershed types of void finder. We show that the photo-z scatter has introduced a selection bias which results in a boosting of the negative lensing signal. We also combine our observables of void lensing and void-galaxy cross-correlation to test the linear bias of redMaGiC galaxies distributed around voids. We see no evidence of departure from linearity.

TABLE OF CONTENTS

[1] This work is based on the paper [33], I led or jointly did all the analysis.

[2] This work is based on the paper [15], My contribution to the paper was primarily in sections 5.1 and 5.2 about the tests of systematics. This work is also based on the [87], My contribution to the paper was primarily in section C about the validation of the covariance estimation.

LIST OF TABLES

LIST OF FIGURES

CHAPTER 1 : Introduction

Large scale structure is defined as the inhomogeneity of the Universe on scales larger than that of a galaxy. It has long been believed by people that galaxies are distributed uniformly in space. In 1932, after analyzing a catalog of bright galaxies created by Shaply and Ames, it was first noticed by Edwin Hubble that on angular scales less than $\approx 10^\circ$ there is an excess in the number density of galaxies. Therefore, the Universe is found to be clumpy on small scales, while it appears to be homogeneous on large scales.

The first maps of the sky revealing details of large scale structure were made by Seldner and his collaborators ([96]) using data from the Lick survey. The maps not only confirmed that the projected distribution of galaxies on the plane of sky is not uniform but also displayed a foam-like pattern. This pattern consists of filaments with long strands of galaxies, clusters of galaxies, and empty regions which are referred as voids. It was Peebles and his collaborators who first analyzed the spatial distribution of galaxies in a statistical way (eg. [83]). They found that the two-point correlation function of galaxies can be described by a simple power law over a substantial range of distances.

The physical origin of the observed large scale structure is the initial fluctuations in the energy density filed of the early Universe. The current observations of anisotropy of cosmic microwave background enable us to see directly the initial conditions. The initial fluctuations grow throw gravitational instability into the patterns we saw today in the galaxy density field. The properties of the observed large scale structure is thus a consequence of the physics of the early Universe; measurements of them can therefore be useful constraining cosmological parameters.

1.1. Correlation Functions and Linear Bias

A commonly used statistic for studying large scale structure is the two-point galaxy correlation function, $\xi(\mathbf{r})$, which is defined as a measure of the excess probability, relative to a random Poisson distribution, of finding a galaxy in a volume element dV_1 at a distance r from another galaxy in a volume element dV_2:

$$d^2P = \langle n_1 \rangle \langle n_2 \rangle [1 + \xi(r)] dV_1 dV_2 \tag{1.1}$$

where $\langle n_i \rangle$ is the mean density of the galaxy in each sample ([84]). If the galaxies are of the same population, then the ξ is referred to as the auto-correlation function, otherwise the ξ is referred to as the the cross-correlation function. To measure $\xi(r)$, one counts pairs of galaxies as a function of separation and then normalized by the expected number of pairs from an randomly distributed sample with no clustering, which occupies the identical 3D volume as the data and with same redshift distribution. The random catalog should also be large enough to not introduce Poisson error in the estimator. The normalization using random catalog is introduced to correct for the issue caused by the fact that no galaxies can be observed beyond the survey boundaries. Several estimator for $\xi(r)$ has been proposed and two of them are widely used: the Davis & Peebles estimator ([23]):

$$\xi_{\mathrm{DP}}(r) = \frac{N_R}{N_D} \frac{DD(r)}{DR(r)} - 1 \tag{1.2}$$

and the Landy & Szalay estimator ([59]):

$$\xi_{\mathrm{LS}}(r) = \frac{1}{RR}[DD(\frac{N_R}{N_D})^2 - 2DR(\frac{N_R}{N_D}) + RR] \tag{1.3}$$

where DD, DR, and RR are the counts of pairs of galaxies as a function of separation in the data catalog, between data and random catalogs, and in the random catalog, respectively. N_D and N_R are the mean number densities of galaxies in the data and random catalogs.

The distribution of baryons need not trace exactly the underlying distribution of mass. This concept of biasing was first introduced by Kaiser ([54]) in an attempt to explain the observed relation between the correlation functions of galaxies and galaxy clusters, which could not both be unbiased tracers of mass. Using the high-peak approximation to a

Gaussian density field, he showed that the two correlation functions were proportional. In fact, this biasing is expected to be a nontrivial function on small scales due to complicated non-gravitational process during galaxy formation. However, on very large scales, since the density fluctuations are small, a linear relation between matter and luminous tracers can be assumed. Their ratio is referred to as the linear bias:

$$b = \xi_{tm}/\xi_{mm} \tag{1.4}$$

or

$$b = \sqrt{\xi_{tt}/\xi_{mm}} \tag{1.5}$$

where ξ_{tm} is the tracer-matter cross-correlation function, ξ_{mm} is the matter auto-correlation function and ξ_{tt} is the tracer auto-correlation function.

1.2. Weak Lensing Basics

According to General Relativity, the gravitational field of cosmic structure can deflect the path of a light ray. This process is called gravitational lensing in analogy with the deflection of light by optical lenses. The deflection is described by geodesic which follows the curvature of spacetime. The bending of light ray towards deeper gravitational potential gives rise to a few possible observational effects:

1. the image of a background source galaxy will typically appeared to be distorted, either stretched or compressed; and can be magnified or shrunken.

2. if the lens is very massive and the source is close enough to it, the light from the source can possibly take different path, which will result in the observer see multiple images of a single source. In some special cases, the observer can see arcs or 'Einstein rings'.

3. since the number of photons is conserved, the images of sources can appear brighter or fainter.

4. in case of multiple images, the paths that light travel along are with different lengths. Thus if the source varies with time, multiple images will vary accordingly but with different timing.

'Weak lensing' refers to the cases that the light from sources are only weakly deflected by lenses, where no multiple images, arcs or Einstein rings can be formed. Most importantly, It is a promising way to study the underlying dark matter distribution, which makes it a useful probe of cosmic structure. Below, we summarize some basic formalism of weak gravitational lensing.

1.2.1. Weak Lensing Geometry

With 'weak lens', we mean the Newtonian potential Φ of the lens is much smaller than c^2, $\Phi/c^2 \ll 1$. In this case, we can assume a locally flat Minkowski metric that is only weakly perturbed by the Newtonian potential of the lens.

$$\eta_{\mu\nu} \rightarrow g_{\mu\nu} = \begin{pmatrix} 1+\frac{2\Phi}{c^2} & 0 & 0 & 0 \\ 0 & -(1-\frac{2\Phi}{c^2}) & 0 & 0 \\ 0 & 0 & -(1-\frac{2\Phi}{c^2}) & 0 \\ 0 & 0 & 0 & -(1-\frac{2\Phi}{c^2}) \end{pmatrix}$$

where the line element is given by:

$$ds^2 = g_{\mu\nu}dx^\mu dx^\nu = (1+\frac{2\Phi}{c^2})c^2dt^2 - (1-\frac{2\Phi}{c^2})(d\vec{x})^2 \tag{1.6}$$

since the light propagates along the null geodesic, we have:

$$c' = \frac{|d\vec{x}|}{dt} = c\sqrt{\frac{1+\frac{2\Phi}{c^2}}{1-\frac{2\Phi}{c^2}}} \approx c(1+\frac{2\Phi}{c^2}) \tag{1.7}$$

where $\Phi/c^2 \ll 1$ by assumption. Thus we got the effective 'index of refraction' for the lens' gravitational field:

$$n = \frac{c}{c'} = \frac{1}{1 + \frac{2\Phi}{c^2}} \approx 1 - \frac{2\Phi}{c^2} \tag{1.8}$$

Then the Fermat's principle can be applied, which says the light will travel between two points along the path that requires the least time. By solving a variational problem, we can get the total deflection angle:

$$\hat{\alpha} = \frac{2}{c^2} \int_{\lambda_{\text{source}}}^{\lambda_{\text{observer}}} \vec{\nabla}_{\perp} \Phi d\lambda \tag{1.9}$$

where λ is used to parameterize the trajectory and $\vec{\nabla}_{\perp}$ is the gradient perpendicular to the path. Since we are only interested in the case where the deflection angle is small, instead of integrating along the actual deflected light path, we can integrate over the unperturbed one. Thus the deflection angle is given by:

$$\hat{\alpha} = \frac{2}{c^2} \int \vec{\nabla}_{\perp} \Phi dr_{\text{los}} \tag{1.10}$$

Figure 1 from [5] shows a sketch of a typical weak lensing system. The photon emitted at $\boldsymbol{\eta}$ takes a trajectory moving toward the observer is deflected by an angle $\hat{\alpha}$. If $\boldsymbol{\theta}$, $\boldsymbol{\beta}$, and $\hat{\alpha}$ are all small angles, they can simply be related by the lens equation:

$$\boldsymbol{\theta} D_{\text{S}} = \boldsymbol{\beta} D_{\text{S}} + \hat{\alpha} D_{\text{LS}} \tag{1.11}$$

where D_{S} and D_{LS} are the angular diameter distances from the source to the observer and from the source to the lens, respectively. And the impact parameter is given by:

$$\boldsymbol{\xi} = D_{\text{L}} \boldsymbol{\theta} \tag{1.12}$$

where D_{L} is the angular diameter distance between the source and observer and $\boldsymbol{\theta}$ is the observed angular distance between the lens and source.

we can further define the reduced deflection angle:

$$\boldsymbol{\alpha} \equiv \frac{D_{\rm LS}}{D_{\rm S}} \hat{\alpha} \tag{1.13}$$

then Equation 1.11 can be simplified as:

$$\boldsymbol{\beta} = \boldsymbol{\theta} - \boldsymbol{\alpha} \tag{1.14}$$

1.2.2. Distortion and Magnification of Observed Images

As mentioned earlier, the image of a background source galaxy will typically appeared to be distorted and magnified. Galaxies are usually intrinsically extended objects with non-negligible apparent sizes. The fact that light emitted at different position are deflected differently causes the distortion and magnification of the observed image. To study this, we can relate the observed image with the true image by asking the question: how small changes in the observed position, $\boldsymbol{\theta}$, relate to small changes in the true position $\boldsymbol{\beta}$? With small angle assumption, this can be described by the Jacobian matrix:

$$\begin{aligned} A \equiv \frac{\partial \beta_i}{\partial \theta_j} &= \frac{\partial}{\partial \theta_j}(\theta_i - \alpha_i) \\ &= \delta_{ij} - \frac{\partial \alpha_i}{\partial \theta_j} \\ &\equiv \delta_{ij} - \frac{\partial}{\partial \theta_j}(\frac{\partial \phi}{\partial \theta_i}) \end{aligned} \tag{1.15}$$

where ϕ is the effective lensing potential defined by:

$$\vec{\nabla}\phi \equiv \boldsymbol{\alpha} \tag{1.16}$$

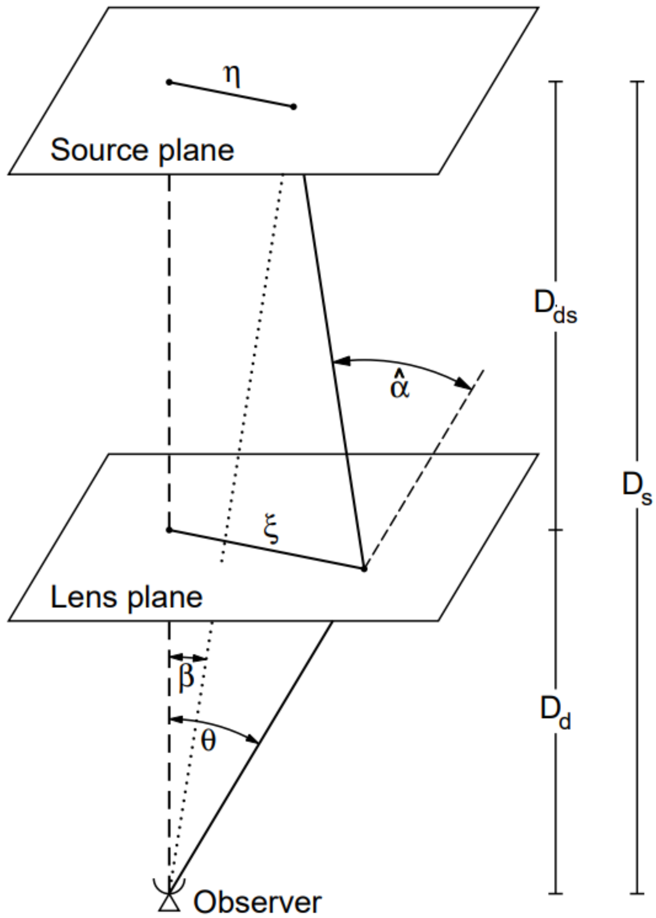

Figure 1: A sketch of weak lensing system from [5]. The photon emitted at $\boldsymbol{\eta}$ is deflected by an angle $\hat{\alpha}$ because the presence of the lens. The observed photon will be at an angle $\boldsymbol{\theta}$ from the center, which should be at an angle $\boldsymbol{\beta}$ if there is no lensing effect. All these angles can be related to each other by the angular diameter distances between source, lens, and observer.

Thus we obtain:

$$\phi(\boldsymbol{\theta}) = \frac{2}{c^2}\frac{D_{\rm LS}}{D_{\rm L}D_{\rm S}}\int \Phi(D_{\rm L}\boldsymbol{\theta}, r_{\rm los})dr_{\rm los} \tag{1.17}$$

Equation 1.15 shows that the change in shape of observed source galaxy is govern by a linear combination of second derivatives of effective lensing potential ϕ. We can split off an isotropic part from the Jacobian:

$$(A - \frac{1}{2}\,\mathrm{Tr}\,A \cdot I)_{ij} = \begin{pmatrix} -\frac{1}{2}(\phi_{,11} - \phi_{,22}) & -\phi_{,12} \\ -\phi_{,12} & \frac{1}{2}(\phi_{,11} - \phi_{,22}) \end{pmatrix}$$

This is called the shear matrix which describes the distortion. We can define the shear $\vec{\gamma} = (\gamma_1, \gamma_2)$:

$$\begin{aligned} \gamma_1 &= \frac{1}{2}(\phi_{,11} - \phi_{,22}) \\ \gamma_2 &= \phi_{,12} = \phi_{,21} \end{aligned} \tag{1.18}$$

which is a pseudo-vector on the lens plane. In reality, we often consider tangential coordinate systems defined on every lens-source pairs. The tangent component of the above shear in this system is given by:

$$\gamma_t(\boldsymbol{\theta}) = -\gamma_1(\boldsymbol{\theta})\cos(2\phi) - \gamma_2(\boldsymbol{\theta})\sin(2\phi) \tag{1.19}$$

where ϕ is the angle between the x-axis of the 'global' Cartesian coordinate system and the line joining this lens-source pair. And the cross component is given by:

$$\gamma_\times(\boldsymbol{\theta}) = \gamma_1(\boldsymbol{\theta})\sin(2\phi) - \gamma_2(\boldsymbol{\theta})\cos(2\phi) \tag{1.20}$$

describes the shear component that is at 45° to the tangential line. Gravitational lensing can only generate the tangential component γ_t of the shear. The cross component is thus usually serves as a test of systematics in the measurement.

The reminder part of the Jacobian matrix is given by:

$$\frac{1}{2}\,\mathrm{Tr}\,A = [1 - \frac{1}{2}(\phi_{,11} + \phi_{,22})]\delta_{ij} = (1-\kappa)\delta_{ij} \tag{1.21}$$

this isotropic part describe the convergence of gravitational lensing: it only rescales the image by a constant factor.

1.2.3. Stacked Measurement

The intrinsic ellipticity of individual source galaxy is in general much larger than the shear induced by weak lensing. In real observation, it is usually necessary to average over a large number of lens-source pairs.

For example, in galaxy-galaxy lensing, we calculate the average shear in angular bin as our estimator, which is given by:

$$\left\langle \gamma_i^{\mathrm{lens}}(\boldsymbol{\theta}) \right\rangle = \frac{\sum_j w'_j \gamma_{t,j}}{\sum_j w'_j} \tag{1.22}$$

where i is either t or $\times$, and the weight w'_j is usually given by:

$$w'_j = \frac{1}{\sigma^2_{\mathrm{shape}} + \sigma^2_{m,j}} \tag{1.23}$$

where σ_{shape} is the intrinsic shape noise for each source galaxy, and $\sigma_{m,j}$ is the measurement error. ,

CHAPTER 2 : Tidal Stripping as a Test of Satellite Quenching[1]

2.1. Introduction

Clusters of galaxies – composed of tens to hundreds of satellite galaxies orbiting within a dark matter halo – are the most massive virialized objects in the Universe. Their average dark matter profiles and halo masses have been measured in great detail (e.g., [65, 53, 63, 99, 89, 67]). Recent work has measured finer features of the mass distribution within and around cluster halos. The splashback radius predicted by [28] and [2] was recently detected by [74]. Halo assembly bias [101, 37, 113, 22] has also been detected by the same group [71, 74]. Evidence for cluster ellipticity from weak lensing has been measured on small samples of ~ 20 clusters [80, 30] as well as large samples of several thousand clusters [32, 12]. Similarly, filaments between individual pairs of massive clusters [29, 52] and thousands of group and cluster pairs [14] have recently been detected using weak gravitational lensing, supplementing similar measurements with the cluster galaxy distribution [116].

While this work has been accomplished with existing data such as the Sloan Digital Sky Survey[2] (SDSS), the next generation of surveys including the Dark Energy Survey[3] (DES; [70, 79, 93]), Hyper Suprime-Cam[4] (HSC, [72]) and the Kilo Degree Survey[5] (KiDS, [111]) have also begun producing results on galaxy clusters. Within a few years these new surveys will provide much larger cluster samples than were previously available.

Compared to their massive host clusters, the properties of cluster subhalos are less well-studied. Subhalos were once isolated dark matter halos, each with their own central galaxy,

[1] This work is based on the paper [33], I led or jointly did all the analysis.
[2] `http://www.sdss.org`
[3] `http://www.darkenergysurvey.org`
[4] `http://www.naoj.org/Projects/HSC/`
[5] `http://kids.strw.leidenuniv.nl`

before gravitational forces pulled them inside much larger neighboring halos. Many such accreted halos are tidally destroyed and become indistinguishable as distinct entities, but subhalos are the survivors that persist as satellites of the larger cluster halo. Since the lensing and clustering signals of subhalos are dwarfed by their massive host clusters, it is more difficult to study their detailed mass distributions. Recent progress in determining weak lensing masses of subhalos has been made by [62] using CFHT Stripe-82 data [31] and by [102] with KiDS data [57]. While simulation studies of subhalos predict that tidal forces from the host cluster will strip mass from the subhalo outskirts [43, 38], the recent lensing studies were not able to identify a tidal radius beyond which mass was stripped. However, the [62] measurements hinted that subhalos closer to the cluster center – where tidal forces are strongest – may be less massive, which would provide indirect evidence for tidal stripping.

Given the insufficient signal-to-noise (S/N) of weak lensing, correlations between subhalos within the same host provide a promising alternative way to measure tidal stripping, as demonstrated by [10] using subhalos in N-body simulations. [16] and [17] had shown the existence of such correlations and discussed a variety of consequences in physical and velocity space. [10] pointed out that subhalo-subhalo correlations can be used to address an important open question in galaxy formation: did the star formation of satellites galaxies end upon accretion? The striking color difference between galaxies in cluster and field environments – satellites are mostly "red and dead" while field galaxies are mostly blue and actively forming stars – has prompted a search for the mechanisms within clusters that end star formation in satellites. These include accretion shocks [3, 26], strangulation [60], ram-pressure stripping [41, 1], and the effect of many high-speed encounters with other satellites [34, 73] – all of which act to either forcibly remove gas from the subhalo or prevent it from cooling enough to form stars.

It is possible to reproduce many observed statistics of quiescent galaxies using models relying upon quenching of star formation caused by intra-cluster processes. For example, [114] used a galaxy group catalog from SDSS Data Release 7, combined with the quiescent fractions from COSMOS survey, and a cosmological N-body simulation to study the star formation histories of satellite galaxies at $z \approx 0$. They found that satellite quenching is consistent with the statistics of quiescent galaxies if quenching is a 'delayed-then-rapid' process: the satellites remain actively star forming for $2 - 4$ Gyr after their first infall, unaffected by the host halo, after which the quenching occurs rapidly with an SFR e-folding time < 0.8 Gyr.

Alternatively, it is also possible that other processes besides satellite quenching may be dominant in determining quiescent fractions in clusters. For example, the age-matching model of [44] can reproduce many measurements of galaxy luminosity, color, clustering, and weak lensing [45, 112] without relying on satellite quenching processes. By placing the reddest galaxies in the oldest dark matter halos – which tend to be the ones that formed in denser environments – the [44] model naturally reproduces the large red fraction seen in observations.

Possible mechanisms that can quench galaxy star formation while do not necessarily depend on intra-cluster processes include: virial shock heating of intergalactic gas falling into galactic haloes, that is, as the gas falling in, gravitational energy converts to heat that cannot be balanced out by radiative cooling; Heating by the active galactic nucleus (AGN), simply put, the supermassive black hole at a galaxy center injects energy into its surroundings while accreting material, supplying the energy to heat up or expulse cold gas.

However, recently [117] showed that the original age-matching model of [44] is in tension with measurements of the halo mass of isolated blue galaxies [68]. [117] study two quenching models and show that a model in which halo mass alone determines quenching fits the SDSS measurements [118, 68] better than a hybrid model which depends on stellar mass and host halo mass (for satellites). While both models do well at fitting red galaxy clustering and lensing, the halo quenching model is much better at modeling the halo mass for massive blue central galaxies. [117] show that the color dependence of the $\langle M_h | M_* \rangle$ relation in the publicly available mock galaxy catalogs of [45] is inconsistent with SDSS measurements, since this mock tends to place blue and red centrals of similar M_* in halos of similar mass, which is heavily disfavored by the data. It is unclear whether this conclusion can be generalized to the broader class of age-matching models, or if it is specific to the original construction of [44], since [8] argue that a slightly modified parametrization of age-matching fits the measurements of [117].

The detection of the splashback feature by [74] provides additional insight into quenching processes in clusters. More et al. detect the splashback feature in both red and blue galaxies. This shows that galaxies can complete at least one full orbit within their host clusters while remaining unquenched (i.e. blue). Given that orbital times in the outskirts of halos can be a large fraction of the Hubble time (e.g., 6 Gyr), this result may pose a challenge for the model of [114]. More et al. also find that the red fraction of cluster galaxies exhibits a pronounced feature at the splashback radius $r_{\rm sp}$. While the naive interpretation of this sharp feature at the splashback radius is that crossing $r_{\rm sp}$ modifies galaxy colors (i.e. host-quenching), similar behavior also naturally arises in age-matching models without host-quenching. In those models, the sharp feature in the red fraction is a consequence of the sharp transition at the splashback radius from the 2-halo region to the 1-halo region.

In light of these conflicting models, we carry out the subhalo-subhalo clustering measurements proposed in [10] in order to provide model-independent constraints on the relationship between subhalo infall and quenching times. Alternative models of galaxy formation may then be distinguished based on their predictions for the fraction of quiescient satellites that quenched upon accretion, rather than while isolated. We assume a flat universe and Ω_m = 0.3. In Section 2.2 we describe our SDSS data samples. In Section 2.3 we describe our method of the measurement. In Section 2.4 we describe measurement results of subhalo correlations and compare infall, dynamical, and quenching timescales for red SDSS satellites. In Section 2.5 we discuss possible systematics as well as implications of our measurements for models of galaxy formation.

2.2. redMaPPer and redMaGic Catalogs

For our subhalo sample we use members of SDSS redMaPPer clusters [92, 91]. We use clusters with redshift $0.15 < z < 0.41$ and more than ten member galaxies, i.e., we require the richness $\lambda > 10$ (note that the public catalog only goes down to $\lambda = 20$). These cuts reduce the number of clusters to 11,800. In addition to the cuts on cluster properties, we only use satellites with a membership probability `Pmem` > 0.8, ensuring that our satellite sample is pure. [91] has shown that the photometric cluster selection done by redMaPPer is effectively as good as a spectroscopic selection for those satellites with a high membership probability. We will be interested in studying the satellite clustering as a function of distance from the center of the cluster, r_c, so for this purpose we define three bins $r_c = 0.1 - 0.3$ Mpc/h, $r_c = 0.3 - 0.6$ Mpc/h, and $r_c = 0.6 - 0.9$ Mpc/h. The range in r_c for each bin was chosen to obtain sufficient signal-to-noise (S/N) in all three bins: each bin of increasing r_c has 110144, 42742, and 6728 galaxies.

We cross-correlate these subhalos with the redMaGiC galaxy catalog [90]. We use redMaGiC because many of these bright red galaxies are members of the redMaPPer clusters and may compose infalling groups with the redMaPPer members we study. We do not simply use the redMaPPer satellites because redMaPPer imposes a spatial selection around each cluster, rejecting all galaxies outside a radius $R_\lambda = 1\,\mathrm{Mpc}/h\,(\lambda/100)^{0.2}$. This might introduce edge effects in our measurement so we use the spatially uniform redMaGiC sample for cross-correlations (see Sec. 2.4 for details). The redMaGiC algorithm selects only red galaxies with good photometric redshifts with a median bias $z_{\mathrm{spec}} - z_{\mathrm{photo}}$ of 0.005 and scatter $\sigma_z/(1+z)$ of 0.017. When performing cross-correlations we select only redMaGiC galaxies within 0.02 of the cluster redshift.

For each redMaPPer member, we use SED fits to the broadband photometry to determine the age, or time since the onset of star formation. The prior on star formation history is taken to be delayed tau models [69], which produce a continuous but exponentially declining star formation history. We are most interested in when the subhalo quenched, or stopped

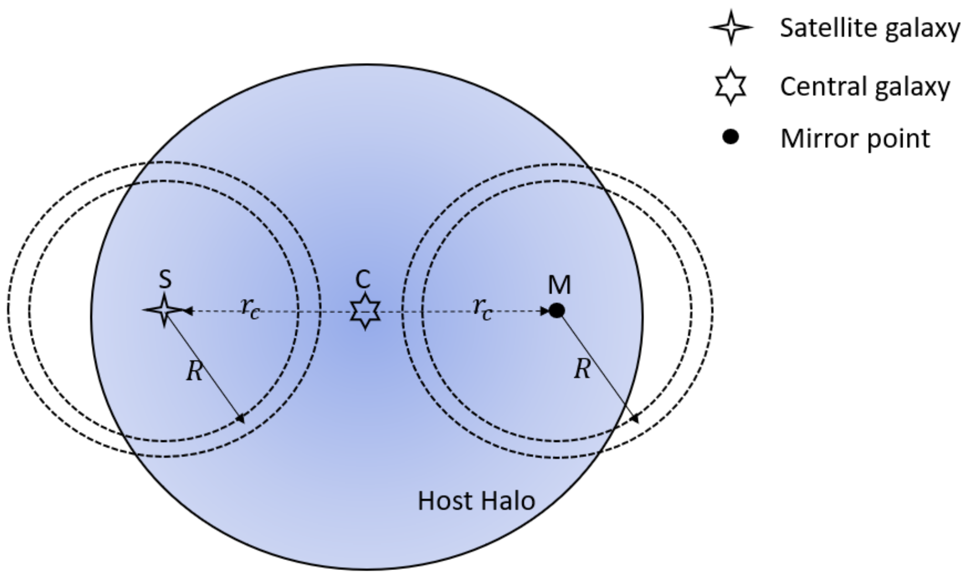

Figure 2: A sketch demonstrates geometry of the "mirror" point subtraction method that used to remove the clustering signal from the host halo. We first measure the number density of redMaGiC galaxies in annuli centered on the satellite galaxy as a function of the distance R. Then we measure the same quantity around the "mirror" point reflected about the cluster center. Our final estimator is the difference between these two number densities.

forming stars. Due to the exponential decline, it is not a bad approximation to take this measure of age as the quenching time, $t_{\rm quench} \equiv (\int {\rm d}t\ t\ {\rm SFR}(t))/\int {\rm d}t\ {\rm SFR}(t)$, where we have used the star formation rate (SFR)-weighted age. The initial mass function is taken from [94] over the range $0.1-100\,M_\odot$. See Appendix A of [75] for more details on the SED modeling. In Sec. 2.5.2 we discuss how this definition of $t_{\rm quench}$ connects with definitions used in galaxy formation models.

2.3. Isolation of Subhalo Clustering Signal

[10] used simulations to split subhalos between those that were recently accreted and those accreted more than one dynamical time ago. The dynamical time was estimated as the period for a circular orbit at radius equal to the distance from satellite to its central galaxy. The results are shown in their Figure 2: the oldest subset showed no significant correlation at large radii. In contrast, the subhalos which infell recently did show large-scale correlations.

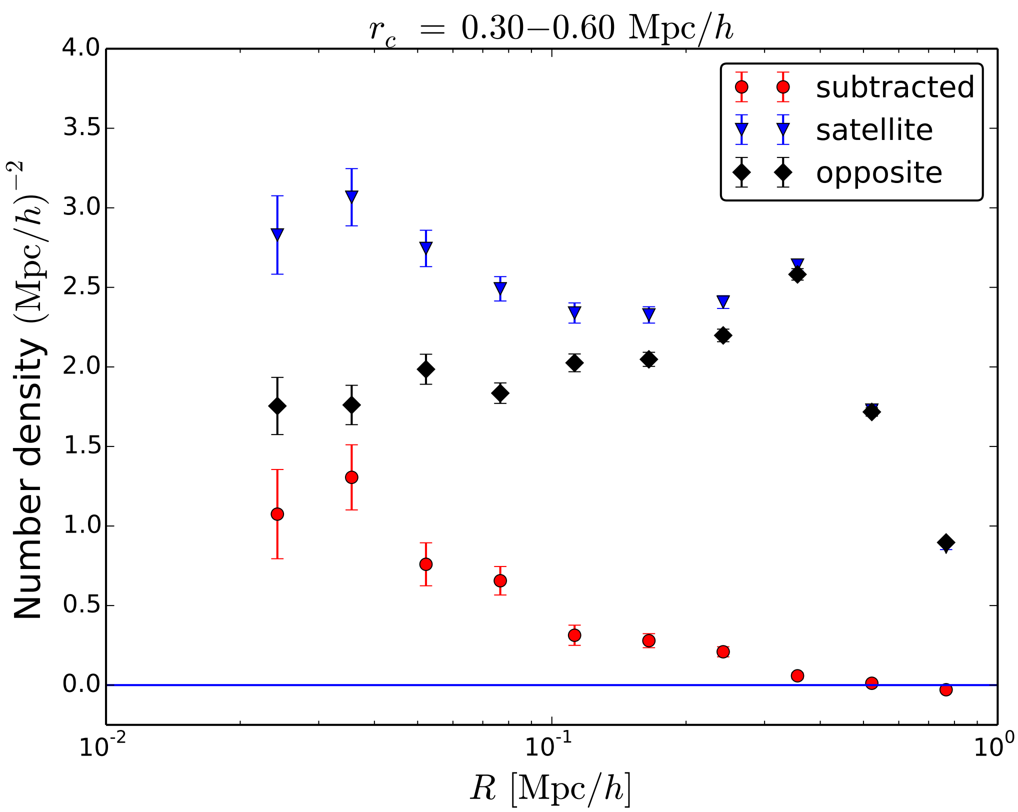

Figure 3: Number density of redMaGiC galaxies around redMaPPer members (blue points) and around their opposite positions relative to the cluster center (black points). The difference (red points) isolates the subhalo clustering signal.

This means the measurement of large-scale correlations can be used to determine when subhalos fell into their hosts. We have also tested that we recover similar results as [10], but using a larger simulation. These results are shown in Appendix A.1.

We seek to detect these large-scale correlations in data by cross-correlating subhalos (redMaPPer members) with the redMaGiC sample by counting the number of redMaGiC galaxies in annuli centered on each redMaPPer subhalo. However, since subhalos are by definition always part of a larger halo, the raw number counts measured around subhalos will be dominated by the host. In order to remove this host signal, we follow the method of [82] and [10], subtracting the counts around the subhalo's "mirror" point reflected about the cluster center. The geometry of this method is shown in Fig. 2. Since this point is at the same distance r_c from the cluster center, if the host cluster profile is spherically symmetric it will have the same contribution from the host. This method is illustrated in Fig. 3, which shows the counts around the redMaPPer satellite and the opposite point. Both are dominated by the mis-centered host signal, but after subtraction the subhalo clustering signal is clearly visible at small scales and falls smoothly to zero at large scales.

This subtracted signal is our estimator used in all remaining plots: we count redMaGiC galaxies in annuli centered on each redMaPPer subhalo, subtract the counts of redMaGiC galaxies around each mirror point, and divide by the number of subhalos. For all measurements, we divide the SDSS data into 200 spatially uniform patches and estimate a jackknife covariance by removing each patch in turn [78]. All figures show the diagonal 1σ jackknife errors while our signal-to-noise (S/N) estimates incorporate the full jackknife covariance.

Note that we measure correlations in 2D, projected bins of cluster-centric distance r_c. This is in contrast to Figure 2 of [10], which shows 3D correlations. In Sec. 2.5.1 we argue that the qualitative conclusions we draw from the 2D correlations should be similar to those based on 3D correlations. Moreover in future work we intend to present correlations in deprojected 3D cluster-centric distance bins to compare more directly with [10].

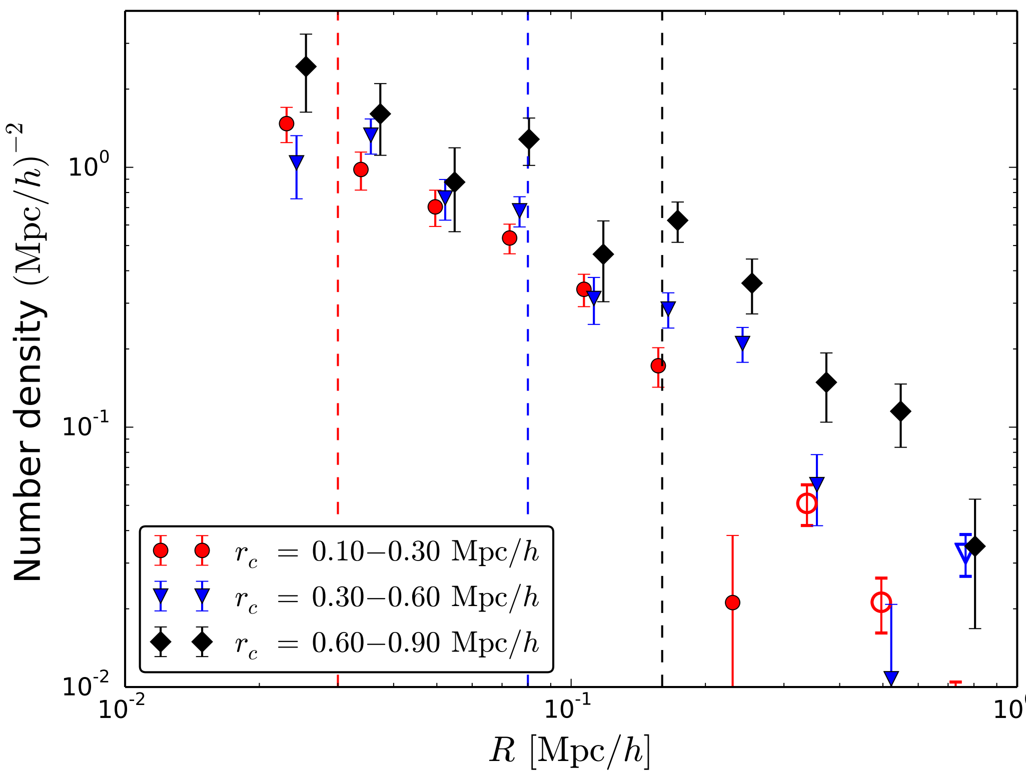

Figure 4: Projected number density of redMaGiC galaxies stacked around subhalos, for all 3 bins of cluster-centric distance r_c. Note the data points have been shifted slightly along the x-axis for clarity. Above ~ 0.1 Mpc/h there is a clear trend of increasing correlations for larger cluster-centric distance. Vertical lines show the estimated tidal radius for each subhalo sample: all measurements show signficant correlations with unbound material beyond the tidal radius.

2.4. Results

2.4.1. Correlations Beyond the Tidal Radius

In Fig. 4 we show the results for three cluster-centric radius bins, $0.1 < r_c < 0.3$, $0.3 < r_c < 0.6$, and $0.6 < r_c < 0.9$ Mpc/h. The correlations are clearly detected in each case, and fall as $\sim 1/R$ with increasing scale. Note there is an increase in correlations for larger r_c bins which may be due partly to the positive correlation of r_c with stellar mass (see Fig. 5). We also tested measurements in bins of r_c/R_{200}, where R_{200} is the host's virial radius. These results were qualitatively similar. In order to interpret the measurements of Fig. 4, we next

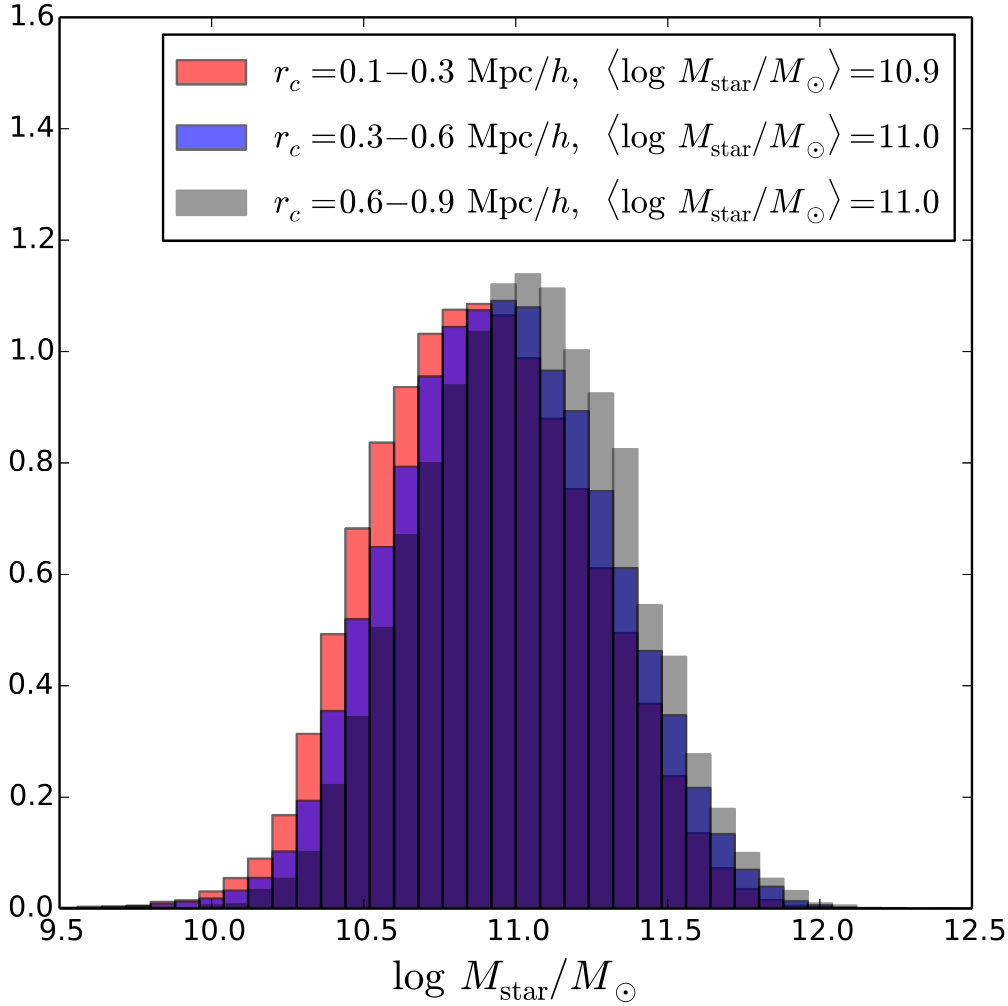

Figure 5: Normalized stellar mass distributions for the three cluster distance bins.

estimate the subhalos' tidal radius, beyond which unbound material can be stripped by tidal forces from the host.

Measuring correlations well beyond the tidal radius would indicate that at least some of the subhalos were recently accreted, since otherwise unbound material would have been stripped. The "Hill" radius, which can be used to estimate the tidal radius, is roughly the radius where $\rho_{\rm subhalo} \sim \rho_{\rm host}$ [10], where the dynamical time for particles orbiting the subhalo becomes comparable to the dynamical time for the subhalo to orbit its host. To obtain $\rho_{\rm subhalo}$ we use the results of [62], which measured lensing masses for a subset of our subhalos, those which overlap with the CFHT Stripe-82 Survey. [62] found best-fit subhalo masses $10^{11.3}$, $10^{12.0}$, and $10^{12.5} M_\odot/h$ for increasing distance from the cluster, using the same three r_c bins as our measurements.

In Fig. 6 we show NFW density profiles [76] for the three bins using these masses.

To obtain the average local host density at the satellite locations, we use the mass-richness relation of [103]:

$$M_{200} = 10^{14.344} M_\odot/h \times (\lambda/40)^{1.33} \,. \tag{2.1}$$

We then estimate $\rho_{\rm host}(r)$ using this host mass and an NFW profile, and plot the result in Fig. 6. Here r is the 3D cluster-centric distance. By assuming the host halo is spherically symmetric, and the distribution of satellites follows an NFW form, r can be estimated by

$$r(r_c) = \frac{\int_0^{\sqrt{{R_{200}}^2 - r_c^2}} \rho_{\rm nfw}(\sqrt{r_c^2 + x^2}) \times \sqrt{x^2 + r_c^2}\, {\rm d}x}{\int_0^{\sqrt{{R_{200}}^2 - r_c^2}} \rho_{\rm nfw}(\sqrt{r_c^2 + x^2})\, {\rm d}x} \,. \tag{2.2}$$

The host and subhalo density profiles cross at $r_{\rm tidal} \sim 0.03$, 0.07, and 0.15 Mpc/h for the three bins of increasing r_c. A rough comparison to the simulation results of [10] shows that our results are comparable: for their $0.4 < r_c < 0.6$ Mpc/h bin, the local host density and subhalo density match at ~ 0.045 Mpc/h (see Fig. 1 of that work). This is slightly smaller but close to the tidal radius ~ 0.07 Mpc/h that we find for subhalos between

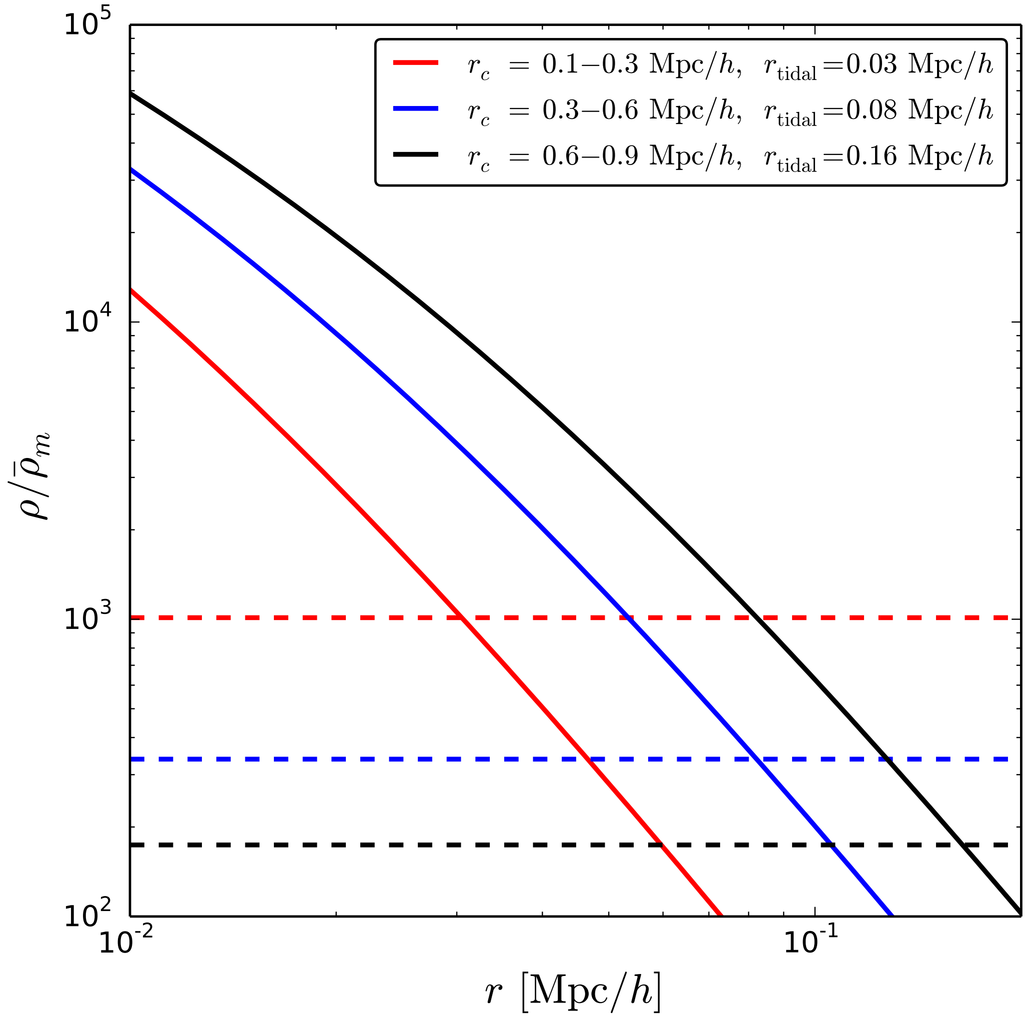

Figure 6: The subhalo profile (solid lines) and background host density (dashed lines) for each r_c bin. The estimated $r_{\rm tidal}$ is the radius where the two density profiles cross.

$0.3 < r_c < 0.6$ Mpc/h; exact agreement is not expected since we have not attempted a comparison with matched host halo masses.

Material at larger radii should be unbound, so we look for correlations beyond $r_{\rm tidal} \sim 0.03$, 0.07, and 0.15 Mpc/h, for each of the three r_c bins. Comparing these scales to Fig. 4, we do see correlations well beyond $r_{\rm tidal}$ in each case. We find the S/N using points in the range $r_{\rm tidal}$ to $r_c/2$ is 11.1, 10.3, and 6.1 corresponding to the three bins of increasing r_c. Thus all show significant detections. This implies that some of the subhalos recently fell into their hosts and there has not been enough time for unbound material to be torn away, i.e., $t_{\rm infall} < t_{\rm dyn}$, where $t_{\rm infall}$ is the infall time and $t_{\rm dyn}$ is the dynamical time. In Table 1 we also show the S/N using a wider range of scales $r_{\rm tidal} < R < r_c$, but note that points close to r_c may be subject to several systematics discussed in Section 2.5.1. In the following section we estimate the dynamical time and compare it to the quenching timescale for the subhalos.

r_c (Mpc/h)	S/N	
	$[r_{\rm tidal},\, r_c/2]$	$[r_{\rm tidal},\, r_c]$
0.1 - 0.3	11.1	14.7
0.3 - 0.6	7.1	8.8
0.6 - 0.9	6.1	6.8

Table 1: Signal-to-noise of the correlations beyond the tidal radius shown in Fig. 4. The measurement is significant regardless of cluster-centric distance r_c.

2.4.2. Dynamical and Quenching Timescales

We can estimate the dynamical time for each subhalo using its distance from the cluster center r and the host density profile. As in Sec. 2.4.1, we estimate the host density using the redMaPPer mass richness relation and assume an NFW profile. The dynamical time is then

$$t_{\rm dyn} = 2\pi\sqrt{r^3/(GM(<r))}\,, \tag{2.3}$$

where $M(< r)$ is the host mass contained within the 3D radius r, which is estimated by Eq. (2.2). In Fig. 7 we show histograms of the resulting dynamical times, for the three r_c

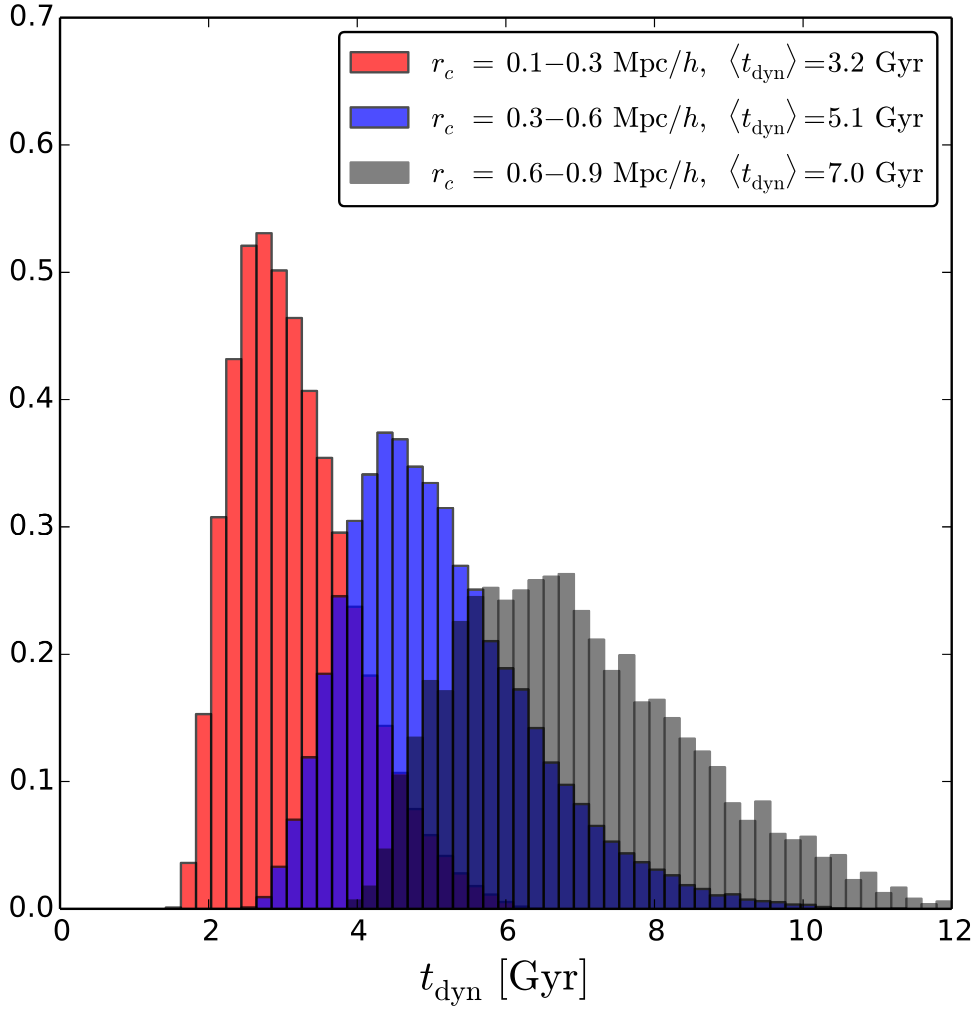

Figure 7: Distribution of dynamical times of the subhalos for each r_c bin. The dynamical time is estimated using Eq. (2.3). Here we use the redMaPPer relation and assume an NFW profile to estimate the host mass. It can be seen that the dynamical time is increasing with r_c with the mean value for the outer most bin $t_{dyn} \sim 6$ Gyr.

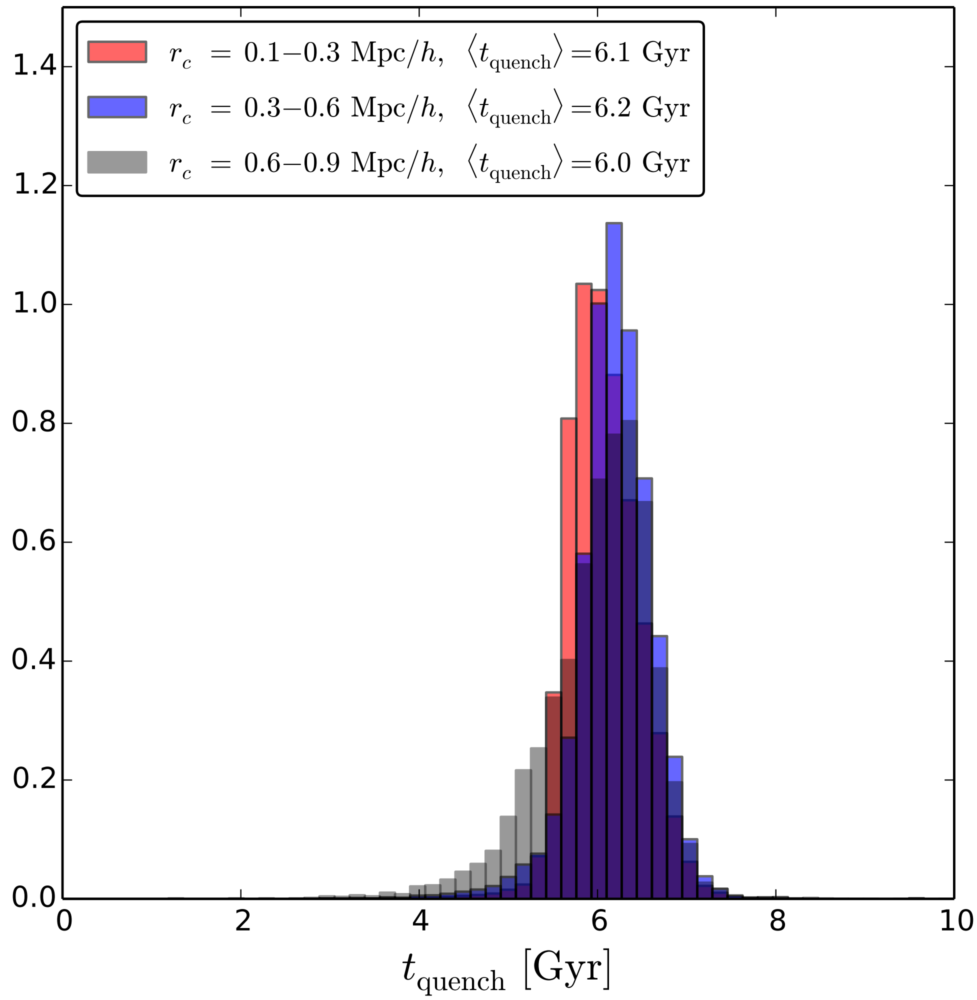

Figure 8: Quenching time since the redMaPPer subhalos stopped forming stars. For all three r_c bins, the mean quenching time is ~ 6 Gyr. Thus for the inner two r_c bins we have $t_{\rm dyn} < t_{\rm quench}$.

bins. The mean is small for the innermost bin, ~ 3 Gyr, increasing to ~ 6 Gyr for the galaxies farthest from the cluster center. This is expected due to the smaller density at larger distances from the cluster center.

We next compare these dynamical times to the quenching time determined from SED fits (see details in Sec. 2.2). In Fig. 8, we show the distribution of t_{quench} using the mean of the posterior for each subhalo. The distribution peaks at ~ 6 Gyr, a value greater than the dynamical times $\sim$ 3-4 Gyr (see Fig. 7) for subhalos with $r_c < 0.6$ Mpc/h. Thus many of our subhalos have $t_{\text{infall}} < t_{\text{dyn}} < t_{\text{quench}}$, implying that these galaxies ceased star formation long before being accreted by their hosts.

This would be inconsistent with models of star formation in which these subhalos were actively forming stars up until the time they fell into their current hosts. In such models, infall into the cluster leads to stripping of the gas and quenching of star formation. Hence such models require that $t_{\text{quench}} < t_{\text{infall}}$ for a large fraction of our subhalos.

2.4.3. Other Tests

As an additional test of the quenching scenario, we have redone the measurement using the older half of subhalos in Fig. 8, most of which have $t_{\text{quench}} > 6$ Gyr. The results are shown in Fig. 9, and again we see strong correlations well beyond the tidal radius. For a more model-independent test of age we split the subhalos into halves based on color, a proxy for age since the reddest, deadest subhalos are the ones that ceased forming stars long ago.

In Fig. 10 we show the correlations measured around the "redder" subhalos, defined as those which are redder than the redMaPPer red sequence model at that redshift. Again we see strong correlations beyond the tidal radius, for all r_c bins. Thus, many of these subhalos recently fell into their hosts, long after they had ceased forming stars.

We also tested the dependence of our results on the specific galaxy samples by measuring the auto-correlation of redMaPPer satellites. This gave similar results with correlations

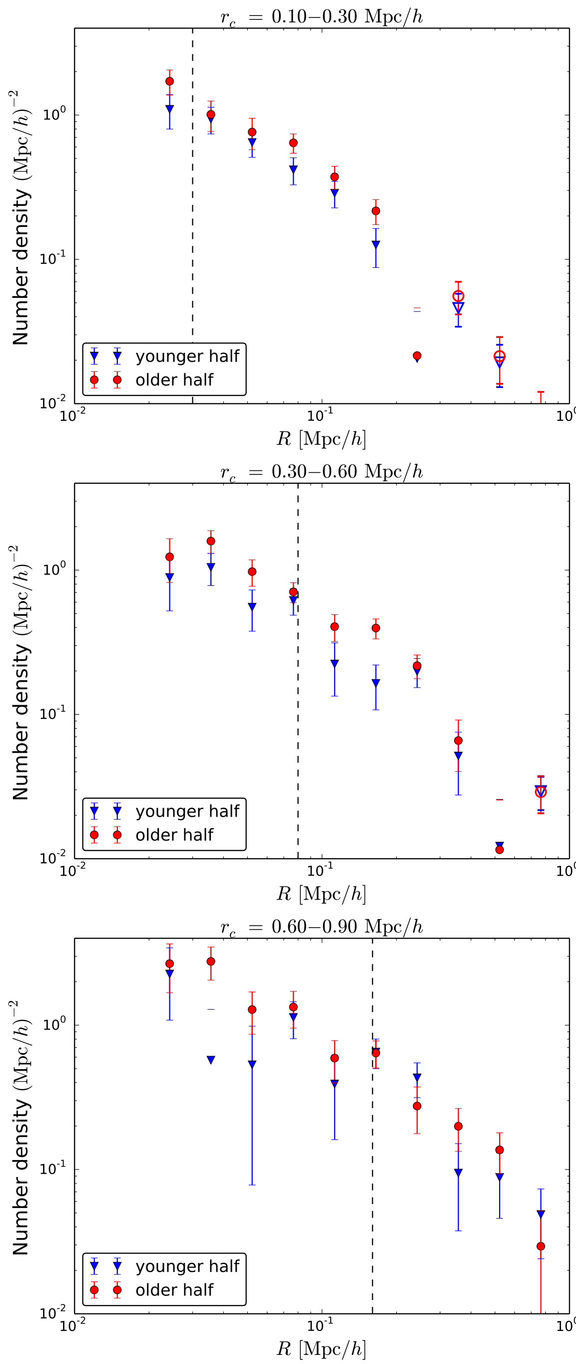

Figure 9: Comparison between correlations of older (red circles) and younger (blue triangles) subhalos, as determined from SED fit results for t_{quench}. Each panel shows results for subhalos at different distances r_c from the host cluster. Subhalos with $r_c < 0.6$ Mpc/h show correlations well beyond the tidal radius (vertical dashed line). These long-range correlations are present for both the young and old samples.

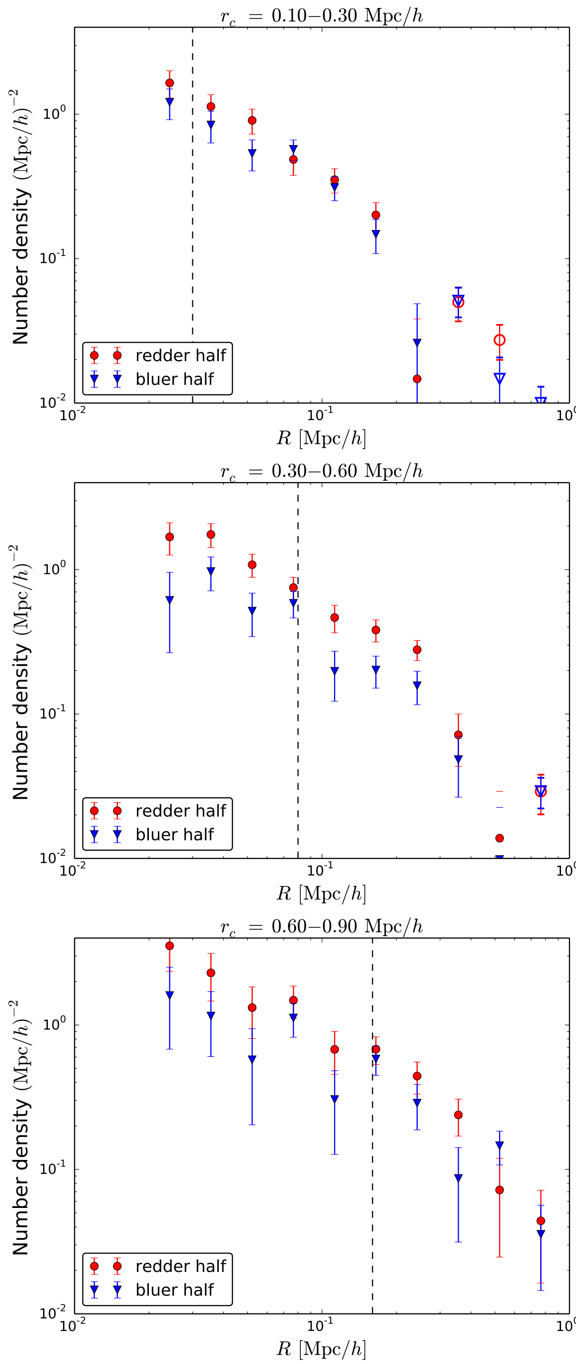

Figure 10: Same as Fig. 9 but showing subhalos split by color: those redder (red circles) and bluer (blue triangle) than the red sequence model. Since redder galaxies have been quiescent for longer, these results are similar to the t_{quench} split but less dependent on detailed SED modeling.

persisting well beyond the tidal radius. The redMaPPer satellites are dimmer than redMaGiC with a cut at $L > 0.2L_*$ instead of $L > 0.5L_*$. But redMaPPer also enforces a spatial selection around the cluster center, which may bias the redMaPPer auto-correlation for the larger r_c bins. For this reason we did not choose the auto-correlation for our fiducial measurements.

2.5. Discussion

We have shown that redMaGiC galaxies are significantly correlated with redMaPPer satellites, on angular scales exceeding the estimated tidal radii for satellites at small cluster-centric distances. This result holds even when we subselect the reddest satellites, or those believed to have been quenched for the longest times. Our measurements can be compared with the simulation results of Chamberlain et al (2015), and suggest that a significant fraction of the massive satellites in our sample were quenched prior to infall into their host cluster halos. Future studies with ongoing surveys using the clustering of satellite galaxies and their weak lensing signal can shed light on galaxy formation models and probe possible interactions of dark matter. Below, we discuss potential systematics in our measurements, and then discuss implications for satellite quenching models.

2.5.1. Possible Systematics

First, we discuss possible systematics in our measurement of correlations beyond the tidal radius. Two effects which we have neglected will become increasingly important at projected distances $\sim r_c$, i.e., near and beyond the cluster center. The first is over-subtraction of the subhalo profile. When we measure correlations around the mirror point (see Sec. 2.3 and Fig. 3) there will be some positive contribution from the subhalo, the magnitude of which will become important at scales $R \sim 2\,r_c$ when the annulus R contains the subhalo. Note that this systematic contributes with negative amplitude due to the subtraction and so does not weaken our case for the detection of subhalo correlations beyond the tidal radius.

A second effect could result from systematic cluster miscentering. If the true cluster center is on average closer to the subhalo than redMaPPer's most probable center, then the subtraction of the mirror point signal will imperfectly remove correlations due to the host cluster. This would contribute most strongly at larger scales $R \sim r_c$: as seen in Fig 3, the cluster signal as measured around the opposite point is roughly flat within $R \sim r_c/2$, then begins rising to peak at $R \sim r_c$ before decreasing again. Thus residuals of the subtracted cluster signal could cause a roughly constant systematic below $r_c/2$ and increase in magnitude at larger scales. We found no evidence of such a trend in our measurements. Note that we only use clusters with a center that is both (i) the most likely center for that cluster and (ii) truly looks like a central: these are galaxies which are bright, red, and near the center of the spatial distribution of cluster members. See [92] for more information on the redMaGiC centering filter and [88] for further tests of redMaPPer centering, including comparison to X-ray centers for a subset of clusters.

Due to imprecise line-of-sight information on galaxy positions, some fraction of the redMaPPer members may lie outside the halo. Assuming this interloper component has a constant spatial density, it will be most important at large r_c since the profile of actual cluster galaxies drops with distance from the cluster center. According to [91], the fraction of such interlopers is estimated to be 6% averaged over the whole cluster. If interlopers were responsible for much of the signal we detect, the measured angular correlation for neighbors around redMaPPer galaxies at small r_c would be $\sim 16\times$ smaller than the analogous correlation function at $r_c \gg r_{\rm vir}$. We do not find this, so conclude that interlopers are not a significant factor in our analysis.

The previous paragraph discussed the effect of projections of distant interlopers, next we discuss the effect of two types of less catastrophic projections. First, we measure correlations with redMaGiC galaxies in 2D projected distance (i.e., the x-axis of Fig. 4 is a projected quantity). [10] showed that results for subhalo-subhalo correlations in 3D and in projection are qualitatively similar. For example, in their Figures 3 and 4, they show that 3D and projected correlations show the same features between different cluster-centric distance bins. Thus, we do not worry further about this type of projection effect. Second, we use 2D cluster-centric bins r_c, meaning that each r_c bin contains subhalos over a range of larger 3D distances. In this paper, we have partially accounted for this effect by estimating the average 3D cluster-centric distance via Eq. (2.2), and using that mean 3D quantity to estimate $r_{\rm tidal}$ and $t_{\rm dyn}$. In addition, we have carried out a deprojection of our angular correlations for the two lower r_c bins; preliminary results suggest that the long-range correlations persist. We will present a quantitative comparison of our deprojected correlations with galaxy formation models in a separate study.

2.5.2. Implications for Models of Galaxy Formation

We have argued that the absence of tidal stripping favors isolated quenching of a significant fraction massive galaxies, prior to their infall into galaxy clusters. Here we compare our results to host-quenched fractions predicted by more specific models of galaxy formation. The model of [114] predicts a strong dependence of the host-quenched fraction with subhalo stellar mass and host halo mass. Our clusters have mass $\gtrsim 10^{14} M_\odot/h$, comparable to the most massive cluster bin studied by [114]. In Fig. 5 we show our subhalo stellar mass distributions: all three bins have similar distributions with mean mass $\sim 10^{11} M_\odot$, with a very slight shift to larger stellar mass for larger r_c. For this host mass and subhalo stellar mass, Fig. 10 of [114] indicates that 55% of quiescent satellites quenched as satellites (40% in the current host and 15% as satellites of a prior host; 45% quenched while isolated). This estimate appears to be consistent with our findings that a large fraction of redMaPPer satellites quenched prior to entering their current hosts. It will be interesting, therefore, to perform the same measurement for satellites with lower stellar masses, where the Wetzel et al. model predicts nearly $\sim 100\%$ quenched as satellites. Such measurements should be possible with ongoing imaging surveys like DES, HSC or DECALS, or future surveys like LSST. Within the range of satellite stellar masses in our data (see Figure 8), we have split the sample into two with median stellar masses of about 4.6×10^{10} and $1.7 \times 10^{11} M_\odot/h$. The results are shown in Fig. 11; it is evident that deeper imaging data that obtains cluster satellites with lower stellar mass is needed to explore possible trends.

Another reason it will be interesting to pursue similar measurements for lower-mass galaxies is that the [114] model requires a delay between the time when star forming satellites fell into their first host and the time when their star formation began to exponentially decay. Their Figure 8 shows that this delay time is ~ 2.5 Gyr for our subhalos. Since our SED fits imply that $t_{\rm quench} \sim 6$ Gyr, the [114] model would predict that first infall occured ~ 8.5 Gyr ago (i.e. at $z > 1$) in order for satellites to be host-quenched. We see no evidence for such high redshifts of infall. For satellites with $M_\star \sim 10^{11} M_\odot$, a large fraction are predicted to quench as centrals, so our measurements are not inconsistent with the model's predictions. However, if we find similar results for satellites with $M_\star \sim 10^{10} M_\odot$, it will be difficult to reconcile that behavior with host quenching models like the Wetzel et al. model in which nearly 100% of objects quenched as satellites. One possible solution to this problem is if a significant fraction of the red satellites quenched as satellites of previous (smaller) hosts, rather than their current hosts. For the host-satellite properties that match our data, [114] estimate that only $\sim 15\%$ of such galaxies quenched as satellites in hosts different than their current hosts, and it is unclear whether this small fraction would be sufficient to account for the correlations observed in our sample. We intend to address some of these open questions in a future study that includes the use of deprojected, 3D correlations of satellites for quantitative comparisons with theoretical models.

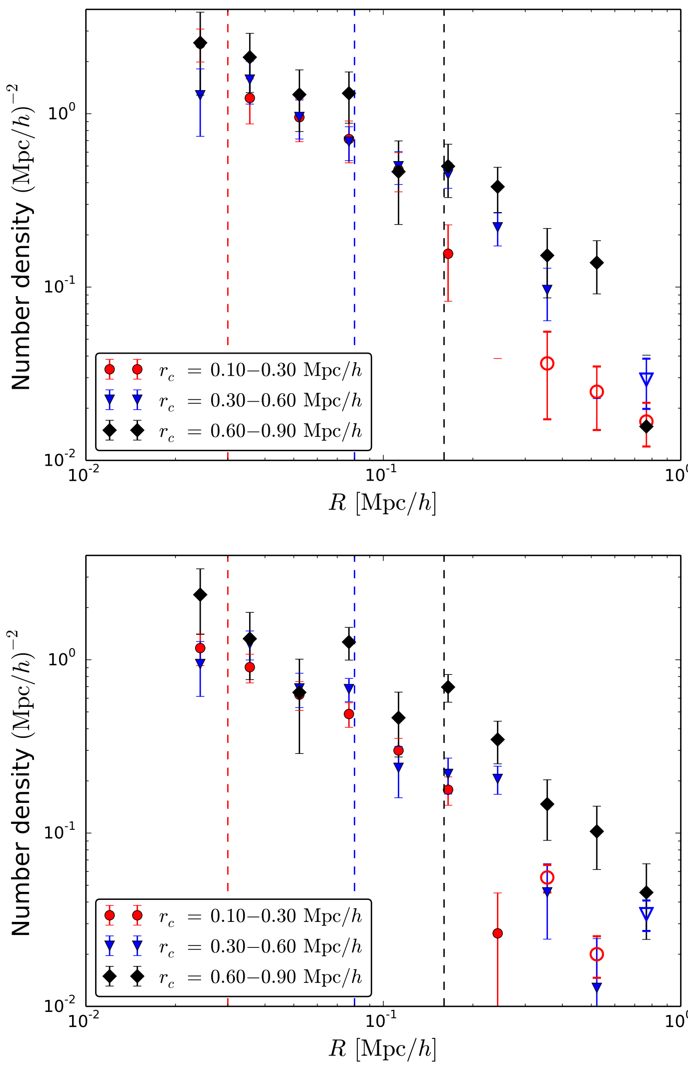

Figure 11: Projected number density as in Fig. 2, but split by satellite stellar mass: higher (upper panel) and lower (lower panel) than $10^{11} M_{\odot}/h$.

CHAPTER 3 : Galaxy-galaxy Lensing[1]

3.1. Introduction

Weak gravitational lensing refers to the subtle distortions in the shape of images of distant galaxies by intervening structures along the line of sight. The measurement of cross-correlation between foreground (lens) galaxy positions and the lensing shear of background (source) galaxies is referred to as galaxy-galaxy lensing ([109], [6], [27]). The component of the shear that is tangential to the line connecting the lens and source galaxies are binned in annuli on the sky centered on lens galaxies to get a measurement as a function of angular separation, which is a measure of the average, projected, excess mass profile around the lens galaxies.

Galaxy-galaxy lensing at small scales can be used to infer the mass distribution within the dark matter haloes where the lens galaxies reside, while at large scales it measures the galaxy-mass cross-correlation. It has many applications, ranging from fitting Navarro-Frenk-White (NFW) halo mass profiles ([76]) to constraining large-scale galaxy bias and cosmological parameters ([7], [64], [74], [58]). Recent surveys such as CFHTLenS ([46], [31]) have used galaxy-galaxy lensing to study properties of dark matter haloes that host galaxies ([39], [110], [48]). The galaxy-mass connection has been studied in [100] and [66] using galaxy-galaxy lensing.

In this work, we introduce methodology of measuring galaxy-galaxy lensing signal from both Science Verification (SV) and Year one (Y1) data of the Dark Energy Survey (DES). DES is an ongoing wide-field multi-band imaging survey that will cover 5000 sq. deg. of Southern sky over five years of observation. We focus on several tests of systematics of our measurement pipeline and validation of estimating the covariance matrix. The detailed tests

[1]This work is based on the paper [15], My contribution to the paper was primarily in sections 5.1 and 5.2 about the tests of systematics. This work is also based on the [87], My contribution to the paper was primarily in section C about the validation of the covariance estimation.

and validation presented in this work will serve as a foundation for future work relying on galaxy-galaxy lensing measurements, such as the cosmological analysis and Halo Occupation Distribution (HOD) analysis.

The plan of this chapter is as follow. In Section 3.2 we present details of the measurement methodology with our estimator of galaxy-galaxy lensing. Several tests of potential systematic effects on the measurement are shown in Section 3.3. Section 3.4 describes a set of log-normal simulations and how it be used to validate our estimation of covariance matrix. We conclude in Section 3.5.

3.2. Measurement Methodology

Here we describe the details of the tangential shear measurement $\langle\gamma_t\rangle$. Similarly, we can measure the cross-component of the shear $\langle\gamma_\times\rangle$, which can be used as a useful test of possible systematic errors in the measurement as it can not be produced by gravitational lensing. For a given lens-source galaxy pair j, we define the tangential (e_t) and cross ($e_\times$) components of the ellipticity of the source galaxy as

$$e_{t,j} = -\mathrm{Re}[\mathrm{e_j e^{-2i\phi_j}}], \mathrm{e_{\times,j}} = -\mathrm{Im}[\mathrm{e_j e^{-2i\phi_j}}] \tag{3.1}$$

where $e_j = e_{1,j} + ie_{2,j}$, with $e_{1,j}$ and $e_{2,j}$ being the two components of the ellipticity of the source galaxy measured with respect to a Cartesian coordinate system with its origin set on the lens galaxy, and ϕ_j being the position angle of the source galaxy with respect to the horizontal axis of the Cartesian coordinate system. Assuming the intrinsic ellipticities of individual source galaxies are randomly orientated, we can obtain the mean weak lensing shear $\langle\gamma_{t/\times}\rangle$ by averaging the ellipticity measurements for each component over many such lens-source pairs. However, note that the assumption about the randomness of orientations of source galaxies can be broken by intrinsic galaxy alignments (IA), which will lead to non-lensing shape correlations (e.g. [108]), which are included in the modeling of the combined probes cosmology analysis. Then:

$$\langle \gamma_\alpha(\theta) \rangle = \frac{\sum_j w_j e_{\alpha,j}}{\sum_j w_j} \tag{3.2}$$

where θ is the angular separation, $\alpha = t$ or $\times$ denotes the two possible components of the shear, and $w_j = w_l w_s w_e$ is a weight associated with each lens-source pair, which will depend on the lens, on the source weight assigned by the shear catalog and on a weight assigned by the estimator. These estimates need to be corrected for shear responsivity (in the case of METACALIBRATION shear catalog) or multiplicative and additive bias (in the case of IM3SAHPE catalog). Also note that in this work we set $w_e = 1$ because we are using the γ_t estimator, which weights all sources uniformly. Another option would be to choose an optimal weighting scheme that takes into account the redshift estimate of the source galaxies to maximize the lensing efficiency, as it is the case of the $\Delta\Sigma$ estimator. In the context of a cosmological analysis combining galaxy-galaxy lensing and cosmic shear, using uniform weighting for the sources has the considerable advantage that nuisance parameters describing the systematic uncertainty of shear and redshift estimates of the sources are the same for both probes.

In all measurements in this work, we average the shears for galaxy pairs in 20 log-spaced angular separation bins between 2.5 and 250 arcmin. We use **TreeCorr**[2] ([50]) to compute all galaxy-galaxy lensing measurements in this work.

3.2.1. METACALIBRATION Responses

In the METACALIBRATION shear catalog ([49], [98]), shears are calibrated using the measured response of the shear estimator to shear, which is usually the ellipticity $\boldsymbol{e} =$

[2]https://github.com/rmjarvis/TreeCorr

(e_1, e_2). Expanding this estimator in a Taylor series about zero shear

$$\begin{aligned} \boldsymbol{e} &= \boldsymbol{e}|_{\gamma=0} + \left.\frac{\partial \boldsymbol{e}}{\partial \boldsymbol{\gamma}}\right|_{\gamma=0} + \ldots \\ &\equiv \boldsymbol{e}|_{\gamma=0} + \boldsymbol{R}_\gamma \gamma + \ldots, \end{aligned} \tag{3.3}$$

we can define the shear response $\boldsymbol{R}_\gamma$, which can be measured for each galaxy by artificially shearing the images and remeasuring their ellipticity:

$$R_{\gamma,i,j} = \frac{e_i^+ - e_i^-}{\Delta\gamma_j}, \tag{3.4}$$

where e_i^+, e_i^- are the measurements made on an image sheared by $+\gamma_j$ and $-\gamma_j$, respectively, and $\Delta\gamma_j = 2\gamma_j$. In the Y1 METACALIBRATION catalog, $\gamma_j = 0.01$. If the estimator $\mathbf{e}$ is unbiased, the expected response matrix $\langle R_{\gamma,i,j} \rangle$ will be equal to the identity matrix.

Then averaging Equation. 3.3 over a sample of galaxies and assuming the intrinsic ellipitcities of galaxies are randomly oriented, the mean shear can be expressed as:

$$\langle \gamma \rangle \approx \langle \boldsymbol{R}_\gamma \rangle^{-1} \langle \boldsymbol{e} \rangle \tag{3.5}$$

It is important to note that any shear statistic will be effectively weighted by the same responses. Therefore, such weighting needs to be included when averaging over quantities associated with the source sample.

Besides the shear response correction described above, in the METACALIBRATION framework, when making a selection on the original catalog using a quantity that could modify the distribution of ellipticities, for instance a cut in S/N, it is possible to correct for selection effects. This is performed by measuring the mean response of the estimator to the selection, repeating the selections on quantities measured on sheared images. Following on the example of the mean shear, the mean selection response matrix $\langle \boldsymbol{R}_s \rangle$ is

$$\langle R_{S,i,j} \rangle = \frac{\langle e_i \rangle^{S+} - \langle e_i \rangle^{S-}}{\Delta \gamma_j}, \tag{3.6}$$

where $\langle e_i \rangle^{S+}$ represents the mean of ellipticities measured on images without applied shearing in component j, but with selection based on parameters from positively sheared images. $\langle e_i \rangle^{S-}$ is the analogue quantity for negatively sheared images. In the absence of selection biases, $\langle \boldsymbol{R}_s \rangle$ would be zero. Otherwise, the full response is given by the sum of the shear and selection response:

$$\langle \boldsymbol{R} \rangle = \langle \boldsymbol{R}_\gamma \rangle + \langle \boldsymbol{R}_S \rangle \tag{3.7}$$

The application of the response corrections depends on the shear statistics that is being calibrated; a generic correction for the two point functions, including the tangential shear, which is our particular case of interest, is derived in [98]. In this work we make use of two approximations that significantly simplify the calculation of the shear responses. First, in principle we should take the average in Equation. 3.7 over the sources used in each bin of θ, but we find no significant variation with the angular separation θ and use a constant value. Therefore, the correction to the tangential shear becomes just the average response over the ensemble, with no spatial dependence. Second, we assume the correction to be independent of the relative orientation of galaxies, so that we do not rotate the response matrix as we do with the shears in Equation. 3.1. Overall, our simplified estimator of the tangential shear for METACALIBRATION, which replaces the previous expression from Equation. 3.2 is:

$$\langle \gamma_{t,\mathrm{mcal}} \rangle = \frac{1}{\langle R_\gamma \rangle + \langle R_S \rangle} \frac{\sum_j w_{l,j} e_{t,j}}{\sum_j w_{l,j}}, \tag{3.8}$$

summing over lens-source or random-source pairs j and where $w_{l,j}$ are the weights associated with the lenses.

3.2.2. IM3SHAPE Calibration

For the IM3SHAPE shear catalog, additive and multiplicative corrections need to be implemented in the following manner, replacing the previous expression from Equation. 3.2:

$$\langle \gamma_{t,\mathrm{im3shape}} \rangle = \frac{\sum_j w_{l,j} w_{s,j} e_{t,j}}{\sum_j w_{l,j} w_{s,j} (1 + m_j)}, \tag{3.9}$$

summing over lens-source or random-source pairs j, where m_j is the multiplicative correction and the additive correction c_j has to be applied to the Cartesian components of the ellipticity, before the rotation to the tangential component, defined in Equation. 3.1, has been performed. $w_{l,j}$ are the weights associated with the lenses and $w_{s,j}$ the ones associated with the source galaxies in the IM3SHAPE catalog.

3.2.3. Random Points Subtraction

One advantage of galaxy-shear cross-correlation over shear-shear correlations is that additive shear systematics (with constant γ_1 or γ_2) will average to zero in the tangential coordinate system. However, this cancellation only occurs when sources are distributed isotropically around the lens and additive shear is spatially constant, two assumptions that are not accurate in practice, especially near the survey edge or in heavily masked regions, where there is a lack of symmetry on the distribution of source galaxies around the lens. To remove this additive systematics robustly, we also measure the tangential shear around random points: such points are randomly distributed with neither net lensing signal nor clustering, yet they sample the survey edge and masked regions in the same way as the lenses, and they are with high number density to make sure not introducing considerable shape noise at small scales. Our full estimator of tangential shear can then be written as:

$$\langle \gamma_\alpha(\theta) \rangle = \langle \gamma_\alpha(\theta)_{\mathrm{Lens}} \rangle - \langle \gamma_\alpha(\theta)_{\mathrm{Random}} \rangle \tag{3.10}$$

Besides accounting for additive shear systematics, removing the measurement around random points from the measurement around the lenses has other benefits, such as leading to a significant decrease of the uncertainty on large scales, as was studied in detail in [104].

This measurement, using a set of random points with 10 times as many points as lens galaxies, is shown in Fig. 12. Even though this is a correction included in the measurement, it is nonetheless useful to confirm that it is small at all scales used in the analysis. The measurement tests the importance of systematic shear which is especially problematic at the survey boundary, and allows us to compare the magnitude of the systematic shear with the magnitude of the signal around actual lens galaxies. We find the tangential shear around random points to be a small correction, consistent with the null hypothesis, as it is seen in the left panel of Fig. 13.

Even though the random point subtraction is a mild correction to the signal, it has an important effect on the covariance matrix. Subtracting the measurement around random points removes a term in the covariance due to performing the measurement using the overdensity field instead of the density field, as it was studied in detail in [104]. As seen in Fig. 13, we observe this effect on scales larger than 20 arcmin., where the covariance is no longer dominated by shape noise. When subtracting the measurement around random points, we detect both a significant decrease on the uncertainty of the tangential shear (top right panel) and a reduction of the correlation between angular bins (lower panels).

Finally, another argument that strongly favors applying the random points subtraction is the following. In Sec. 3.4 we validated the jackknife method using log-normal simulations, showing that the uncertainties on the tangential shear are compatible when using the jackknife method and when using the true variance from 1200 independent **FLASK** simulations (Fig. 17). We have performed this comparison both with and without the random point subtraction, finding that where is only agreement between the different methods when the tangential shear around random points is removed from the signal.

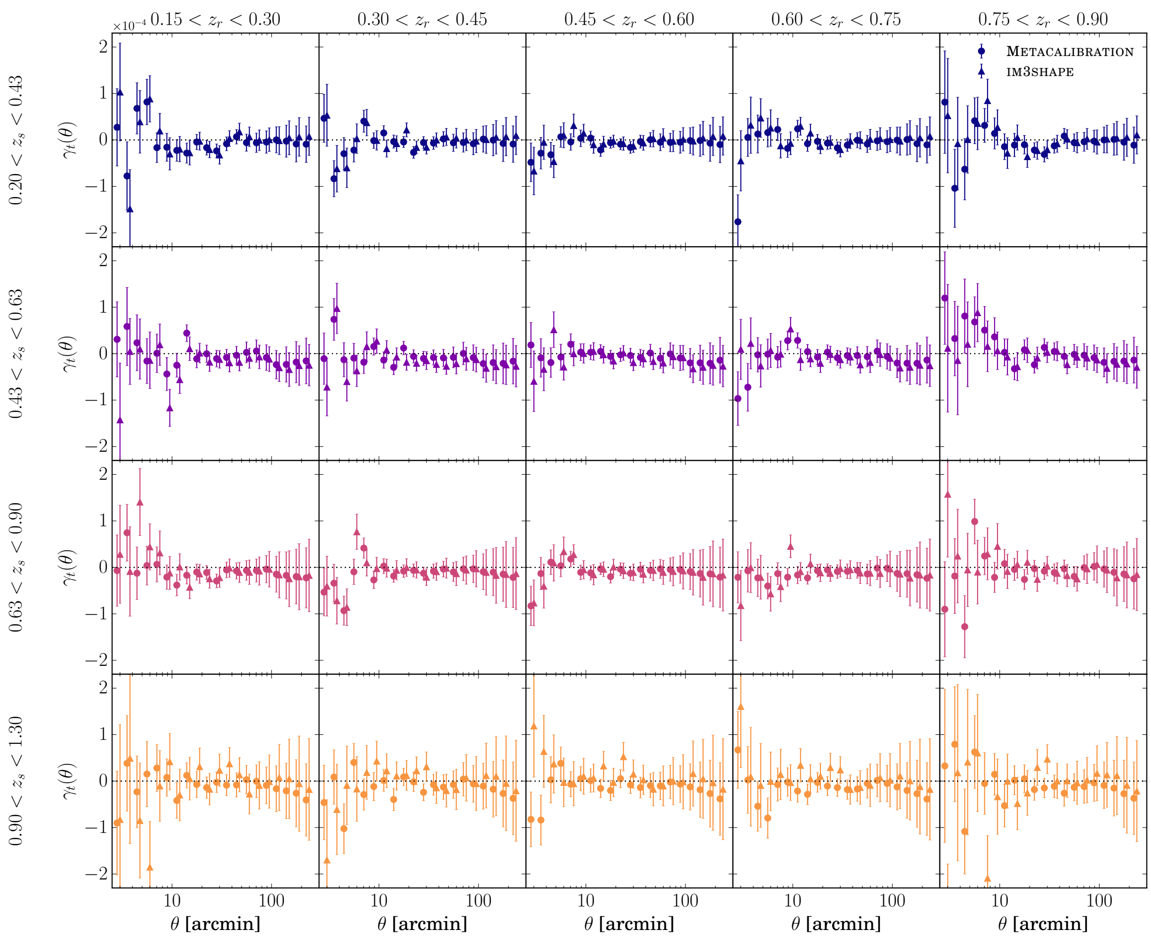

Figure 12: Tangential shear around random points for METACALIBRATION and IM3SHAPE.

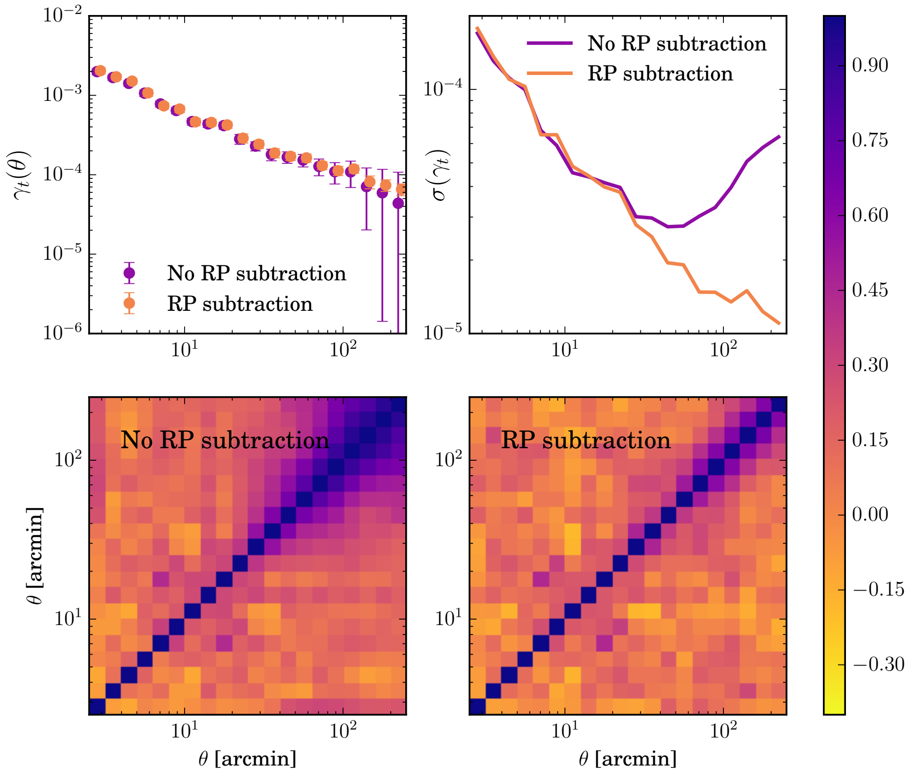

Figure 13: We show the impact the random point subtraction has on the tangential shear measurement and its corresponding jackknife covariance matrix for an example redshift bin ($0.3 < z_l < 0.45$ and $0.63 < z_s < 0.90$ for METACALIBRATION)

3.3. Systematic Tests

In this section, we demonstrate methods for testing different kinds of systematics in galaxy-galaxy lensing measurements. All figures shown in this section are using Dark Energy Survey (DES) Science Verification (SV) data. In order to quantify the comparison of the data tests in this section with the null hypothesis, we compute the null χ^2 for each of them in the following way:

$$\chi^2_{\text{null}} = \sum_{i,j} \mathbf{y}^{\mathrm{T}}(\mathbf{C}^{\text{stat}})\mathbf{y} \tag{3.11}$$

where y_i corresponds to γ_i, and $\mathbf{C}^{\text{stat}}$ is the corresponding covariance matrix. A list of null χ^2 value for each of the tests can be found in Table 2. While χ^2 is a helpful statistic, it is possible that two tests, each with the same χ^2 values, could indicate different levels of systematic error. Thus, we also perform a single parameter, constant fit to the data for each test.

Test	Lens redshift	χ^2/ndf	NGMIX Systematic uncertainty	χ^2/ndf	IM3SHAPE Systematic uncertainty
Cross-component	Medium	8.3/13	$(6.7 \pm 5.1) \times 10^{-5}$	10.9/13	$(6.0 \pm 7.8) \times 10^{-5}$
PSF leakage	Medium	16.4/13	$(0.1 \pm 3.5) \times 10^{-5}$	13.3/13	$(1.5 \pm 1.1) \times 10^{-5}$
Random points	Medium	16.4/13	$(0.4 \pm 2.8) \times 10^{-5}$	7.2/13	$(2.0 \pm 3.6) \times 10^{-5}$
Flip lens-source	High	12.0/13	$(0.6 \pm 1.8) \times 10^{-5}$	8.7/13	$(1.2 \pm 1.9) \times 10^{-5}$

Table 2: Summary of all test results described in Section 3.3. We show reduced χ^2 and constant fit for all tests.

3.3.1. Cross Component and PSF Leakage

In the cross component test, we measure the stacked lensing signal of $\gamma_\times(\boldsymbol{\theta})$ defined in Equation. 1.20, which describe the shear component at 45° to the axis that is tangential to the line connected the lens and source galaxy. Since gravitational lensing can only generate the tangential component γ_t of the shear, the cross component should be compatible with zero if there is no systematic error in the shape measurement.

The observed shapes can be seen as convolutions of the true shape and the PSF, so it is important for any shape measurement pipeline to accurately model the PSF pattern.

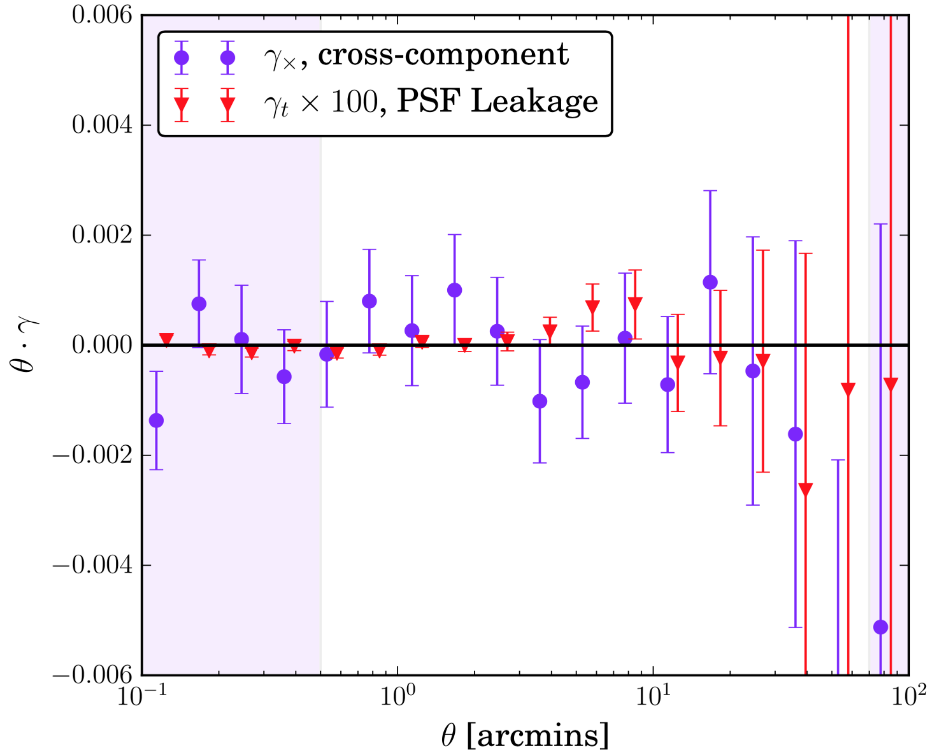

Figure 14: Cross component of the shear(purple) and measured tangential shear signal using interpolated PSF at source positions(red). In the white region, both tests pass with constant fits consistent with zero. The PSF leakage result shown here is multiplied by 100.

However, this process is imperfect: based on tests in [51], ~ 1 per cent of the PSF shape may 'leak' into the measured galaxy shape for NGMIX shear pipeline ([97]). To test the PSF leakage, we measure the stacked lensing signal of tangential shear of the PSF interpolated to the source galaxy locations.

In Fig. 14, we show the results for the both tests described above. They are measured around the DES SV redMaGiC galaxies, and are consistent with a constant fit equal to zero.

3.3.2. Random Point Shear and Flip Lens-source Sample

The signal around random points is subtracted in our estimator of galaxy-galaxy lensing defined in Eq. 3.10, in order to remove additive systematics near the edge of the survey. It

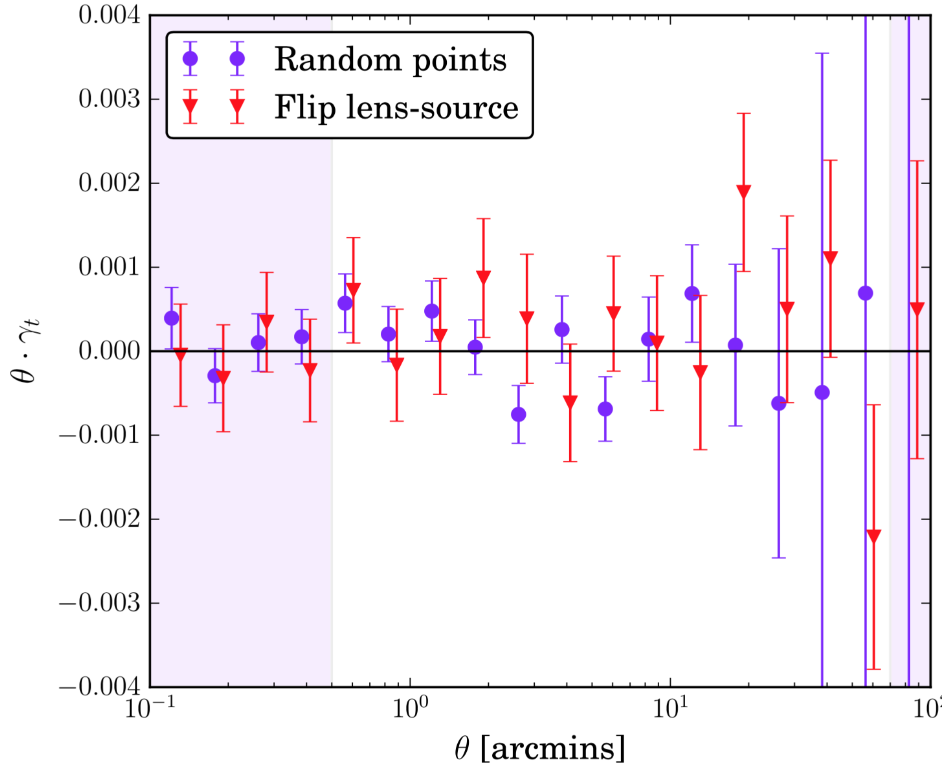

Figure 15: Tangential shear signal around random points(purple) and tangential shear of foreground sources measured around background lenses (red). In the white region, both tests pass with constant fits consistent with zero.

is nonetheless useful to confirm this correction is small and to compare its magnitude to the magnitude of the signal around actual lens galaxies.

Only background source galaxies will be lensed by the foreground lens galaxies. However, for photometric survey like DES, in the presence of errors in redshift estimation, some low redshift sources will mistakenly be put behind the lenses, and vice versa. To test how bad the photo-z error can affect our galaxy-galaxy lensing measurement, we measure the tangential shear by using sources with lower redshift ($0.2 < z_S < 0.5$) and lenses at higher redshift ($0.5 < z_L < 0.8$).

In Fig. 15, we show the results for the both tests described above. We find they are consistent with the null hypothesis.

3.4. Covariance Estimation and its Validation

3.4.1. Log-normal Simulation

Log-normal random fields are widely used in cosmology to model the distribution of matter in the Universe. It has been shown to accurately reproduce two-point statistics such as galaxy clustering and galaxy-galaxy lensing on sufficiently large scales. [19] was among the first to study how usual statistic quantities would behave if the density fluctuations were described by log-normal random field. [47] showed that the log-normal approximation yields realistic covariances in N-body simulations of weak lensing. Moreover, it is significantly less expensive in terms of computational time to generate log-normal mock catalogs than to perform N-body simulations.

In this work, we use the publicly available code **FLASK** (*Full-sky log-normal Astro-fields Simulation Kit*, [115]), to generate mock catalogs for both lens galaxies and source fields. The maps are pixelated on a **HEALPix** grid with resolution set by an N_{side} parameter of 4096, which corresponds to pixel size of 0.73 arcmin^2. We have generated 150 full-sky shear and density catalogs. For each full-sky mock, we mask out regions of the grid to then produce 8 DES Y1 footprint. After matching the number density of the mock tomographic bins to those of the data and adding shot noise, we get a total of 1200 mock surveys that mimic our observed sample.

3.4.2. Validate Jackknife Covariance

Galaxy-galaxy lensing measurements are generally correlated across angular bins. The correct estimation of the covariance matrix is crucial not only in the usage of these measurements for cosmological studies but also in the assessment of potential systematic effects that may contaminate the signal. While a validated halo-model covariance is used for the DES Y1 multiprobe cosmological analysis [56], in this work we use jackknife (JK) method to get the covariance matrices. A set of 1200 log-normal simulations, described in Section 3.4.1, is used to validate the jackknife approach in the estimation of the galaxy-galaxy lensing covariances. We estimate the JK covariance using the following expression:

$$C_{ij}^{\mathrm{JK}}(\gamma_i, \gamma_j) = \frac{N_{\mathrm{JK}} - 1}{N_{\mathrm{JK}}} \sum_{k=1}^{N_{\mathrm{JK}}} (\gamma_i^k - \bar{\gamma}_i)(\gamma_j^k - \bar{\gamma}_j) \tag{3.12}$$

where the complete sample is split into a total of N_{JK} regions, γ_i represents either $\gamma_t(\theta_i)$ or $\gamma_x(\theta_i)$, γ_i^k denotes the measurement from the k^{th} realization and the i^{th} angular bin, and $\bar{\gamma}_i$ is the mean of N_{JK} resamplings.

Jackknife regions are obtained using the **kmeans**[3] algorithm run on a homogeneous random point catalog with the same survey geometry and, then, all split in $N_{\mathrm{JK}} = 100$ subsamples. Specifically, **kmeans** is a clustering algorithm that subdivides n objects into N groups (See Appendix B in [105] for further details).

In the upper panels of Fig. 16 we present the different covariance estimates considered in this work, namely the jackknife covariance in the data (**Data JK**), the mean of 100 jackknife covariances measured on the log-normal simulations (**FLASK JK**) and the true covariance from 1200 log-normal simulations (**FLASK True**), for a given lens-source redshift bin combination ($0.3 < z_l < 0.45$ and $0.63 < z_s < 0.90$). On the lower panels of this figure, we show the differences between them normalized by the corresponding uncertainty. The lower left panel shows the distribution of these differences and its agreement with a normal distribution with $\mu = 0$ and $\sigma = 1$, as expected from a pure noise contribution, using all possible lens-source bin combinations, and the lower middle and right panels show the same quantity element-by-element for the redshift bin combination used in the upper panels. The uncertainty on the data jackknife covariance comes from the standard deviation of the jackknife covariances measured on 100 log-normal simulations. The uncertainties on the two other covariance estimates are significantly smaller; in the mean of 100 jackknife covariance it is $\sqrt{N}$ times smaller, where $N = 100$ in our case. On the other hand, the uncertainty on each element of the true covariance from 1200 log-normal simulations is calculated using $(\sigma C_i, j)^2 = (C_{ii}C_{jj} + C_{ij}Cij)/(N-1)$, where $N = 1200$ in our case. The lower left panel

[3] `https://github.com/esheldon/kmeans_radec`

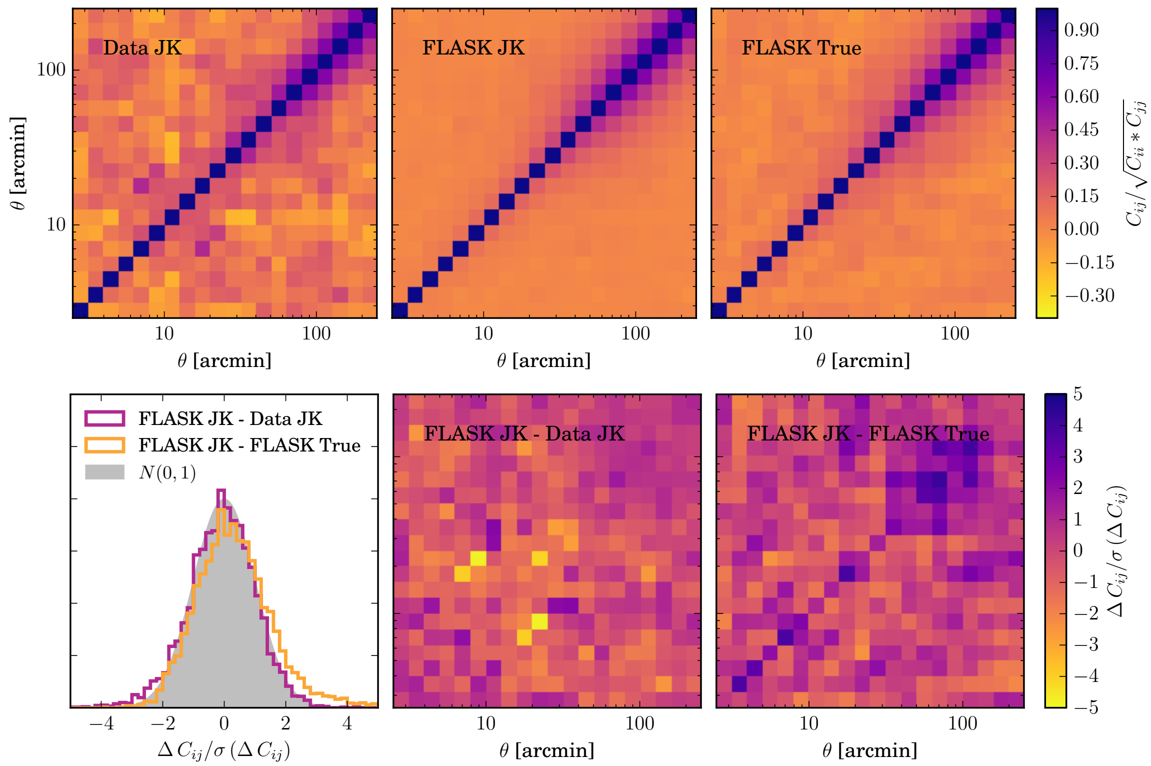

Figure 16: Correlation matrices obtained from the jackknife method on the data (top-left panel), from the mean of jackknife covariances using 100 FLASK realizations (top-middle panel) and from the 1200 log-normal simulations FLASK (top-right panel), for an example redshift bin ($0.3 < z_l < 0.45$ and $0.63 < z_s < 0.90$). In the bottom-middle and bottom-right panels, we show the differences between the covariance matrices shown in the upper panels normalized by the uncertainty on the differences, for the same example redshift bin. On the bottom-left panel, we display the normalized histograms of these differences (20×20 for each covariance, corresponding to 20 angular bins) for all the 5×4 lens-source redshift bin combinations, compared to a Gaussian distribution centered at zero with a width of one.

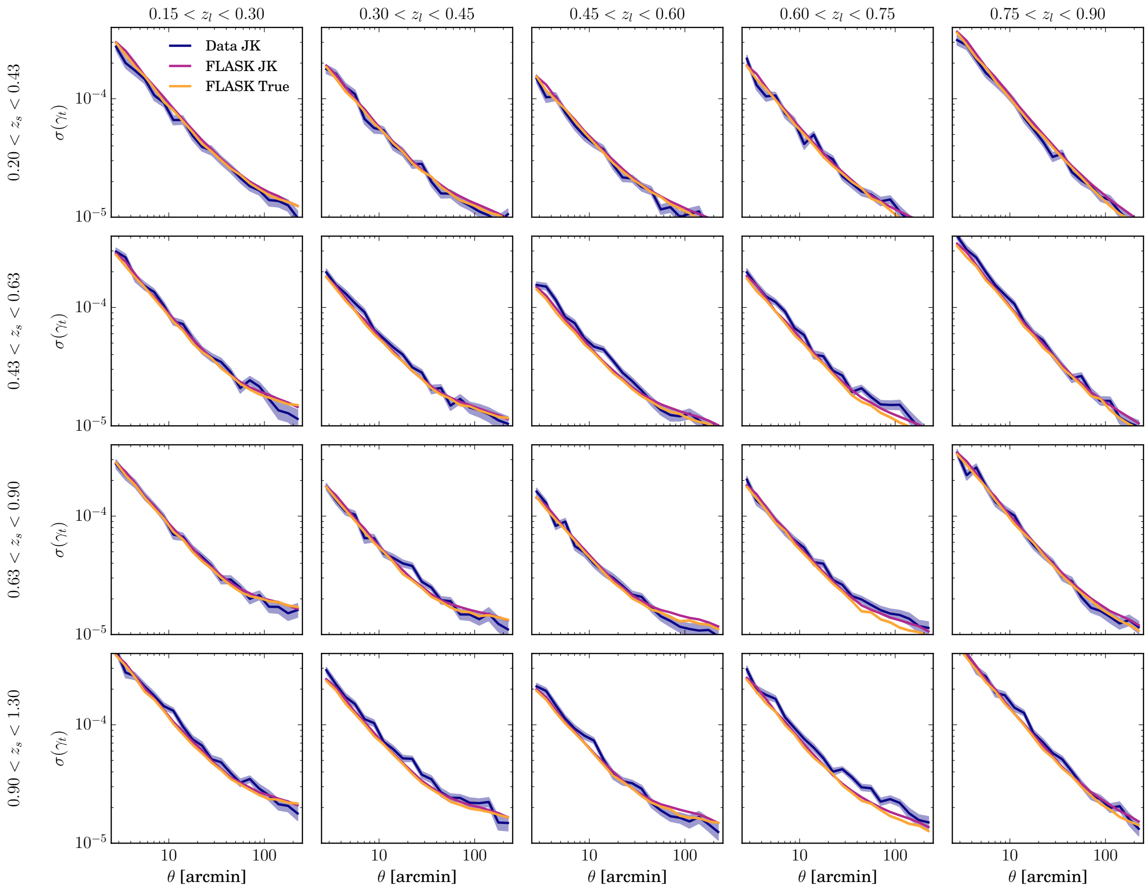

Figure 17: Comparison of the diagonal elements of the covariance obtained from the jackknife method on the data (**Data JK**), from the mean of jackknife covariances using 100 FLASK realizations (**FLASK JK**) and from the 1200 log-normal simulations FLASK (**FLASK True**), for all the lens-source combinations.

shows an overall good agreement between the covariance estimates, even though the larger tail of the orange histogram with respect to a normal distribution indicates a potential slight overestimation of the covariance obtained with the jackknife method.

In Fig. 17 we compare the diagonal elements of the covariance for the 20 lens-source redshift bin combinations, obtaining good agreement for all cases and scales. As in Fig. 16, the uncertainty on the data jackknife covariance comes from the standard deviation of the jackknife covariances measured on 100 log-normal simulations. The uncertainties on the two other error estimates are also shown on the plot, but are of the same order or smaller than the width of the lines.

Overall, we have validated the implementation of the jackknife method on the data by comparing this covariances to the application of the same method on 100 log-normal simulations and to the true covariance obtained from 1200 log-normal simulations, and finding good agreement among them, both for the diagonal and off-diagonal elements.

3.5. Conclusions

Galaxy-galaxy lensing is one of the key ingredients in DES cosmology analysis. This cross-correlation is expected to have lower systematic uncertainties than the shear auto-correlation as additive errors in the shear do not contribute at lowest order. However, a number of sources of systematic uncertainty must still be tested for and quantified.

In this work, we focus on ways to validate galaxy-galaxy lensing measurements made with DES data. To that end, we have performed a number of null tests on the DES SV shear catalogs and photometric redshifts. First, we show that the cross-component of the shear is compatible with zero, which should be the case if the shear is only produced by gravitational lensing. Second, we characterize the PSF leakage by measuring tangential shear signal using interpolated PSF at source positions. Next, we show that the tangential shear signal measured by stacking on random points is consistent with null hypothesis up to a certain scale, which validates the usage of this correction to remove additive systematics near the edge of the survey. Finally, we test how bad the scatter in photometric redshift can affect the galaxy-galaxy lensing measurements by measuring tangential shear of foreground source galaxies around background lens galaxies. We show that the DES SV data passed all our tests.

In addition to the systematics testing, we estimate the covariance matrices for the DES Y1 galaxy-galaxy lensing measurement using the jackknife approach. We validate the estimation using a suite of log-normal mock surveys. We compare the jackknife covariance in the data, the mean of 100 jackknife covariances measured on the log-normal simulations and the true covariance from 1200 log-normal simulations. We find good agreement among them, both for the diagonal and off-diagonal elements. In Section 3.2.3, we show that the random point subtraction can remove a term in the covariance which is significant on scales larger than 20 arcmin.

The detailed tests of measurement systematics and validation of covariance estimation are not just a crucial foundation for other work relying on tangential shear measurements with DES data, but also serve as a useful pipeline for validating future galaxy-galaxy lensing measurements.

CHAPTER 4 : Void Lensing

4.1. Introduction

Cosmic voids are the most underdense regions that constitute the dominant volume fraction of the Universe. Unlike galaxies clusters - which are strongly affected by non-linear gravitational effects and galaxy formation physics, cosmic voids are alternative probes for constraining cosmological parameters ([61], [106], [42]). Meanwhile, the intrinsic underdense environments of cosmic voids make them ideal testbeds for modified gravity theories. For example, [11] showed that chameleon models predict the fifth force is repulsive and stronger inside voids, and the abundance of large voids in modified gravity can be much greater than in ΛCDM. [4] suggested that lensing by voids is a promising tool to test modified gravity theories.

However, 'generic low-density regions in the Universe' is far from a precise definition of cosmic voids. For example, there is no commonly accepted way to determine the boundary of such regions. Thus, a considerable number of void finding algorithms, using different void definition with different tracers, exist in the literature. For example, [81] introduced a method to find voids by identifying spherical volumes where the overall density contrast satisfies a particular threshold. Another series of popular methods involve Voronoi tessellation combining with watershed transform ([85], [77], [107]). And most recently, void finders which identify circular underdensities in 2D projected galaxy map are widely used in the lensing studies of voids ([13], [95]). There are literatures compare properties of voids in different void finders: [18] compared a total of 13 void finders identifying voids from Millennium simulation, while [9] compared 5 void finders focusing on their potential power to test a particular class of modified gravity theory - chameleon $f(R)$ gravity.

Most of the above void finders were applied to simulations where the precise 3D positions were available, or galaxy survey data with spectroscopic redshifts (spec-z). However, spectroscopic surveys like 2dF ([20]) or BOSS ([24]) are expensive in terms of time. The resulting galaxy catalogs are usually smaller than the product of photometric surveys and also may suffer from selection effects, incompleteness and limited depth. Conversely, photometric surveys like KiDS ([25]) or DES([105]), which are more efficient, bias free, more complete and deeper, can only provide photometric redshifts (photo-z) that are less precise. Thus, in order to use photo-z galaxies as tracers, the dispersion along the line-of-sight must be dealt with very carefully. The void finder in [95] circumvented this issue by splitting galaxies into tomographic photometric redshift bins with width larger than the photo-z scatter. In this work, we study how photo-z scatter affects 3D watershed type of void finder in both void-galaxy two-point correlation and lensing measurements.

Recent work by [86] showed that in hydrodynamical simulation the void-tracer cross-correlation can be described by a linear bias relation: the tracer-density contrast around voids can be related to the void matter-density profile by a multiplicative constant that coincides with the linear tracer bias from theoretical calculation. Thanks to the state of art Dark Energy Survey Year 1 (DES Y1) shear catalog ([49], [98]), we get the lensing signal by both 2D and 3D (VIDE) voids with heretofore highest significance. This enable us to test the linearity of tracer bias around voids by comparing the lensing and galaxy-density profiles.

In Section 2 we describe the data and simulation used in this work. In Section 3 we briefly introduced both 2D and 3D void finding algorithms. Section 4 explains our measurement methods for both galaxy-density and lensing profiles. Section 5 presents our measured signal, comments on how photo-z scatter affects the 3D void finder. In Section 6, we make the comparison of profiles in order to test the linearity of tracer bias. Finally, we discuss our results in Section 7.

4.2. Data and Simulations

The Dark Energy Survey is a photometric survey that will cover 5000 sq. deg. of the southern sky to a depth of $r > 24$, imaging about 300 million galaxies in 5 broadband filters (grizY) up to redshift $z = 1.4$. In this work, we use data from a large contiguous region of 1321 sq. deg. of DES Year 1 observations, reaches a limiting magnitude of ≈ 23 in the r-band (with a mean of 3 exposures out of the planned 10 for the full survey).

4.2.1. Void Tracer Galaxies: RedMaGiC

The tracer galaxies used to identify voids in this work is a subset of the DES Y1 Gold Catalog selected by RedMaGiC ([90]), an algorithm used to select a sample of luminous red galaxies (LRGs) with excellent photo-z performance (with a median bias ($z_{\mathrm{spec}} - z_{\mathrm{photo}} \approx 0.5\%$), and a scatter of $\sigma_z/(1+z) = 0.0166$). The RedMaGiC algorithm select galaxies above some luminosity threshold based on how well they fit a red sequence template which calibrated using redMaPPer ([91]) and a subset of galaxies with spectroscopic redshifts. The cutoff in the goodness of the fit to the template is imposed as a function of redshift and adjusted such that a constant comoving density of galaxies is maintained.

4.2.2. Lensing Source Catalog: METACALIBRATION

METACALIBRATION ([49], [98]) is a recently developed method to accurately measure weak lensing shear without using any prior information about galaxy properties or calibration from simulations. The method involves distorting the image with a small known shear, and calculate the response of a shear estimator to that applied shear. It can be applied to any shear estimation pipeline. For the catalog used in this work, it has been applied to the NGMIX shear pipeline ([97]).

4.2.3. Simulation: MICE

Aside from the data catalogs presented above, the RedMaGiC algorithm has also been run on a mock catalog from MICE ([21], [35]) simulation. The *MICE Grand Challenge* (MICE-GC, [36]) is an all-sky lightcone N-body simulation using 4096^3 dark-matter particles in a $(3Gpc/h)^3$ comoving volume, and assuming a flat concordance ΛCDM cosmology with $\Omega_m = 0.25, \Omega_\Lambda = 0.75, \Omega_b = 0.044, n_s = 0.95, \sigma_8 = 0.8$ and $h = 0.7$. The galaxy mock catalog includes extensive galaxy and lensing properties for ~ 200 million galaxies over 5000 sq.deg. up to a redshift $z = 1.4$.

4.3. Void Finders

In the following, we introduce two void finding algorithms that will be applied to the same set of data used in this work. One is to identify voids in 2D redshift slices, the other works in 3D.

4.3.1. 2D Voids

We are using the same 2D void finding algorithm as in [95], which is similar to that of [13]. The void finder works by searching for underdensities in 2D galaxy fields, which constructed from projecting galaxies onto redshift slices. The motivation for using thick(100 Mpc/h) redshift slices is to minimize the effects of photo-z scatter.

Basically, the algorithm can be described by the following steps:

1. It projects tracer galaxies in a redshift slice of some thickness onto a HEALpix ([40]) map.

2. For each slice, it computes the mean tracer density in the map, and convert the tracer density map to a density contrast map. Then it smooths the density contrast map with a Gaussian filter.

3. For a particular slice, it starts with the most underdense pixel in the smoothed map by considering the pixel as the first void center. Then it grows a circular shell around that pixel until the density in the shell reaches the mean density.

4. All pixels within the circular shell are removed from the list of potential void centers. Repeat the previous step until all pixels which are below some density threshold have been removed (assigned to a void).

5. Pruning the resulting void catalog by joining voids in neighboring slices that are

angularly close.

4.3.2. 3D VIDE Voids

To identify voids in 3D, we use the publicly available void finder VIDE([107]). VIDE is a wrapper for ZOBOV ([77]), and it provides a functionality for identifying voids from real observation while ZOBOV was originally intended for void-finding in simulation.

Basically, the algorithm can be described by the following steps:

1. Assign each tracer a cell using a Voronoi tessellation technique. It guarantees that a cell assigned to a tracer is the region which is closer to that tracer than to any other tracer. Thus the inverse of the volume of a cell is an estimator of density in that sell.

2. Identify the density minima in the density field established in step 1. A density minima is a Voronoi cell with a density lower than all its adjacent cells.

3. Starting from a density minima, join together adjacent cells with increasing density until no surrounding higher density cell can be found. The resulting groups are called *basins*.

4. A watershed transform is performed to join together basins in order to form larger voids. The ridge between basins needs to be lower than 20% of the mean density of the Universe.

5. The void-center is defined as the volume-weighted barycenter, and the effective radius of the void is computed from the total volume and spherical shape assumption.

4.3.3. Final void catalogs

Applying the void finding algorithms on the DES Y1 redMaGiC catalog, we find a total of 533 2D voids and 7387 3D VIDE voids. Figure. 18 shows the void radius distribution for both void catalogs. We divide each void catalog into 3 subsamples based on the void radius: for 2D voids we define three bins $R_v = 20 - 40$ Mpc/h, $R_v = 40 - 60$ Mpc/h, and

$R_v = 60 - 120$ Mpc/h, each bin of increasing R_v has 291, 121, and 85 voids. For 3D VIDE voids we also define three bins $R_v = 10 - 20$ Mpc/h, $R_v = 20 - 30$ Mpc/h, and $R_v = 30 - 60$ Mpc/h, each bin of increasing R_v has 3555, 2902, and 918 voids.

4.4. Methodology

With the void catalogs constructed from the algorithms described earlier, we are ready to measure the tangential shear as well as the galaxy density contrast around these voids. By measuring the lensing signal, we not only can validate the void finding algorithms but also be able to compare these algorithms more fundamentally: probing the underlying mass profile of the detected voids.

In this section, we present our procedure of lensing measurement, covariance estimation, and the observables for galaxy density contrast.

4.4.1. Lensing measurements

The excess surface mass density $\Delta\Sigma$ is defined as

$$\Delta\Sigma(R/R_v) = \overline{\Sigma(R/R_v)} - \Sigma(R/R_v) = \Sigma_{\rm crit}\gamma_t(R/R_v) \tag{4.1}$$

where $\Sigma_{\rm crit}$ is the critical surface mass density describing the lensing strength

$$\Sigma_{\rm crit} = \frac{c^2}{4\pi G}\frac{D_A(z_S)(1+z_L)^{-2}}{D_A(z_L)D_A(Z_L, Z_S)} \tag{4.2}$$

where z_L and z_S are the lens and source redshifts, respectively. And we have $\Sigma^{-1}_{\rm crit}(z_L, z_S) = 0$ for $z_S < z_L$. All the distances are in comoving units and a flat ΛCDM with $\Omega_m = 0.3$ is assumed. Following the method in [64], our stacked lensing observable is given by

$$\Delta\Sigma_k(R/R_v; z_L) = \frac{\sum_j [w_j \gamma_{k,j}(R/R_v)\Sigma_{\rm crit,j}(z_L, z_S)]}{\sum_j w_j} \tag{4.3}$$

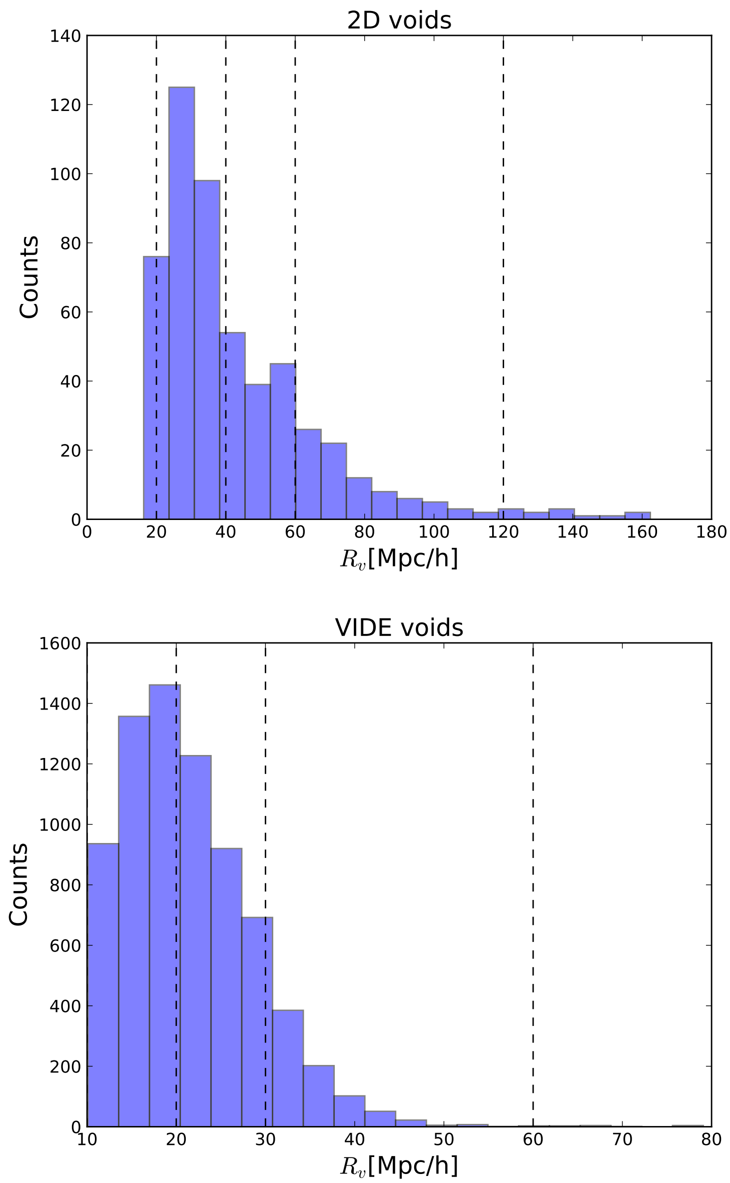

Figure 18: Distribution of comoving void radius of the DES Y1 void catalogs. The upper panel shows the 2D voids identified using redshift slices of thickness 100 Mpc/h, and the lower panel shows the 3D VIDE voids. The vertical dashed lines corresponding to the cuts we used in this work to divide our void samples.

where k denotes the two possible components of the shear: the tangential and cross components, the summation $\sum_j$ runs over all void-source pairs in the radial bin R/R_v, and the optimal weight for the j-th galaxy is given by [100]

$$w_j = \frac{[\Sigma^{-1}_{\mathrm{crit,j}}(z_L, z_S)]^2}{\sigma^2_{\mathrm{shape}} + \sigma^2_{m,j}} \tag{4.4}$$

Here σ_{shape} is the intrinsic shape noise for each source galaxy, and $\sigma_{m,j}$ is the shape measurement error.

Note that for the DES Y1 data, we are also using the MetaCALIBRATION shear catalog ([49], [98]), so we are applying the response corrections to the shear statistics as described in section 3.2.1.

4.4.2. Covariance estimation

Due to the small number of voids in the catalogs (especially in the 2D void catalog), we perform a void-by-void jackknife in the same way as in [95]: we perform the measurement multiple times with each void omitted in turn to make N (the number of voids in our sample) jackknife realizations. The covariance of the measurement is thus given by [78]:

$$C[\Delta\Sigma_i, \Delta\Sigma_j] = \frac{N-1}{N} \times \sum_{k=1}^{N} [(\Delta\Sigma_i)^k - \overline{\Delta\Sigma_i}][(\Delta\Sigma_j)^k - \overline{\Delta\Sigma_j}] \tag{4.5}$$

where $(\Delta\Sigma_i)^k$ denotes the measured value from the k-th JK realization and the i-th radial bin, and the mean value is

$$\overline{\Delta\Sigma_i} = \frac{1}{N} \sum_{k=1} N(\Delta\Sigma_i)^k \tag{4.6}$$

4.4.3. Galaxy density contrast

People have investigated the linearity of tracer bias around voids in simulations ([86]). They found the tracer-density profile of voids can be related to their matter-density profile by a single number which coincides with the linear tracer bias extracted from the large-scale auto-correlation function and from theoretical calculation.

Since our void lensing results are with pretty high signal-to-noise ratio, it would be interesting to test this linearity (or constrain the scale of the linear regime) of tracer bias in real data.

In [86], they measure the 3D overdensity of tracers around void centers by

$$\xi_{\rm 3D}(r) = \frac{n_{vt}(r)}{\langle n_t \rangle} - 1 \tag{4.7}$$

In real observations, especially for photometric surveys, we don't have precise information along the line-of-sight direction. One way to bypass this is: instead of measuring the 3D correlation function; we can project all tracers along the line of sight and measure the 2D correlation function. And equation (4.7) thus can be written as:

$$\xi_{\rm 2D}(r_p) = \frac{\Sigma_{vt}(r_p)}{\langle \Sigma_t \rangle} - 1 \tag{4.8}$$

where Σ_{vt} is the measured 2D number density of tracers around voids and $\langle \Sigma_t \rangle$ is the mean number density of tracers.

Cosmic voids are extended structures typically with radius R_v greater than 10 Mpc/h, and our measurements go as far as a few R_v. According to [86], as the void radius surpasses a critical value, the estimated bias $b_{\rm slope}$ stabilizes asymptotically to a constant value. So we are potentially more interested in larger voids. Thus we need to be very careful dealing with voids near the survey edge since no galaxies are observed beyond the boundary.

For uniformly-distributed 2D points, the correlation function is zero. Thus we can use a random catalog generated by applying the same survey mask as the tracer catalog to 'normalize' the 2D number density of tracers. Meanwhile, we make sure the mean density is equal to the number density of random points around those voids. That is, we apply a

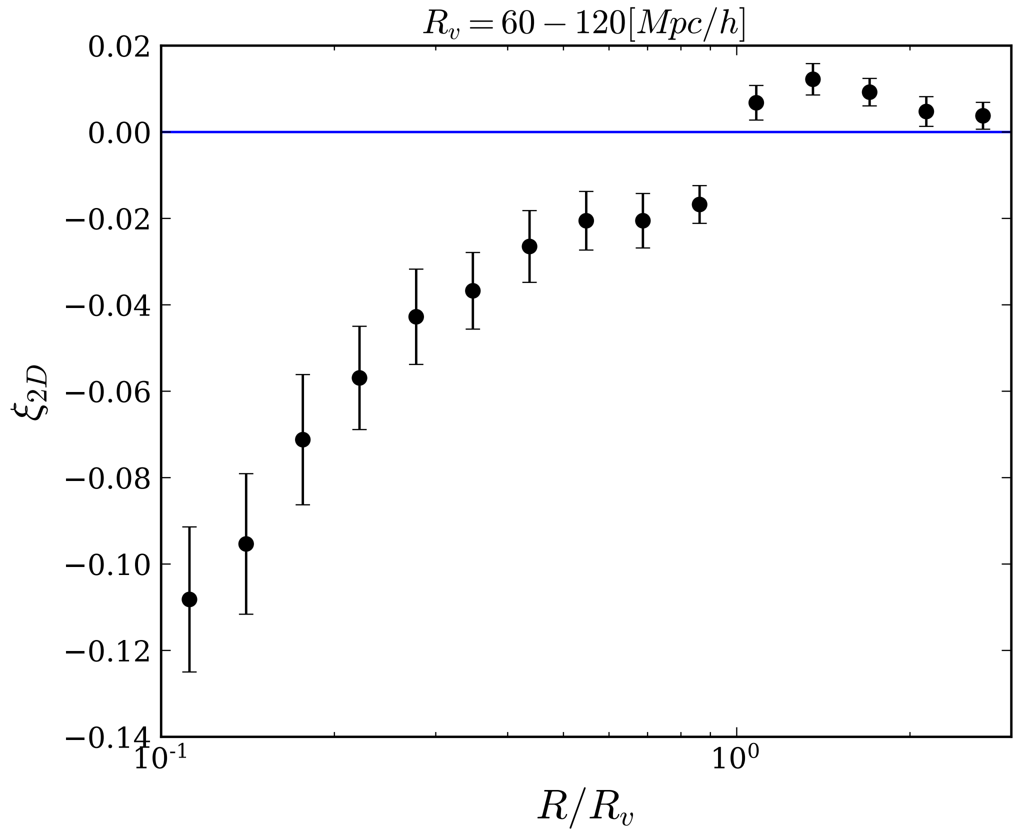

Figure 19: Measured '2D' overdensity of RedMaGiC galaxies around 2D voids in DES Y1 data with $R_v = 60 - 120$ Mpc/h. The error bars are 1σ jackknife errors calculated by omitting one single void each time.

Davis & Peebles estimator ([23]) and Equation 4.8 becomes:

$$\xi_{\rm 2D}(r_p) = \frac{N_r}{N_t}\frac{\Sigma_{vt}(r_p)}{\Sigma_{vr}(r_p)} - 1 \tag{4.9}$$

where N_t is the size of tracer sample, N_r is the size of random sample, and $\Sigma_{vr}(r_p)$ is the projected 2D number density of random points around voids.

For 2D voids in DES Y1 data with $R_v = 60 - 120$ Mpc/h (85 voids are of this size), the result is shown in Fig. 19. And we also perform the 2D measurement for 3D watershed voids (918 voids are of this size). The result for $R_v = 30 - 60$ Mpc/h sample is shown in Figure 20

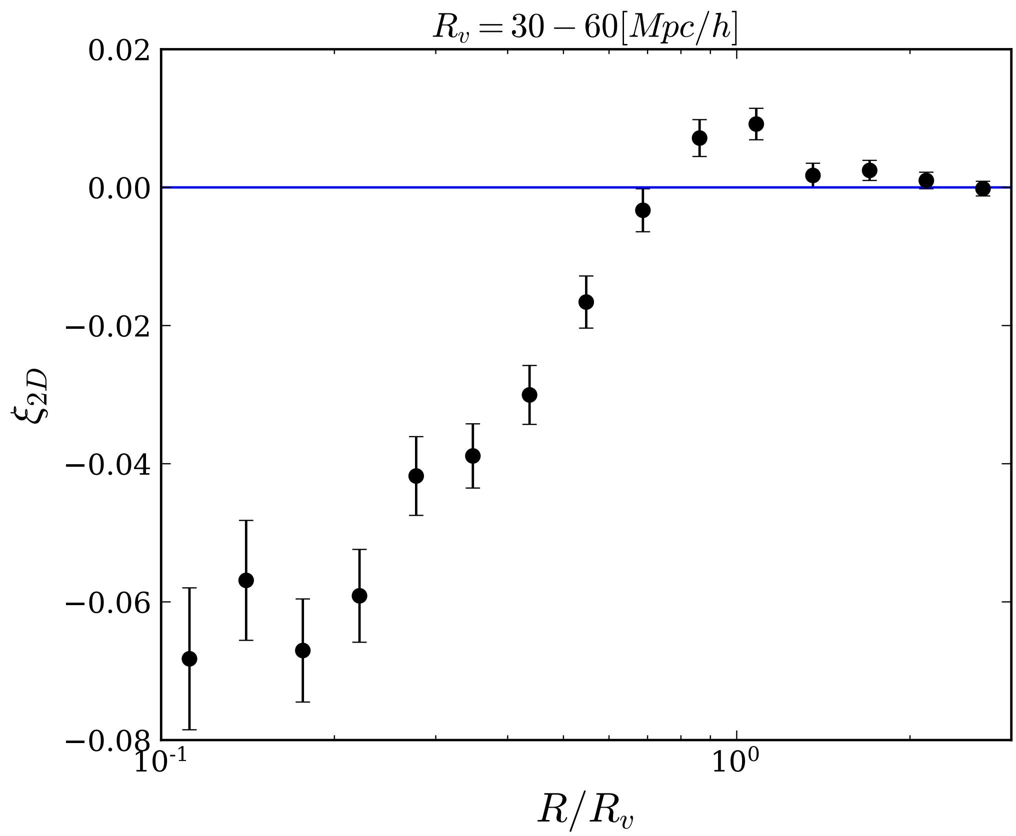

Figure 20: Measured '2D' overdensity of RedMaGiC galaxies around VIDE voids on DES Y1 data with $R_v = 30 - 60$ Mpc/h. The error bars are 1σ jackknife errors calculated by omitting one single void each time.

Another widely used estimator for measuring the two-point correlation function and can incorporate the edge-correction is the Landy & Szalay estimator ([59]), which are shown to have the best noise properties, writing in the void case:

$$\xi_{\mathrm{2D}}(r_p) = \frac{\frac{N_{v_r}N_r}{N_v N_t}\Sigma_{vt}(r_p) - 2\frac{N_{v_r}}{N_v}\Sigma_{vr}(r_p) + \Sigma_{v_r r}(r_p)}{\Sigma_{v_r r}(r_p)} \tag{4.10}$$

where $\Sigma_{v_r r}(r_p)$ is the projected 2D number density of random-void and random-point pairs. The randomized void catalog can be produced such that it mimics the R_v and redshift distribution, and follows the same survey mask (see Appendices C in [95] for further information).

We implement the Landy & Szalay estimator for the 3D VIDE voids in MICE2 simulation. Figure 21 is a comparison of two estimators. It turns out they agree quite nicely. Thus we stick to Equation 4.9 for all our later galaxy profile measurements because it is computationally easier and the randomized void catalog is not needed.

4.5. Results

In this section, we present our measured tangential shear signal of VIDE voids in both MICE simulation and DES Y1 data. We show the lensing results of 2D voids but just in DES Y1 data. We comment on how photo-z scattering affects the void identification using the results from simulation.

4.5.1. Test effects of photo-z scattering in simulation

To validate our procedure, and also test how the uncertainty in the redshift estimation affects the void finding algorithms, we first perform the void lensing measurements on MICE2 simulation. Figure 22 shows the lensing profile of a subset of 3D VIDE voids ($R_v = 30 - 60$ Mpc/h) which use MICE2 RedMaGiC high density sample as tracers. The cross component is strictly consistent with zero at all scale as we expected.

In the simulation, we know the precise 3D information. So we can also run the void finding

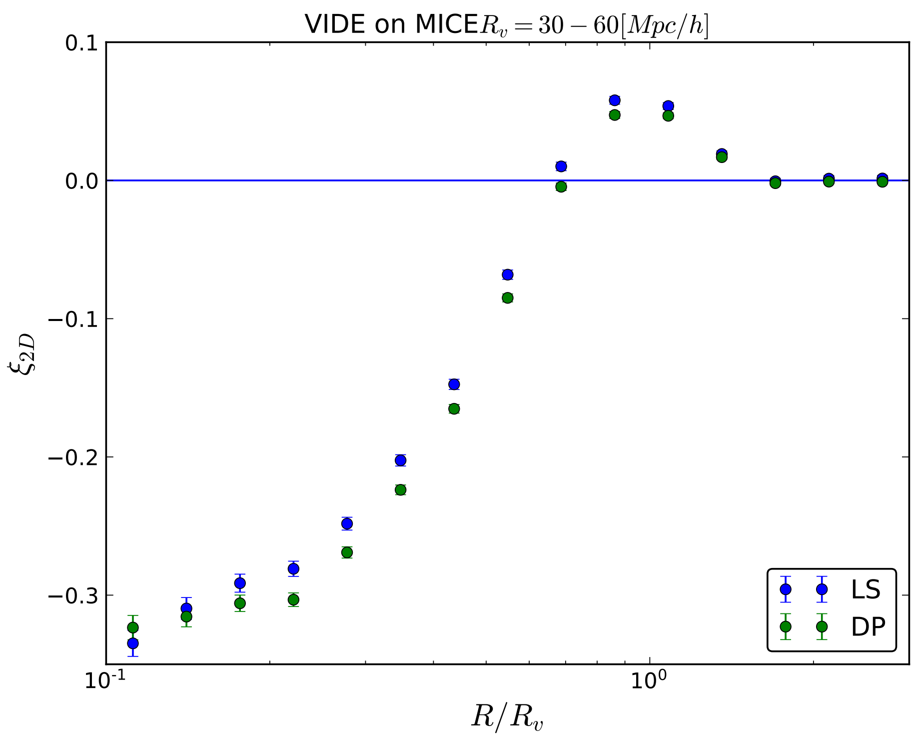

Figure 21: Compare the measured '2D' overdensity of RedMaGiC galaxies around VIDE voids on MICE2 simulation using Davis & Peebles and Landy & Szalay estimators.

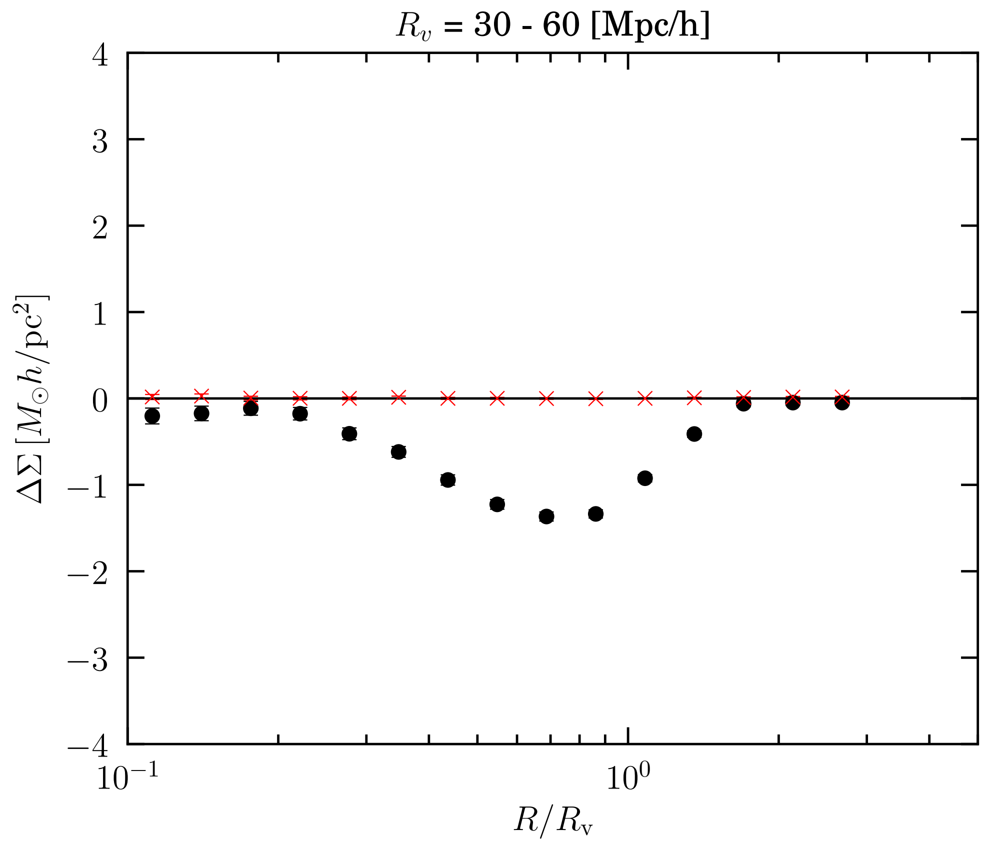

Figure 22: Lensing profile for VIDE voids traced by MICE2 RedMaGiC high density sample. This subsample of voids is with R_v ranging from $30 - 60$ Mpc/h

algorithms based on the true redshifts of the tracer galaxies. We call the resulting catalog the 'spectroscopic' void sample. Then we repeat the lensing measurement on it. Figure 23 shows a comparison of lensing profiles of voids identified by tracers with photometric and true redshifts. It can be seen the two tangential profiles are quite different: the signal for photometric voids is actually much stronger! One possible explanation is: in the photometric void sample, the uncertainty of positions of tracers is only in the line-of-sight(LOS) direction. This 'smearing' of tracers makes the 3D watershed void finder more likely to pick out voids that are elongated along the LOS, which are having stronger lensing signal. In order to testify our guess, we compare the galaxy density contrast profiles for these two void samples, which is shown in Fig 24. Indeed we can see the photo-z voids are emptier in terms of tracers within the cylinder along the LOS, which can cause more negative lensing signal. Thus we come down to a interesting conclusion: for a void finder that works in 3D, photo-z scattering can potentially bias the identified void sample, which results in a boosting of lensing signal.

4.5.2. Tangential shear profiles in data

Figure 25 shows the stacked lensing profile around 2D voids in DES Y1 data. The significant negative tangential component indicates these voids are indeed underdense regions in the universe. It is also evident that two dips exist, which is a sign that this sample is mixing up different void types.

We further divide our 2D void sample into three void radius bins. Their lensing profiles are shown in Figure 26. The negative tangential components are significant in all 3 R_v bins. The 2-dips feature is most evident in the largest void bin. This fact may imply a scenario that merging is an on-going process in larger voids.

Figure 27 shows the lensing profiles for 3D VIDE voids in DES Y1 data. Since the total number of identified 3D voids is much greater than 2D voids, the signal-to-noise ratio for VIDE samples are even higher.

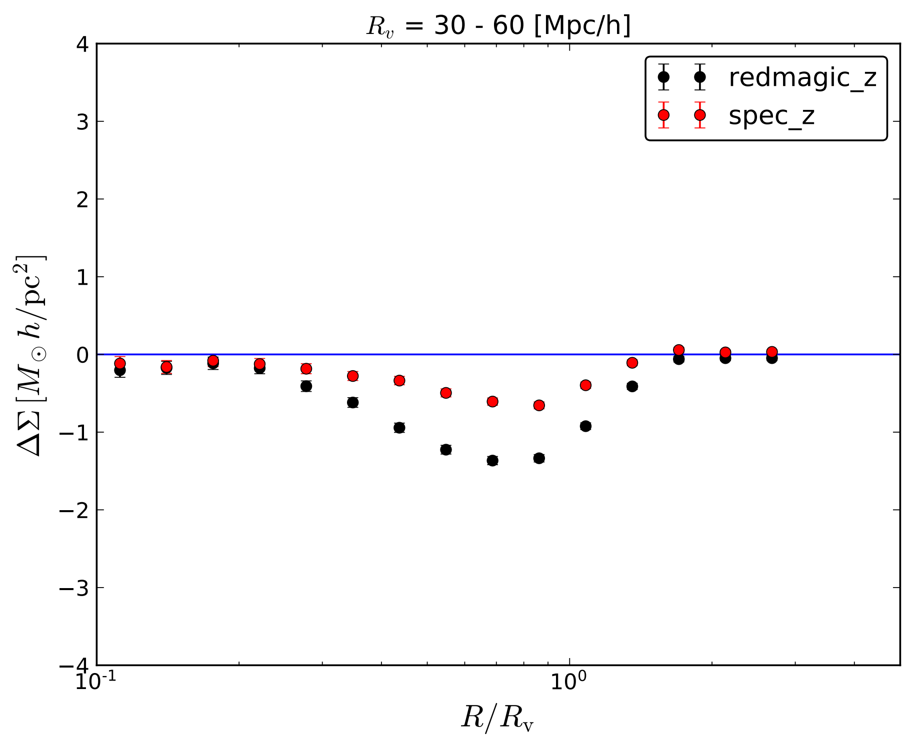

Figure 23: Test how the scattering of tracer redshift affects the lensing profiles of VIDE voids on MICE2 simulation. The black points are the tangential signal for photometric voids and the red points are for the spectroscopy voids.

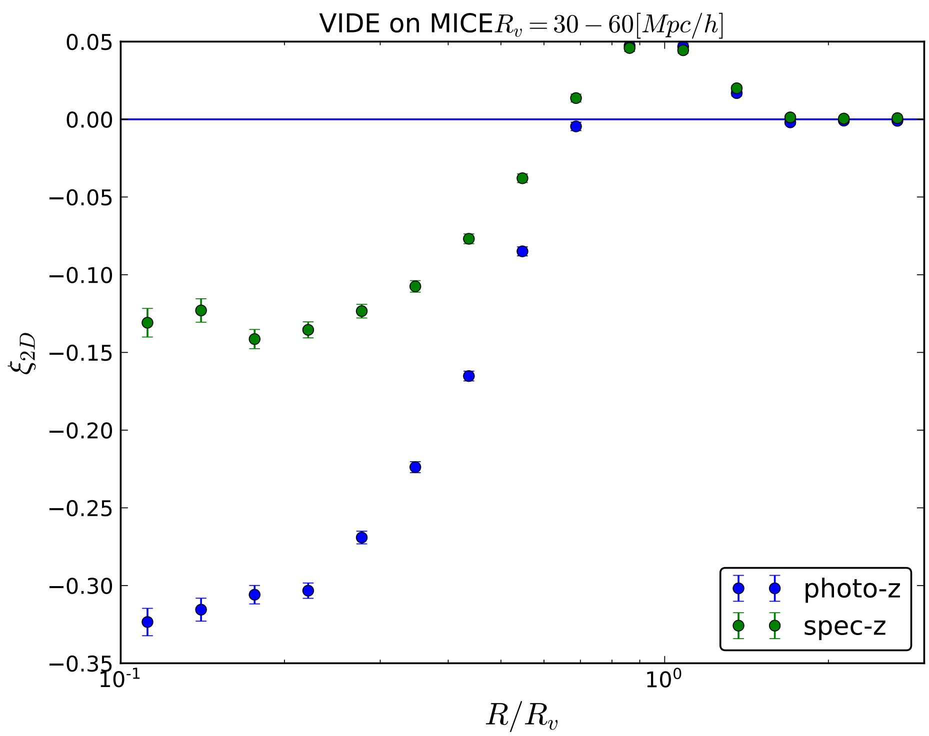

Figure 24: Test how the tracer redshifts affect the galaxy density contrast profiles of VIDE voids on MICE2 simulation. The blue points are the signal for photometric voids and the green points are for the spectroscopy voids.

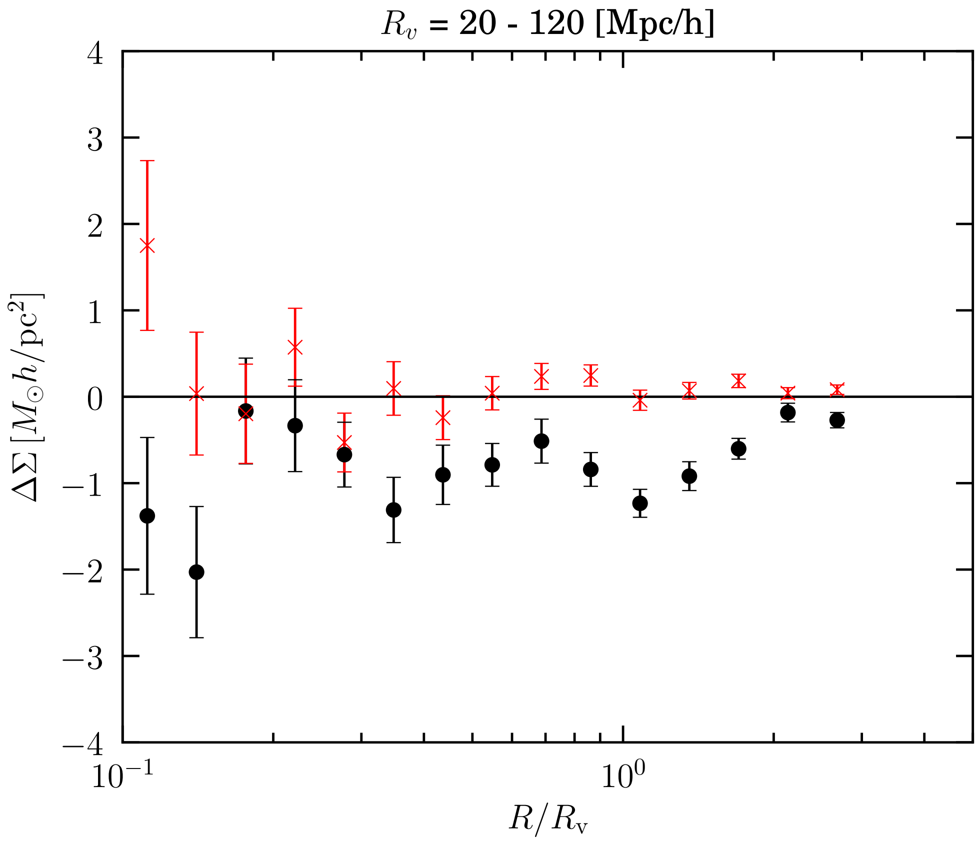

Figure 25: Stacked lensing profile of 2D voids in DES Y1 data. The black points are the tangential components and the red crosses are the cross components. The errorbars represent 1σ jackknife errors. The cross components are consistent with null hypothesis. The tangential components are significantly negative imply the detected 2D voids are indeed correspond to the underdense regions in the matter field.

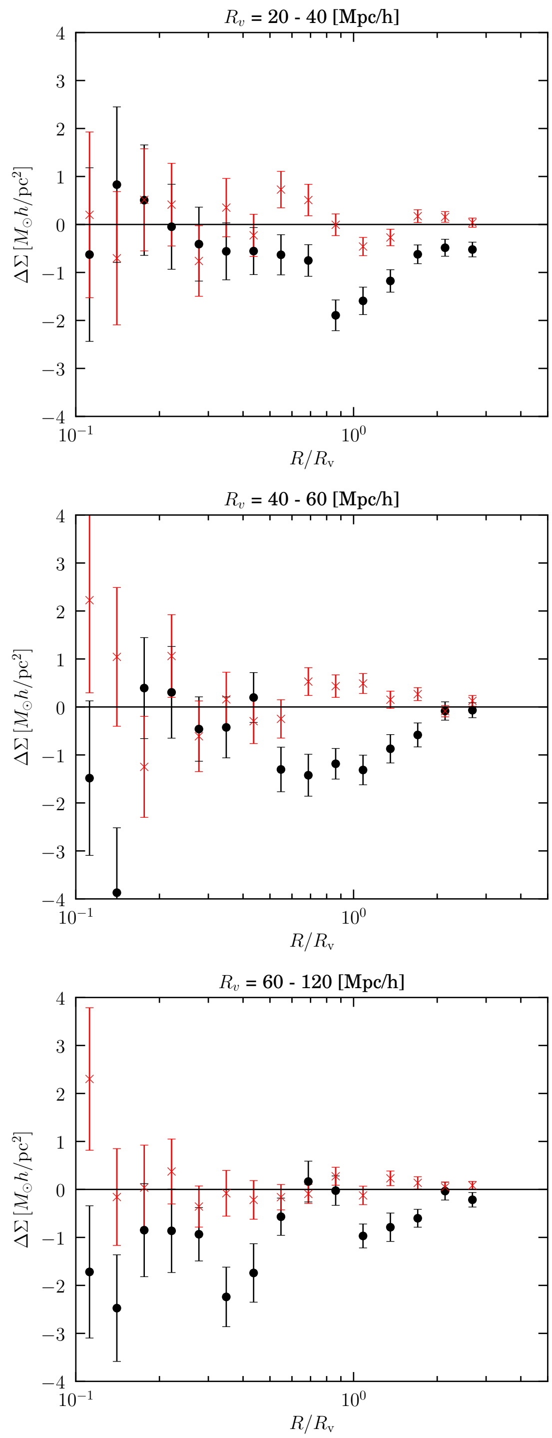

Figure 26: Lensing profiles for 2D voids in DES Y1 data, binning by void radius R_v.

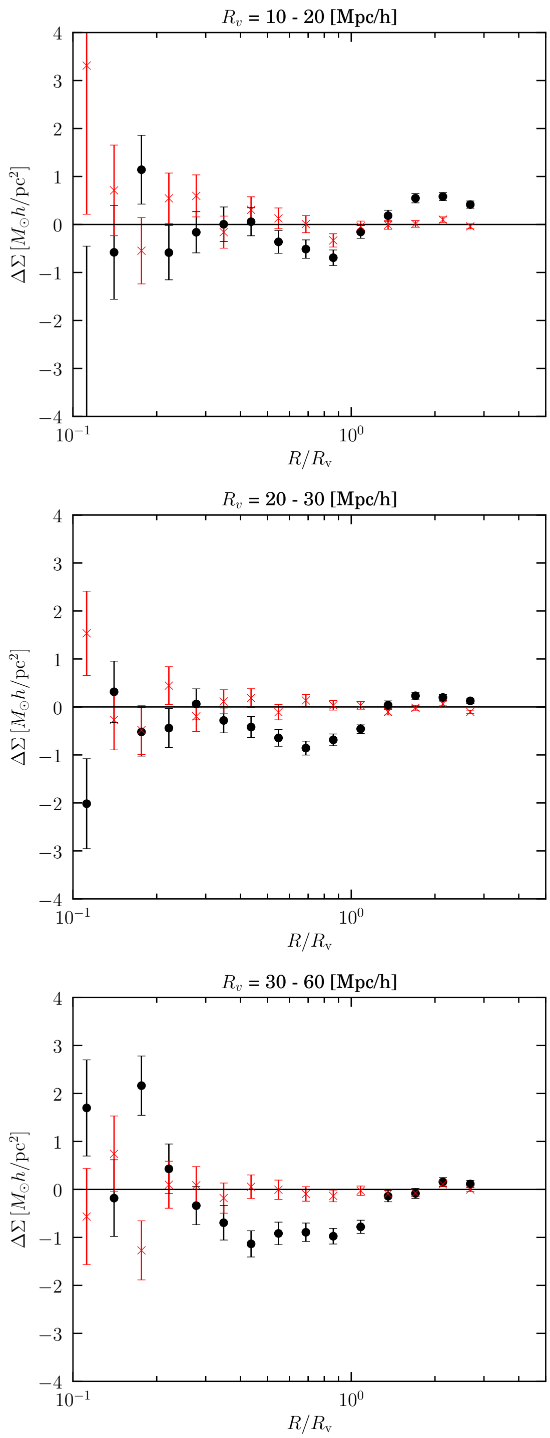

Figure 27: Lensing profiles for VIDE voids in DES Y1 data, binning by void radius R_v.

4.6. Test of Linearity

[86] measured both stacked overdensity profiles of tracer galaxies and matter particles around voids in a hydrodynamical simulation. They found that the tracer profile can be linked to the matter profile of voids with a simple linear relation, and the slope coincides with the linear tracer bias estimated from theoretical calculation. In observation, we can only infer the overall mass distribution from stacked lensing signal. In what follows, we present our formalism and show a qualitative test of this linear relation with voids found in DES Y1 data.

4.6.1. Observables and theory validation

From the Equation.12 in [86]:

$$\frac{n_{vt}}{\langle n_t \rangle} - 1 = b_{\mathrm{slope}}(\frac{n_{vm}}{\langle n_m \rangle} - 1) + c_{\mathrm{offset}} \tag{4.11}$$

where n_{vt} is the measured 3D tracer-density profiles around voids, $\langle n_t \rangle$ is the mean 3D tracer density, n_{vm} is the measured 3D matter-density profile around voids, $\langle n_m \rangle$ is the mean 3D matter density of the Universe, and b_{slope} and c_{offset} are the two free parameters to be fitted. They found that the fitted value of c_{offset} is always consistent with zero and for sufficiently large voids b_{slope} = linear bias. To incorporate this equation with our 2D observables, we can first perform an Abel transform on the 3D quantity $\xi_{vt} = \frac{n_{vt}}{\langle n_t \rangle} - 1$:

$$\xi_{\mathrm{2D,vt}}(r_p) = 2\int_{r_p}^{\infty} \xi_{vt}(r) \frac{r}{(r^2 - r_p^2)^{1/2}} dr \tag{4.12}$$

where r_p is the projected distance from the void center, $\xi_{\mathrm{2D,vt}}(r_p)$ is the projected 2D number density profile of the tracer around voids. From Equation 4.11, we know $\xi_{vt}(r) =$

$b_{\rm slope}\xi_{vm}(r)$. We can substitute it into Equation 4.12:

$$\begin{aligned}\xi_{\rm 2D,vt}(r_p) &= 2\int_{r_p}^{\infty} b_{\rm slope}\xi_{vm}(r)\frac{rdr}{(r^2-r_p^2)^{1/2}} \\ &= 2b_{\rm slope}\int_{r_p}^{\infty}\xi_{vm}(r)\frac{rdr}{(r^2-r_p^2)^{1/2}} \\ &= b_{\rm slope}\xi_{\rm 2D,vm}(r_p)\end{aligned} \tag{4.13}$$

where the $b_{\rm slope}$ can be taken out from the integral since it does not depend on r.

In practice, it could be hard to get the 2D mass profile Σ directly from lensing $\Delta\Sigma$ in a model independent way. However we can do this comparison in an opposite way. We convert the galaxy profile to a 'differentiate' galaxy profile and compare it with lensing $\Delta\Sigma$ directly. Since $\Delta\Sigma(R) = \overline{\Sigma(<R)} - \Sigma(R)$, we can define an operator Δ such that $\Delta(\Sigma) = \bar{\Sigma} - \Sigma$. It is easy to show:

$$\begin{aligned}\Delta(b\Sigma) &= \overline{b\Sigma} - b\Sigma = b\Delta(\Sigma) \\ \Delta(\Sigma + c) &= \overline{\Sigma + c} - (\Sigma + c) = \bar{\Sigma} - \Sigma = \Delta(\Sigma)\end{aligned}$$

where b and c are constants. This operator can be applied to Equation 4.13

$$\begin{aligned}\Delta\Sigma_g(r_p) \equiv \Delta(\xi_{\rm 2D,vt}(r_p)) &= b_{\rm slope}\Delta(\xi_{\rm 2D,vm}(r_p)) \\ &= b_{\rm slope}\Delta(\frac{\Sigma(r_p)}{\langle\Sigma\rangle} - 1) \\ &= b_{\rm slope}\frac{\Delta\Sigma(r_p)}{\langle\Sigma\rangle}\end{aligned} \tag{4.14}$$

Thus we show that the linear relation between the 3D overdensity profiles (Equation 4.11) which has been found in the simulation should also hold for the 2D differentiate profiles $\Delta\Sigma$ and $\Delta\Sigma_g$, where the galaxy profile $\Delta\Sigma_g$ is computed by interpolating the measured 2D tracer overdensity profile $\xi_{\rm 2D,vt}(r_p)$ (Equation 4.9) over the projected distance from the void center, and then apply the Δ operator introduced earlier. Our final data vector consists of both lensing profile $\Delta\Sigma$ and galaxy profile $\Delta\Sigma_g$. We can estimate its covariance using a

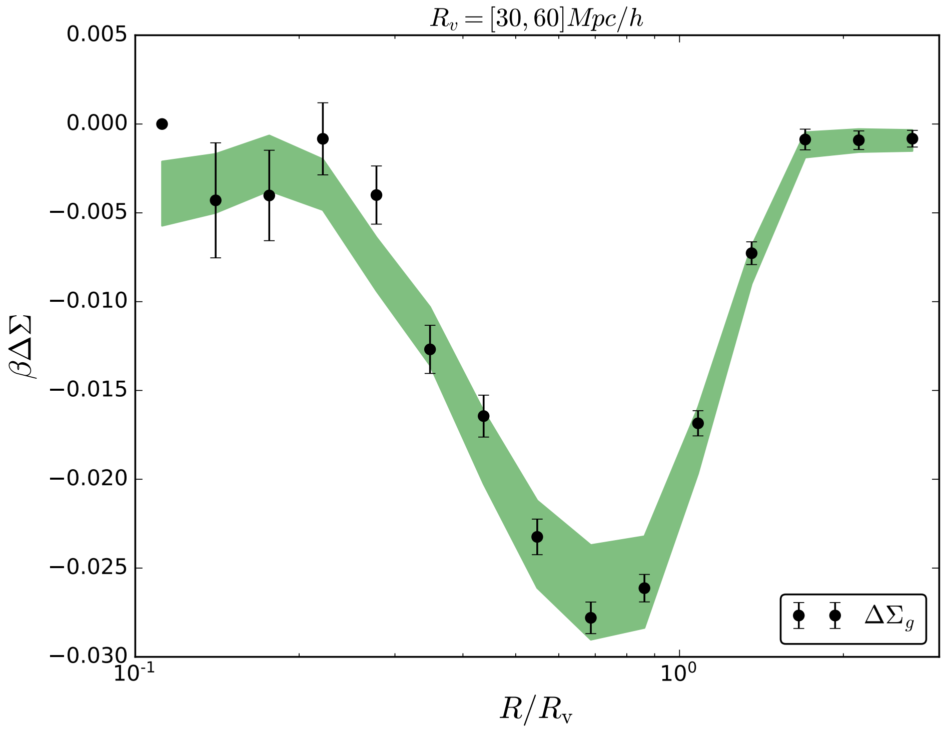

Figure 28: Compare galaxy ($\Delta\Sigma_g$) and lensing ($\Delta\Sigma$) profiles for 3D voids with $R_v = 30 - 60$ Mpc/h identified in the MICE simulation. The ratio fitting was performed by omitting the first 3 data points at small scales. The green band represents the propagated errors. The first data point of $\Delta\Sigma_g$ has been fixed to equal to zero.

void-by-void Jackknife method introduced in Section 4.10.

We then calculate the ratio of the two profiles. Since both of them are noisy quantities, instead of taking the ratio directly and applying a constant fitting, which is potentially biased, we use an MCMC fitting to fit for a constant β and a vector $\boldsymbol{\alpha}$ simultaneously such that:

$$\begin{aligned} \beta * \alpha_i &= \Delta\Sigma_{g,i} \\ \alpha_i &= \Delta\Sigma_i \end{aligned} \tag{4.15}$$

Then the β is simply the ratio $\frac{b_{\rm slope}}{\langle\Sigma\rangle}$ and α_i are just a set of nuisance parameters to be marginalized over.

We first run this pipeline on 3D VIDE voids identified in the simulation. In Figure 28, we show both galaxy profile $\Delta\Sigma_g$ and the fitted β multiplying the lensing profile $\Delta\Sigma$. The ratio fitting was performed by omitting the first 3 data points at small scales. Note that there is no errorbar shown for the first data point of the galaxy profile since it has been fixed to equal to zero. This is because it is the starting point for interpolation, but we don't have any information at scales smaller than that point; thus we assume a flat profile beyond that. It can be seen that both profiles agree with each other quite well at almost all scales, except at the very inner region where the shot noise dominated. In Figure 29, we show how the MCMC fitting is working. The left panel shows the distribution of the ratio β after marginalizing over all other parameters α_i. It can be seen that β has been very tightly constrained. The right panel shows the corresponding random walkers, where β is labeled '0'. The first three data points at small scales were removed from the fitting process to avoid the shot noise dominated region.

Thus we have validated our observables and methodology with 3D VIDE voids in MICE simulation. By just looking at both differentiate profiles, we can check the linearity qualitatively. With the fitted ratio β, we can further infer the b_{slope}, which is shown in [86] to coincide with the tracer bias.

4.6.2. Linearity of voids in DES Y1 data

In Figure 30 we show the results for three void radius R_v bins, $10 < R_v < 20$ Mpc/h, $20 < R_v < 30$ Mpc/h, and $30 < R_v < 60$ Mpc/h, of 3D VIDE voids identified in DES Y1 data. The left panels show the comparison of galaxy profile $\Delta\Sigma_g$ and fitted β times the lensing profile $\Delta\Sigma$. For the smaller two R_v bins, the agreements are quite impressive. At a few data points, the profiles slight deviate from each other for the largest R_v bin. The right panels are the corresponding distributions of fitted β after marginalizing over all nuisance parameters α_i. We repeat this analysis on the 2D voids of radius $20 < R_v < 40$ Mpc/h, $40 < R_v < 60$ Mpc/h, and $60 < R_v < 120$ Mpc/h, found in DES Y1 data. The results are shown in Figure 31. However, the agreements in the 2D voids are not as good as in

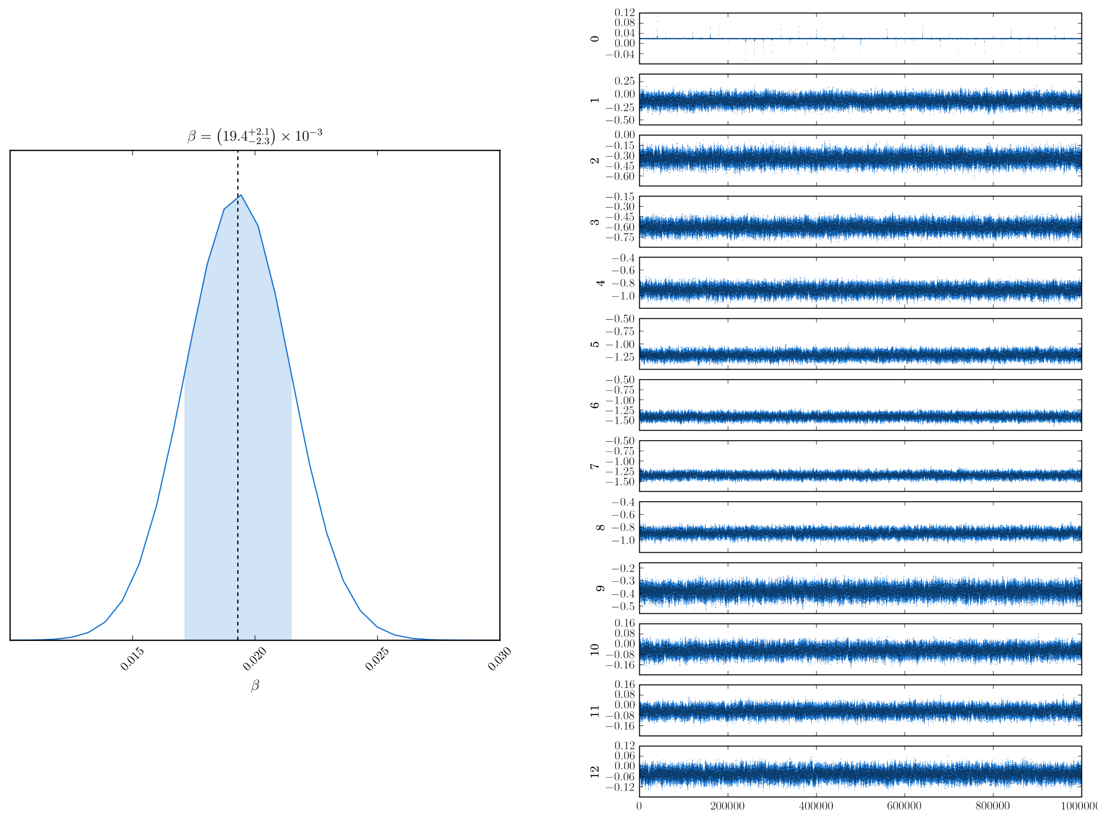

Figure 29: The process of the MCMC fitting. The left panel shows the distribution of the ratio β for 3D VIDE voids with $R_v = 30 - 60$ Mpc/h in the MICE simulation. The β has been very tightly constrained. The right panel shows the walks for all MCMC parameters, where '0' is what β has been labeled. The first three data points at small scales have been omitted during the fitting process.

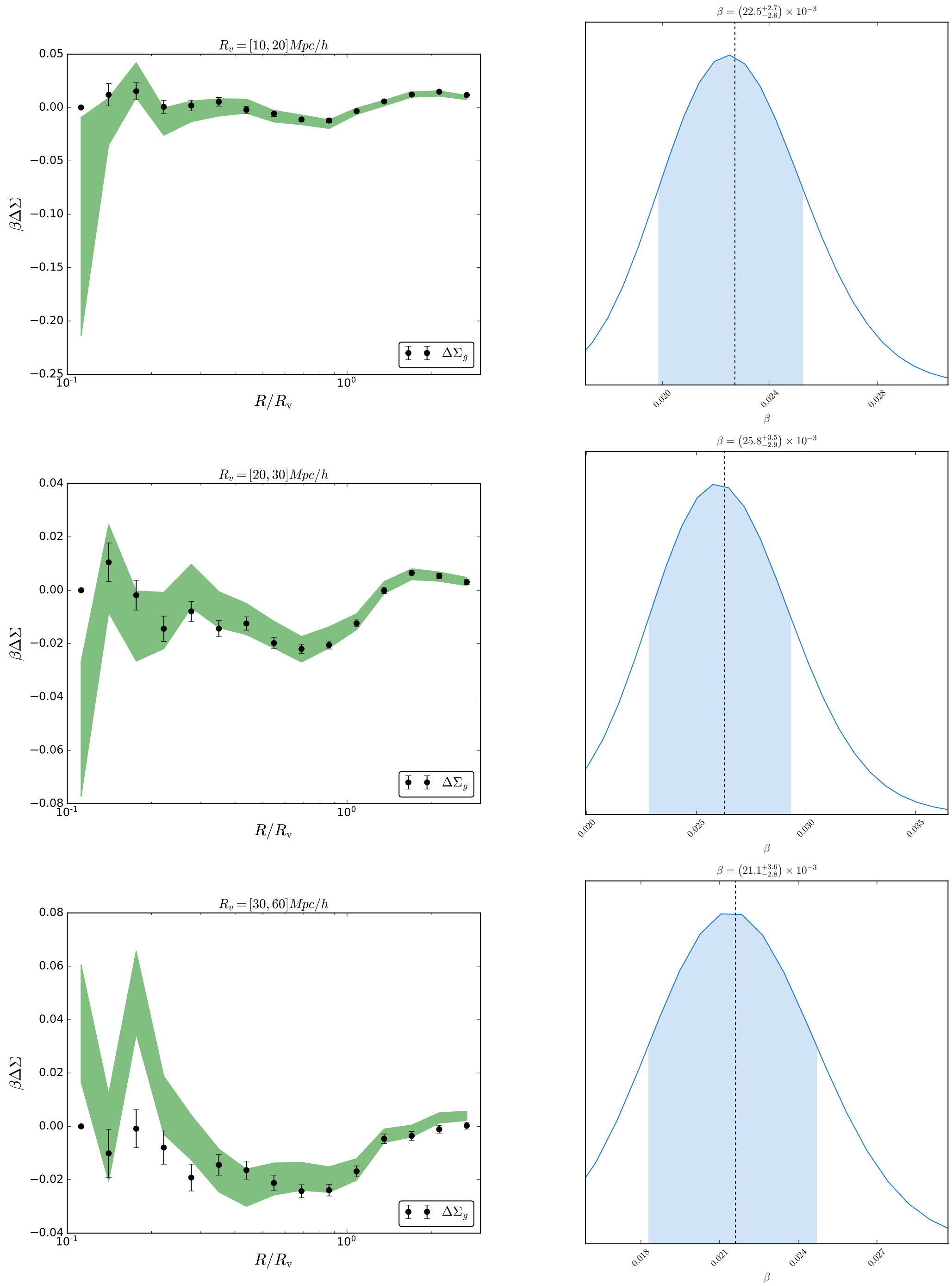

Figure 30: The left panels show the comparison of galaxy and lensing profiles for 3D VIDE voids on DES Y1 data, binning in R_v. The green bands represent the propagated errors. The right panels show the corresponding distribution of fitted β.

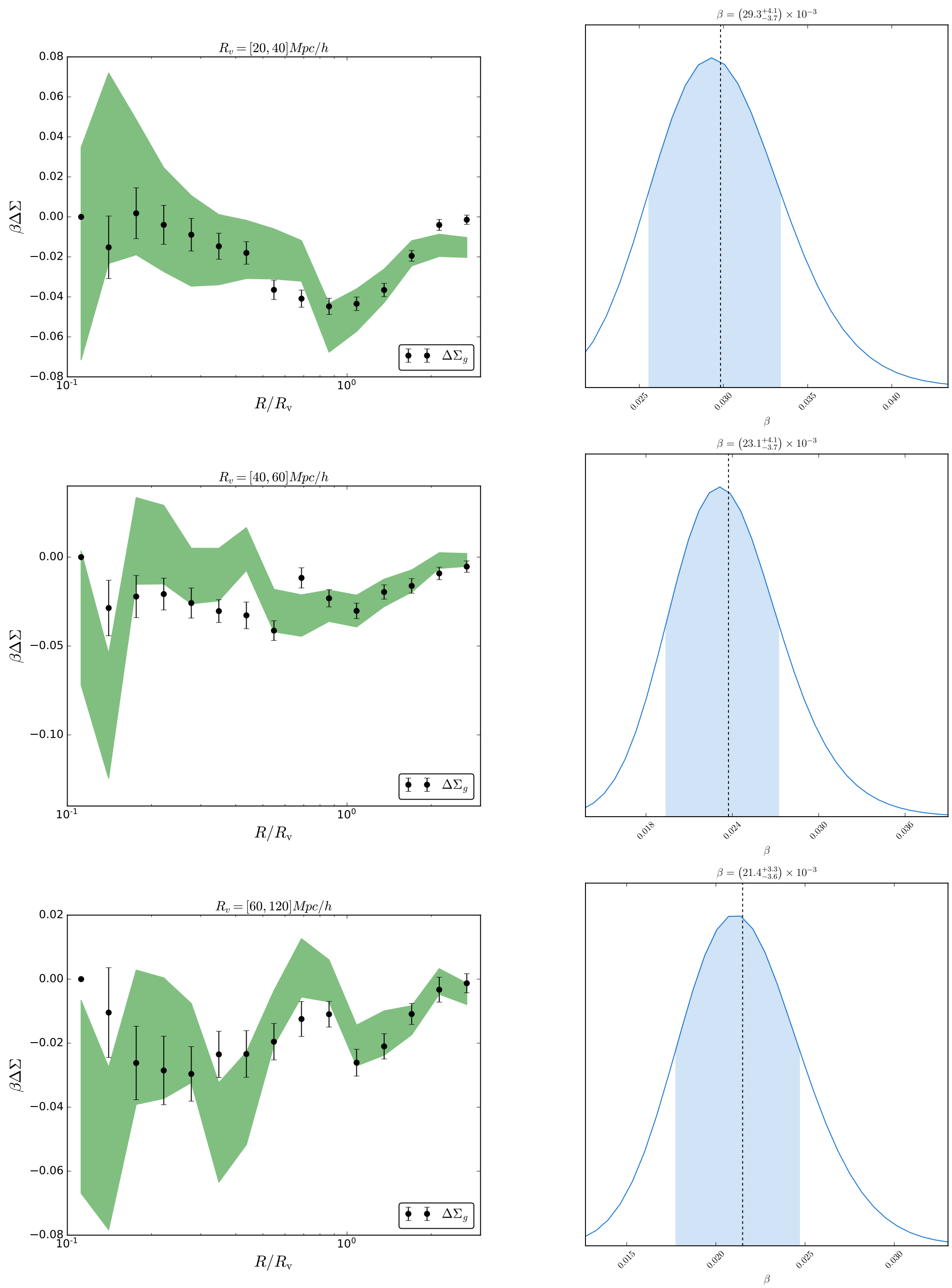

Figure 31: The left panels show the comparison of galaxy and lensing profiles for 2D voids on DES Y1 data, binning in R_v. The green bands represent the propagated errors. The right panels show the corresponding distribution of fitted β.

the 3D VIDE voids. Note that the sparsity of 2D voids leads to much noisier signal for both lensing and clustering measurements. Meanwhile, the theoretical model 4.11 which established in [86] could be void finder dependent. Both of them could potentially bias the linearity analysis.

With the fitted ratio β, we can infer the b_{slope}, which is found to coincide with the tracer bias, using Equation 4.11. We present our estimation of tracer(redMaGiC) bias in Figure 32. In both cases, it is clear that the estimated bias depends on the void radius. For this work, we use the RedMaGiC high density sample as tracers to identify voids. Comparing to the galaxy bias estimated from weak lensing ([87]), which is ≈ 1.6, our results are systematically higher in all R_v bins for both 3D and 2D voids. According to [86], we might need to go to even larger voids for b_{slope} to converge to the linear tracer bias.

4.7. Summary and Discussion

With MICE N-body simulation and DES Year 1 data, we have done comprehensive analysis and measurements of weak lensing and galaxy clustering around voids, identified using two different void finding algorithm. We summarize our work as follows:

1. We have made heretofore the highest signal-to-noise lensing measurements for voids identified using different void finding algorithms. Remarkably, we have got significant lensing signal for 3D VIDE voids on observational data, where there has only been marginal detection in the past. Most importantly, we were able to divide both of our void samples into 3 different void radius bins for each, and still got significant lensing signals from all subsamples.

2. In the lensing results for 2D voids, we can clearly see double dips in the tangential shear profile for the largest R_v bin, and this indicates there could be on-going merging in those large voids. It is also possible that the 2D void finder was mixing up different void types, i.e. the stopping threshold for the circular growth need to be considered with caution for large voids.

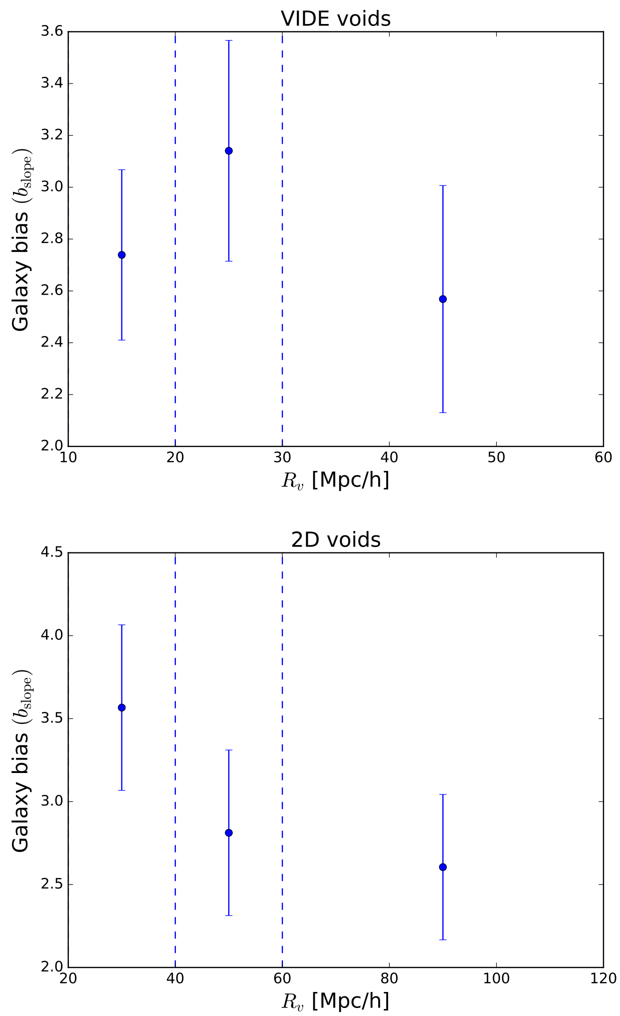

Figure 32: The upper panel shows the galaxy bias($b_{\rm slope}$) inferred from each void radius bin of 3D VIDE voids in DES Y1 data. The lower panel shows the galaxy bias($b_{\rm slope}$) inferred from each void radius bin of 2D voids in DES Y1 data. The vertical dashed lines represent the boundaries of the R_v bins.

3. In the $10 < R_v < 20$ Mpc/h bin of 3D VIDE voids, a positive tangential shear signal is clearly detected beyond the void radius. It suggests that these small 3D voids are likely to be reside in high density environment.

4. With the MICE simulation, we have studied the impact of photo-z scatter on 3D watershed types of void finding algorithms (VIDE). We ran the void finder using the same RedMaGiC sample as tracers, but we were separately using their true and photometric redshifts to identify two different void samples. We did the lensing and void-galaxy correlation measurements on both samples. It turns out the lensing signal for voids identified using photometric redshifts is more significant compared to the voids identified using true redshifts, as well as the galaxy profile for photo-z voids is more negative. It suggests that the photo-z scatter has introduced a selection bias which is helping the 3D void finder to pick out the voids that are emptier and potentially elongated along the line-of-sight direction, which results in a boosting of the negative lensing signal.

5. We have also studied the linear bias relation between mass and galaxy density profiles found in [86], in both simulation and observation. Starting from their Equation.12, we derived the formalism to show that this linear relation should also hold for the 2D differentiate quantities $\Delta\Sigma$ and $\Delta\Sigma_g$. We then performed an MCMC fitting to constrain the ratio β of these two profiles. By comparing $\Delta\Sigma_g$ and $\beta\Delta\Sigma$, we can qualitatively check if this linearity holds. We validated our analysis pipeline with a subsample of 3D VIDE voids on MICE simulation. Then we performed this analysis on both 2D and 3D VIDE voids identified in the DES Year 1 data. We found that for 3D VIDE voids, the two profiles agree with each other quite well, although there are slight deviations in the $30 < R_v < 60$ Mpc/h bin. For the 2D voids, the signals were noisier while the agreements were not as good as for the 3D VIDE voids case. This is the first analysis of voids in data that tests for linear bias of galaxies distributed around voids. We see no evidence of departure from linearity, though our results for

2D voids inside R_v have significant uncertainty.

6. We have further inferred the galaxy-bias using the fitted ratio β. We find evidences for the presence of systematics in the bias estimation: there is a dependence on the void radius, and the values in all of our subsamples are significantly higher than the estimated bias from lensing and clustering measurements ([87]). Thus further studies on the potential systematics is needed for this galaxy-bias inference using voids.

APPENDIX

A.1. Subhalo clustering in N-body simulations

We briefly show results from N-body simulations to demonstrate the effects of tidal stripping exhibited by subhalos that have been in their host for more than a dynamical time. We use the MultiDark Planck 2 simulation [55], available from the CosmoSim database[1]. In Fig. 33 we plot correlations from subhalos within hosts of comparable mass to [10]. The left panel shows subhalos accreted long ago, with accretion redshifts range chosen to be longer than a dynamical time for all the bins. As expected, these subhalos have been in their hosts sufficiently long that long range correlations have completely decayed. The right panel shows subhalos accreted recently: less than a dynamical time ago. These profiles are consistent with no tidal stripping.

[1] `https://www.cosmosim.org`

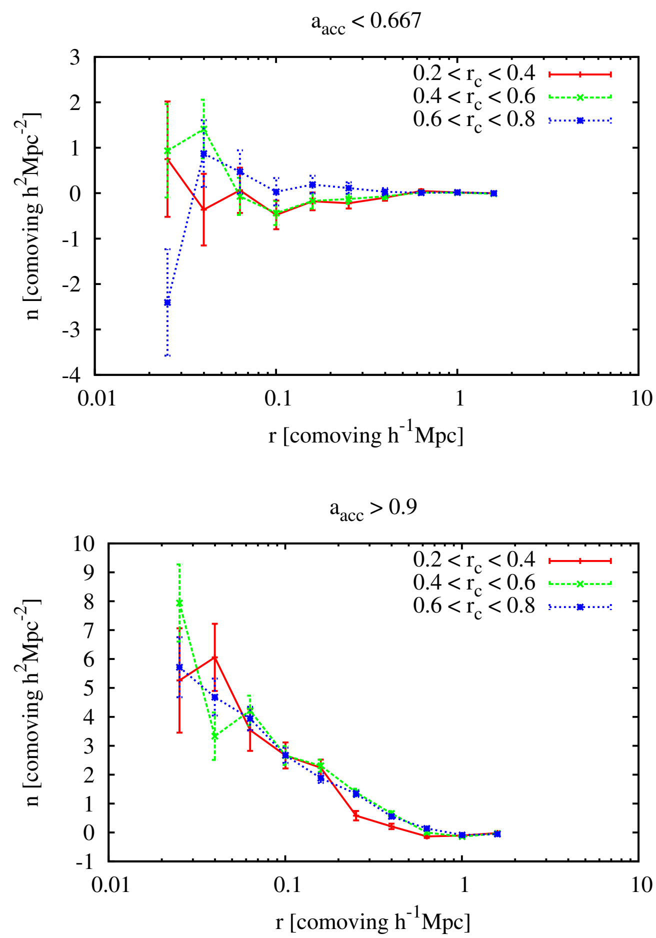

Figure 33: Subhalo correlations in a simulation 64 times bigger than that used in [10]. The left panel shows the measured correlations for subhalos accreted 5 Gyr ago. Thus these subhalos have been in their hosts longer than a dynamical time. From this we conclude that there are no correlations outside r_{tidal} after a dynamical time. The right panel shows the correlations for subhalos accreted more recently, which are consistent with no tidal stripping.

[1] M. G. Abadi, B. Moore, and R. G. Bower. “Ram pressure stripping of spiral galaxies in clusters”. In: *MNRAS* 308 (Oct. 1999), pp. 947–954. DOI: 10.1046/j.1365-8711.1999.02715.x. eprint: astro-ph/9903436.

[2] S. Adhikari, N. Dalal, and R. T. Chamberlain. “Splashback in accreting dark matter halos”. In: *JCAP* 11, 019 (Nov. 2014), p. 019. DOI: 10.1088/1475-7516/2014/11/019. arXiv: 1409.4482.

[3] M. L. Balogh, J. F. Navarro, and S. L. Morris. “The Origin of Star Formation Gradients in Rich Galaxy Clusters”. In: *ApJ* 540 (Sept. 2000), pp. 113–121. DOI: 10.1086/309323. eprint: astro-ph/0004078.

[4] A. Barreira, M. Cautun, B. Li, C. M. Baugh, and S. Pascoli. “Weak lensing by voids in modified lensing potentials”. In: *JCAP* 8, 028 (Aug. 2015), p. 028. DOI: 10.1088/1475-7516/2015/08/028. arXiv: 1505.05809.

[5] M. Bartelmann and P. Schneider. “Weak gravitational lensing”. In: *Phys. Rep.* 340 (Jan. 2001), pp. 291–472. DOI: 10.1016/S0370-1573(00)00082-X. eprint: astro-ph/9912508.

[6] T. G. Brainerd, R. D. Blandford, and I. Smail. “Weak Gravitational Lensing by Galaxies”. In: *ApJ* 466 (Aug. 1996), p. 623. DOI: 10.1086/177537. eprint: astro-ph/9503073.

[7] M. Cacciato et al. “Galaxy clustering and galaxy-galaxy lensing: a promising union to constrain cosmological parameters”. In: *MNRAS* 394 (Apr. 2009), pp. 929–946. DOI: 10.1111/j.1365-2966.2008.14362.x. arXiv: 0807.4932.

[8] Padmanabhan N. & van den Bosch F. C. Campbell D. *in SnowPAC 2016: The Galaxy-Halo Connection.* 2016. URL: http://www.physics.utah.edu/snowpac/talks/campbell.pdf.

[9] M. Cautun et al. “The Santiago-Harvard-Edinburgh-Durham void comparison I: SHEDding light on chameleon gravity tests”. In: *ArXiv e-prints* (Oct. 2017). arXiv: 1710.01730.

[10] R. T. Chamberlain, N. Dalal, A. Hearin, and P. Ricker. “Probing satellite quenching with galaxy clustering”. In: *MNRAS* 451 (Aug. 2015), pp. 1496–1501. DOI: 10.1093/mnras/stv973. arXiv: 1407.2648.

[11] J. Clampitt, Y.-C. Cai, and B. Li. “Voids in modified gravity: excursion set predictions”. In: *MNRAS* 431 (May 2013), pp. 749–766. DOI: 10.1093/mnras/stt219. arXiv: 1212.2216 [astro-ph.CO].

[12] J. Clampitt and B. Jain. “Lensing measurements of the ellipticity of luminous red galaxies dark matter haloes”. In: *MNRAS* 457 (Apr. 2016), pp. 4135–4146. DOI: 10.1093/mnras/stw254. arXiv: 1506.03536.

[13] J. Clampitt and B. Jain. "Lensing measurements of the mass distribution in SDSS voids". In: *MNRAS* 454 (Dec. 2015), pp. 3357–3365. DOI: 10.1093/mnras/stv2215. arXiv: 1404.1834.

[14] J. Clampitt, H. Miyatake, B. Jain, and M. Takada. "Detection of stacked filament lensing between SDSS luminous red galaxies". In: *MNRAS* 457 (Apr. 2016), pp. 2391–2400. DOI: 10.1093/mnras/stw142. arXiv: 1402.3302.

[15] J. Clampitt et al. "Galaxy-galaxy lensing in the Dark Energy Survey Science Verification data". In: *MNRAS* 465 (Mar. 2017), pp. 4204–4218. DOI: 10.1093/mnras/stw2988. arXiv: 1603.05790.

[16] J. D. Cohn. "Galaxy subgroups in galaxy clusters". In: *MNRAS* 419 (Jan. 2012), pp. 1017–1027. DOI: 10.1111/j.1365-2966.2011.19756.x. arXiv: 1105.1397.

[17] J. D. Cohn and M. White. "Using large galaxy surveys to distinguish z $\sim$ 0.5 quiescent galaxy models". In: *MNRAS* 440 (May 2014), pp. 1712–1729. DOI: 10.1093/mnras/stu367. arXiv: 1311.0850.

[18] J. M. Colberg et al. "The Aspen-Amsterdam void finder comparison project". In: *MNRAS* 387 (June 2008), pp. 933–944. DOI: 10.1111/j.1365-2966.2008.13307.x. arXiv: 0803.0918.

[19] P. Coles and B. Jones. "A lognormal model for the cosmological mass distribution". In: *MNRAS* 248 (Jan. 1991), pp. 1–13. DOI: 10.1093/mnras/248.1.1.

[20] M. Colless et al. "The 2dF Galaxy Redshift Survey: spectra and redshifts". In: *MNRAS* 328 (Dec. 2001), pp. 1039–1063. DOI: 10.1046/j.1365-8711.2001.04902.x. eprint: astro-ph/0106498.

[21] M. Crocce, F. J. Castander, E. Gaztañaga, P. Fosalba, and J. Carretero. "The MICE Grand Challenge lightcone simulation - II. Halo and galaxy catalogues". In: *MNRAS* 453 (Oct. 2015), pp. 1513–1530. DOI: 10.1093/mnras/stv1708. arXiv: 1312.2013.

[22] N. Dalal, M. White, J. R. Bond, and A. Shirokov. "Halo Assembly Bias in Hierarchical Structure Formation". In: *ApJ* 687, 12-21 (Nov. 2008), pp. 12–21. DOI: 10.1086/591512. arXiv: 0803.3453.

[23] M. Davis and P. J. E. Peebles. "A survey of galaxy redshifts. V - The two-point position and velocity correlations". In: *ApJ* 267 (Apr. 1983), pp. 465–482. DOI: 10.1086/160884.

[24] K. S. Dawson et al. "The Baryon Oscillation Spectroscopic Survey of SDSS-III". In: *AJ* 145, 10 (Jan. 2013), p. 10. DOI: 10.1088/0004-6256/145/1/10. arXiv: 1208.0022.

[25] J. T. A. de Jong et al. "The Kilo-Degree Survey". In: *The Messenger* 154 (Dec. 2013), pp. 44–46.

[26] A. Dekel and Y. Birnboim. "Galaxy bimodality due to cold flows and shock heating". In: *MNRAS* 368 (May 2006), pp. 2–20. DOI: 10.1111/j.1365-2966.2006.10145.x. eprint: astro-ph/0412300.

[27] I. P. dell'Antonio and J. A. Tyson. "Galaxy Dark Matter: Galaxy-Galaxy Lensing in the Hubble Deep Field". In: *ApJL* 473 (Dec. 1996), p. L17. DOI: 10.1086/310378. eprint: astro-ph/9608043.

[28] B. Diemer and A. V. Kravtsov. "Dependence of the Outer Density Profiles of Halos on Their Mass Accretion Rate". In: *ApJ* 789, 1 (July 2014), p. 1. DOI: 10.1088/0004-637X/789/1/1. arXiv: 1401.1216.

[29] J. P. Dietrich et al. "A filament of dark matter between two clusters of galaxies". In: *Nature (London)* 487 (July 2012), pp. 202–204. DOI: 10.1038/nature11224. arXiv: 1207.0809 [astro-ph.CO].

[30] M. Donahue et al. "The Morphologies and Alignments of Gas, Mass, and the Central Galaxies of CLASH Clusters of Galaxies". In: *ApJ* 819, 36 (Mar. 2016), p. 36. DOI: 10.3847/0004-637X/819/1/36. arXiv: 1601.04947.

[31] T. Erben et al. "CFHTLenS: the Canada-France-Hawaii Telescope Lensing Survey - imaging data and catalogue products". In: *MNRAS* 433 (Aug. 2013), pp. 2545–2563. DOI: 10.1093/mnras/stt928. arXiv: 1210.8156.

[32] A. K. D. Evans and S. Bridle. "A Detection of Dark Matter Halo Ellipticity using Galaxy Cluster Lensing in the SDSS". In: *ApJ* 695 (Apr. 2009), pp. 1446–1456. DOI: 10.1088/0004-637X/695/2/1446. arXiv: 0806.2723.

[33] Y. Fang et al. "Tidal stripping as a test of satellite quenching in redMaPPer clusters". In: *MNRAS* 463 (Dec. 2016), pp. 1907–1915. DOI: 10.1093/mnras/stw2108. arXiv: 1604.08611.

[34] R. Farouki and S. L. Shapiro. "Computer simulations of environmental influences on galaxy evolution in dense clusters. II - Rapid tidal encounters". In: *ApJ* 243 (Jan. 1981), pp. 32–41. DOI: 10.1086/158563.

[35] P. Fosalba, E. Gaztañaga, F. J. Castander, and M. Crocce. "The MICE Grand Challenge light-cone simulation - III. Galaxy lensing mocks from all-sky lensing maps". In: *MNRAS* 447 (Feb. 2015), pp. 1319–1332. DOI: 10.1093/mnras/stu2464. arXiv: 1312.2947.

[36] P. Fosalba, M. Crocce, E. Gaztañaga, and F. J. Castander. "The MICE grand challenge lightcone simulation - I. Dark matter clustering". In: *MNRAS* 448 (Apr. 2015), pp. 2987–3000. DOI: 10.1093/mnras/stv138. arXiv: 1312.1707.

[37] L. Gao, V. Springel, and S. D. M. White. "The age dependence of halo clustering". In: *MNRAS* 363 (Oct. 2005), pp. L66–L70. DOI: 10.1111/j.1745-3933.2005.00084.x. eprint: astro-ph/0506510.

[38] L. Gao, S. D. M. White, A. Jenkins, F. Stoehr, and V. Springel. "The subhalo populations of ΛCDM dark haloes". In: *MNRAS* 355 (Dec. 2004), pp. 819–834. DOI: 10.1111/j.1365-2966.2004.08360.x. eprint: astro-ph/0404589.

[39] B. R. Gillis et al. "CFHTLenS: the environmental dependence of galaxy halo masses from weak lensing". In: *MNRAS* 431 (May 2013), pp. 1439–1452. DOI: 10.1093/mnras/stt274. arXiv: 1301.7421.

[40] K. M. Górski and E. Hivon. *HEALPix: Hierarchical Equal Area isoLatitude Pixelization of a sphere*. Astrophysics Source Code Library. July 2011. ascl: 1107.018.

[41] J. E. Gunn and J. R. Gott III. "On the Infall of Matter Into Clusters of Galaxies and Some Effects on Their Evolution". In: *ApJ* 176 (Aug. 1972), p. 1. DOI: 10.1086/151605.

[42] N. Hamaus et al. "Constraints on Cosmology and Gravity from the Dynamics of Voids". In: *Physical Review Letters* 117.9, 091302 (Aug. 2016), p. 091302. DOI: 10.1103/PhysRevLett.117.091302. arXiv: 1602.01784.

[43] E. Hayashi, J. F. Navarro, J. E. Taylor, J. Stadel, and T. Quinn. "The Structural Evolution of Substructure". In: *ApJ* 584 (Feb. 2003), pp. 541–558. DOI: 10.1086/345788. eprint: astro-ph/0203004.

[44] A. P. Hearin and D. F. Watson. "The dark side of galaxy colour". In: *MNRAS* 435 (Oct. 2013), pp. 1313–1324. DOI: 10.1093/mnras/stt1374. arXiv: 1304.5557.

[45] A. P. Hearin et al. "The dark side of galaxy colour: evidence from new SDSS measurements of galaxy clustering and lensing". In: *MNRAS* 444 (Oct. 2014), pp. 729–743. DOI: 10.1093/mnras/stu1443. arXiv: 1310.6747.

[46] C. Heymans et al. "CFHTLenS: the Canada-France-Hawaii Telescope Lensing Survey". In: *MNRAS* 427 (Nov. 2012), pp. 146–166. DOI: 10.1111/j.1365-2966.2012.21952.x. arXiv: 1210.0032.

[47] S. Hilbert, J. Hartlap, and P. Schneider. "Cosmic shear covariance: the log-normal approximation". In: *A&A* 536, A85 (Dec. 2011), A85. DOI: 10.1051/0004-6361/201117294. arXiv: 1105.3980.

[48] M. J. Hudson et al. "CFHTLenS: co-evolution of galaxies and their dark matter haloes". In: *MNRAS* 447 (Feb. 2015), pp. 298–314. DOI: 10.1093/mnras/stu2367. arXiv: 1310.6784.

[49] E. Huff and R. Mandelbaum. "Metacalibration: Direct Self-Calibration of Biases in Shear Measurement". In: *ArXiv e-prints* (Feb. 2017). arXiv: 1702.02600.

[50] M. Jarvis, G. Bernstein, and B. Jain. "The skewness of the aperture mass statistic". In: *MNRAS* 352 (July 2004), pp. 338–352. DOI: 10.1111/j.1365-2966.2004.07926.x. eprint: astro-ph/0307393.

[51] M. Jarvis et al. "The DES Science Verification weak lensing shear catalogues". In: *MNRAS* 460 (Aug. 2016), pp. 2245–2281. DOI: 10.1093/mnras/stw990. arXiv: 1507.05603 [astro-ph.IM].

[52] M. Jauzac et al. "A weak lensing mass reconstruction of the large-scale filament feeding the massive galaxy cluster MACS J0717.5+3745". In: *MNRAS* 426 (Nov.

2012), pp. 3369–3384. DOI: 10.1111/j.1365-2966.2012.21966.x. arXiv: 1208.4323.

[53] D. E. Johnston et al. “Cross-correlation Weak Lensing of SDSS galaxy Clusters II: Cluster Density Profiles and the Mass–Richness Relation”. In: *ArXiv e-prints* (Sept. 2007). arXiv: 0709.1159.

[54] N. Kaiser. “On the spatial correlations of Abell clusters”. In: *ApJL* 284 (Sept. 1984), pp. L9–L12. DOI: 10.1086/184341.

[55] A. Klypin, G. Yepes, S. Gottlöber, F. Prada, and S. Heß. “MultiDark simulations: the story of dark matter halo concentrations and density profiles”. In: *MNRAS* 457 (Apr. 2016), pp. 4340–4359. DOI: 10.1093/mnras/stw248. arXiv: 1411.4001.

[56] E. Krause et al. “Dark Energy Survey Year 1 Results: Multi-Probe Methodology and Simulated Likelihood Analyses”. In: *ArXiv e-prints* (June 2017). arXiv: 1706.09359.

[57] K. Kuijken et al. “Gravitational lensing analysis of the Kilo-Degree Survey”. In: *MNRAS* 454 (Dec. 2015), pp. 3500–3532. DOI: 10.1093/mnras/stv2140. arXiv: 1507.00738.

[58] J. Kwan et al. “Cosmology from large-scale galaxy clustering and galaxy-galaxy lensing with Dark Energy Survey Science Verification data”. In: *MNRAS* 464 (Feb. 2017), pp. 4045–4062. DOI: 10.1093/mnras/stw2464. arXiv: 1604.07871.

[59] S. D. Landy and A. S. Szalay. “Bias and variance of angular correlation functions”. In: *ApJ* 412 (July 1993), pp. 64–71. DOI: 10.1086/172900.

[60] R. B. Larson, B. M. Tinsley, and C. N. Caldwell. “The evolution of disk galaxies and the origin of S0 galaxies”. In: *ApJ* 237 (May 1980), pp. 692–707. DOI: 10.1086/157917.

[61] G. Lavaux and B. D. Wandelt. “Precision Cosmography with Stacked Voids”. In: *ApJ* 754, 109 (Aug. 2012), p. 109. DOI: 10.1088/0004-637X/754/2/109. arXiv: 1110.0345 [astro-ph.CO].

[62] R. Li et al. “Measuring subhalo mass in redMaPPer clusters with CFHT Stripe 82 Survey”. In: *MNRAS* 458 (May 2016), pp. 2573–2583. DOI: 10.1093/mnras/stw494. arXiv: 1507.01464.

[63] R. Mandelbaum, U. Seljak, and C. M. Hirata. “A halo mass–concentration relation from weak lensing”. In: *JCAP* 8, 006 (Aug. 2008), p. 006. DOI: 10.1088/1475-7516/2008/08/006. arXiv: 0805.2552.

[64] R. Mandelbaum et al. “Cosmological parameter constraints from galaxy-galaxy lensing and galaxy clustering with the SDSS DR7”. In: *MNRAS* 432 (June 2013), pp. 1544–1575. DOI: 10.1093/mnras/stt572. arXiv: 1207.1120.

[65] R. Mandelbaum et al. “Density profiles of galaxy groups and clusters from SDSS galaxy-galaxy weak lensing”. In: *MNRAS* 372 (Oct. 2006), pp. 758–776. DOI: 10.1111/j.1365-2966.2006.10906.x. eprint: astro-ph/0605476.

[66] R. Mandelbaum, U. Seljak, G. Kauffmann, C. M. Hirata, and J. Brinkmann. “Galaxy halo masses and satellite fractions from galaxy-galaxy lensing in the Sloan Digital Sky Survey: stellar mass, luminosity, morphology and environment dependencies”. In: *MNRAS* 368 (May 2006), pp. 715–731. DOI: 10.1111/j.1365-2966.2006.10156.x. eprint: astro-ph/0511164.

[67] R. Mandelbaum, U. Seljak, T. Baldauf, and R. E. Smith. “Precision cluster mass determination from weak lensing”. In: *MNRAS* 405 (July 2010), pp. 2078–2102. DOI: 10.1111/j.1365-2966.2010.16619.x. arXiv: 0911.4972.

[68] R. Mandelbaum et al. “Strong bimodality in the host halo mass of central galaxies from galaxy-galaxy lensing”. In: *MNRAS* 457 (Apr. 2016), pp. 3200–3218. DOI: 10.1093/mnras/stw188. arXiv: 1509.06762.

[69] C. Maraston et al. “Star formation rates and masses of z ˜ 2 galaxies from multicolour photometry”. In: *MNRAS* 407 (Sept. 2010), pp. 830–845. DOI: 10.1111/j.1365-2966.2010.16973.x. arXiv: 1004.4546.

[70] P. Melchior et al. “Mass and galaxy distributions of four massive galaxy clusters from Dark Energy Survey Science Verification data”. In: *MNRAS* 449 (May 2015), pp. 2219–2238. DOI: 10.1093/mnras/stv398. arXiv: 1405.4285.

[71] H. Miyatake et al. “Evidence of Halo Assembly Bias in Massive Clusters”. In: *Physical Review Letters* 116.4, 041301 (Jan. 2016), p. 041301. DOI: 10.1103/PhysRevLett.116.041301. arXiv: 1506.06135.

[72] S. Miyazaki et al. “Properties of Weak Lensing Clusters Detected on Hyper Suprime-Cam 2.3 square deg field”. In: *ApJ* 807, 22 (July 2015), p. 22. DOI: 10.1088/0004-637X/807/1/22. arXiv: 1504.06974.

[73] B. Moore, N. Katz, G. Lake, A. Dressler, and A. Oemler. “Galaxy harassment and the evolution of clusters of galaxies”. In: *Nature (London)* 379 (Feb. 1996), pp. 613–616. DOI: 10.1038/379613a0. eprint: astro-ph/9510034.

[74] S. More et al. “Detection of the Splashback Radius and Halo Assembly Bias of Massive Galaxy Clusters”. In: *ApJ* 825, 39 (July 2016), p. 39. DOI: 10.3847/0004-637X/825/1/39. arXiv: 1601.06063.

[75] J. Moustakas et al. “PRIMUS: Constraints on Star Formation Quenching and Galaxy Merging, and the Evolution of the Stellar Mass Function from z = 0-1”. In: *ApJ* 767, 50 (Apr. 2013), p. 50. DOI: 10.1088/0004-637X/767/1/50. arXiv: 1301.1688 [astro-ph.CO].

[76] J. F. Navarro, C. S. Frenk, and S. D. M. White. “A Universal Density Profile from Hierarchical Clustering”. In: *ApJ* 490 (Dec. 1997), pp. 493–508. DOI: 10.1086/304888. eprint: astro-ph/9611107.

[77] M. C. Neyrinck. “ZOBOV: a parameter-free void-finding algorithm”. In: *MNRAS* 386 (June 2008), pp. 2101–2109. DOI: 10.1111/j.1365-2966.2008.13180.x. arXiv: 0712.3049.

[78] P. Norberg, C. M. Baugh, E. Gaztañaga, and D. J. Croton. "Statistical analysis of galaxy surveys - I. Robust error estimation for two-point clustering statistics". In: *MNRAS* 396 (June 2009), pp. 19–38. DOI: 10.1111/j.1365-2966.2009.14389.x. arXiv: 0810.1885.

[79] B. Nord et al. "Observation and Confirmation of Six Strong-lensing Systems in the Dark Energy Survey Science Verification Data". In: *ApJ* 827, 51 (Aug. 2016), p. 51. DOI: 10.3847/0004-637X/827/1/51. arXiv: 1512.03062.

[80] M. Oguri, M. Takada, N. Okabe, and G. P. Smith. "Direct measurement of dark matter halo ellipticity from two-dimensional lensing shear maps of 25 massive clusters". In: *MNRAS* 405 (July 2010), pp. 2215–2230. DOI: 10.1111/j.1365-2966.2010.16622.x. arXiv: 1004.4214.

[81] N. D. Padilla, L. Ceccarelli, and D. G. Lambas. "Spatial and dynamical properties of voids in a Λ cold dark matter universe". In: *MNRAS* 363 (Nov. 2005), pp. 977–990. DOI: 10.1111/j.1365-2966.2005.09500.x. eprint: astro-ph/0508297.

[82] E. Pastor Mira, S. Hilbert, J. Hartlap, and P. Schneider. "Probing the dark-matter halos of cluster galaxies with weak lensing". In: *A&A* 531, A169 (July 2011), A169. DOI: 10.1051/0004-6361/201116851. arXiv: 1103.1635.

[83] P. J. E. Peebles. "Statistical analysis of catalogs of extragalactic objects. VI - The galaxy distribution in the Jagellonian field". In: *ApJ* 196 (Mar. 1975), pp. 647–651. DOI: 10.1086/153450.

[84] P. J. E. Peebles. *The large-scale structure of the universe*. 1980.

[85] E. Platen, R. van de Weygaert, and B. J. T. Jones. "A cosmic watershed: the WVF void detection technique". In: *MNRAS* 380 (Sept. 2007), pp. 551–570. DOI: 10.1111/j.1365-2966.2007.12125.x. arXiv: 0706.2788.

[86] G. Pollina et al. "On the linearity of tracer bias around voids". In: *MNRAS* 469 (July 2017), pp. 787–799. DOI: 10.1093/mnras/stx785. arXiv: 1610.06176.

[87] J. Prat et al. "Dark Energy Survey Year 1 Results: Galaxy-Galaxy Lensing". In: *ArXiv e-prints* (Aug. 2017). arXiv: 1708.01537.

[88] E. Rozo and E. S. Rykoff. "redMaPPer II: X-Ray and SZ Performance Benchmarks for the SDSS Catalog". In: *ApJ* 783, 80 (Mar. 2014), p. 80. DOI: 10.1088/0004-637X/783/2/80. arXiv: 1303.3373.

[89] E. Rozo et al. "Constraining the Scatter in the Mass-richness Relation of maxBCG Clusters with Weak Lensing and X-ray Data". In: *ApJ* 699 (July 2009), pp. 768–781. DOI: 10.1088/0004-637X/699/1/768. arXiv: 0809.2794.

[90] E. Rozo et al. "redMaGiC: selecting luminous red galaxies from the DES Science Verification data". In: *MNRAS* 461 (Sept. 2016), pp. 1431–1450. DOI: 10.1093/mnras/stw1281. arXiv: 1507.05460 [astro-ph.IM].

[91] E. Rozo, E. S. Rykoff, M. Becker, R. M. Reddick, and R. H. Wechsler. "redMaPPer - IV. Photometric membership identification of red cluster galaxies with 1 per cent

precision”. In: *MNRAS* 453 (Oct. 2015), pp. 38–52. DOI: 10.1093/mnras/stv1560. arXiv: 1410.1193.

[92] E. S. Rykoff et al. “redMaPPer. I. Algorithm and SDSS DR8 Catalog”. In: *ApJ* 785, 104 (Apr. 2014), p. 104. DOI: 10.1088/0004-637X/785/2/104. arXiv: 1303.3562.

[93] E. S. Rykoff et al. “The RedMaPPer Galaxy Cluster Catalog From DES Science Verification Data”. In: *ApJS* 224, 1 (May 2016), p. 1. DOI: 10.3847/0067-0049/224/1/1. arXiv: 1601.00621.

[94] E. E. Salpeter. “The Luminosity Function and Stellar Evolution.” In: *ApJ* 121 (Jan. 1955), p. 161. DOI: 10.1086/145971.

[95] C. Sánchez et al. “Cosmic voids and void lensing in the Dark Energy Survey Science Verification data”. In: *MNRAS* 465 (Feb. 2017), pp. 746–759. DOI: 10.1093/mnras/stw2745. arXiv: 1605.03982.

[96] M. Seldner, B. Siebers, E. J. Groth, and P. J. E. Peebles. “New reduction of the Lick catalog of galaxies”. In: *AJ* 82 (Apr. 1977), pp. 249–256. DOI: 10.1086/112039.

[97] E. S. Sheldon. “An implementation of Bayesian lensing shear measurement”. In: *MNRAS* 444 (Oct. 2014), pp. L25–L29. DOI: 10.1093/mnrasl/slu104. arXiv: 1403.7669.

[98] E. S. Sheldon and E. M. Huff. “Practical Weak-lensing Shear Measurement with Metacalibration”. In: *ApJ* 841, 24 (May 2017), p. 24. DOI: 10.3847/1538-4357/aa704b. arXiv: 1702.02601.

[99] E. S. Sheldon et al. “Cross-correlation Weak Lensing of SDSS Galaxy Clusters. III. Mass-to-Light Ratios”. In: *ApJ* 703 (Oct. 2009), pp. 2232–2248. DOI: 10.1088/0004-637X/703/2/2232. arXiv: 0709.1162.

[100] E. S. Sheldon et al. “The Galaxy-Mass Correlation Function Measured from Weak Lensing in the Sloan Digital Sky Survey”. In: *AJ* 127 (May 2004), pp. 2544–2564. DOI: 10.1086/383293. eprint: astro-ph/0312036.

[101] R. K. Sheth and G. Tormen. “On the environmental dependence of halo formation”. In: *MNRAS* 350 (June 2004), pp. 1385–1390. DOI: 10.1111/j.1365-2966.2004.07733.x. eprint: astro-ph/0402237.

[102] C. Sifón et al. “The masses of satellites in GAMA galaxy groups from 100 square degrees of KiDS weak lensing data”. In: *MNRAS* 454 (Dec. 2015), pp. 3938–3951. DOI: 10.1093/mnras/stv2051. arXiv: 1507.00737.

[103] M. Simet et al. “Weak lensing measurement of the mass-richness relation of SDSS redMaPPer clusters”. In: *MNRAS* 466 (Apr. 2017), pp. 3103–3118. DOI: 10.1093/mnras/stw3250. arXiv: 1603.06953.

[104] S. Singh, R. Mandelbaum, U. Seljak, A. Slosar, and J. Vazquez Gonzalez. “Galaxy-galaxy lensing estimators and their covariance properties”. In: *MNRAS* 471 (Nov. 2017), pp. 3827–3844. DOI: 10.1093/mnras/stx1828. arXiv: 1611.00752.

[105] E. Suchyta et al. “No galaxy left behind: accurate measurements with the faintest objects in the Dark Energy Survey”. In: *MNRAS* 457 (Mar. 2016), pp. 786–808. DOI: 10.1093/mnras/stv2953. arXiv: 1507.08336.

[106] P. M. Sutter, A. Pisani, B. D. Wandelt, and D. H. Weinberg. “A measurement of the Alcock-Paczyński effect using cosmic voids in the SDSS”. In: *MNRAS* 443 (Oct. 2014), pp. 2983–2990. DOI: 10.1093/mnras/stu1392. arXiv: 1404.5618.

[107] P. M. Sutter et al. “VIDE: The Void IDentification and Examination toolkit”. In: *Astronomy and Computing* 9 (Mar. 2015), pp. 1–9. DOI: 10.1016/j.ascom.2014.10.002. arXiv: 1406.1191.

[108] M. A. Troxel and M. Ishak. “The intrinsic alignment of galaxies and its impact on weak gravitational lensing in an era of precision cosmology”. In: *Phys. Rep.* 558 (Feb. 2015), pp. 1–59. DOI: 10.1016/j.physrep.2014.11.001. arXiv: 1407.6990.

[109] J. A. Tyson, F. Valdes, J. F. Jarvis, and A. P. Mills Jr. “Galaxy mass distribution from gravitational light deflection”. In: *ApJL* 281 (June 1984), pp. L59–L62. DOI: 10.1086/184285.

[110] M. Velander et al. “CFHTLenS: the relation between galaxy dark matter haloes and baryons from weak gravitational lensing”. In: *MNRAS* 437 (Jan. 2014), pp. 2111–2136. DOI: 10.1093/mnras/stt2013. arXiv: 1304.4265.

[111] M. Viola et al. “Dark matter halo properties of GAMA galaxy groups from 100 square degrees of KiDS weak lensing data”. In: *MNRAS* 452 (Oct. 2015), pp. 3529–3550. DOI: 10.1093/mnras/stv1447. arXiv: 1507.00735.

[112] D. F. Watson et al. “Predicting galaxy star formation rates via the co-evolution of galaxies and haloes”. In: *MNRAS* 446 (Jan. 2015), pp. 651–662. DOI: 10.1093/mnras/stu2065. arXiv: 1403.1578.

[113] R. H. Wechsler, A. R. Zentner, J. S. Bullock, A. V. Kravtsov, and B. Allgood. “The Dependence of Halo Clustering on Halo Formation History, Concentration, and Occupation”. In: *ApJ* 652 (Nov. 2006), pp. 71–84. DOI: 10.1086/507120. eprint: astro-ph/0512416.

[114] A. R. Wetzel, J. L. Tinker, C. Conroy, and F. C. van den Bosch. “Galaxy evolution in groups and clusters: satellite star formation histories and quenching time-scales in a hierarchical Universe”. In: *MNRAS* 432 (June 2013), pp. 336–358. DOI: 10.1093/mnras/stt469. arXiv: 1206.3571.

[115] H. S. Xavier, F. B. Abdalla, and B. Joachimi. “Improving lognormal models for cosmological fields”. In: *MNRAS* 459 (July 2016), pp. 3693–3710. DOI: 10.1093/mnras/stw874. arXiv: 1602.08503.

[116] Y. Zhang, J. P. Dietrich, T. A. McKay, E. S. Sheldon, and A. T. Q. Nguyen. “Studying Intercluster Galaxy Filaments through Stacking gmBCG Galaxy Cluster Pairs”. In: *ApJ* 773, 115 (Aug. 2013), p. 115. DOI: 10.1088/0004-637X/773/2/115. arXiv: 1304.6696.

[117] Y. Zu and R. Mandelbaum. "Mapping stellar content to dark matter haloes - II. Halo mass is the main driver of galaxy quenching". In: *MNRAS* 457 (Apr. 2016), pp. 4360–4383. DOI: 10.1093/mnras/stw221. arXiv: 1509.06758.

[118] Y. Zu and R. Mandelbaum. "Mapping stellar content to dark matter haloes using galaxy clustering and galaxy-galaxy lensing in the SDSS DR7". In: *MNRAS* 454 (Dec. 2015), pp. 1161–1191. DOI: 10.1093/mnras/stv2062. arXiv: 1505.02781.